

UNIVERSITY OF THE WITWATERSRAND

**Characterization of graphene epoxy  
nanocomposite interface region by  
multiscale modelling**

by

Relebohile George Qhobosheane

A dissertation submitted to the Faculty of Engineering and the Built Environment, University of the Witwatersrand, Johannesburg, in fulfilment of the requirements for the degree of Master of Science in Engineering.

July 2018

# Declaration of Authorship

I, Relebohile George Qhobosheane, declare that this thesis titled, ‘Characterization of graphene epoxy nanocomposite interface region by multiscale modeling’ and the work presented in it are my own. I confirm that:

- This work was done wholly or mainly while in candidature for a research degree at the University of Witwatersrand.
- Where any part of this thesis has previously been submitted for a degree or any other qualification at this University or any other institution, this has been clearly stated.
- Where I have consulted the published work of others, this is always clearly attributed.
- Where I have quoted from the work of others, the source is always given. With the exception of such quotations, this thesis is entirely my own work.
- I have acknowledged all main sources of help.
- Where the thesis is based on work done by myself jointly with others, I have made clear exactly what was done by others and what I have contributed myself.

Signed:

---

Date: 16<sup>th</sup> May 2018

*“Without hard work, do not expect any satisfactory payoff”*

Paul Qhobosheane and Mats’epang Qhobosheane

## *Acknowledgements*

- I would first like to thank my thesis advisor Prof Jacob Muthu of the School of Mechanical, Industrial and Aeronautical Engineering at the University of the Witwatersrand. The door to Prof. Muthu's office was always open whenever I ran into a trouble spot or had a question about my research or writing. He consistently pushed me and steered me in the right direction whenever he thought I needed it.
- I would like to thank Department of Science and Technology (DST), Council for Scientific and Industrial Research (CSIR) and SITA for sponsoring my research program and made it possible for the completion of this dissertation.
- I must express my very profound gratitude to my parents Mr Paul and Mrs Mats'epang Qhobosheane for providing me with unfailing support and continuous encouragement throughout my years of study and through the process of researching and writing this thesis. This accomplishment would not have been possible without them.
- Finally, I would like to thank my colleagues, friends and everyone who contributed to my work in anyway throughout.

...

UNIVERSITY OF THE WITWATERSRAND

## *Abstract*

Engineering  
Mechanical, Industrial and Aeronautical

Master of Science

by Relebohile George Qhobosheane

The aim of this study was to characterize graphene epoxy nanocomposite interfacial region using multiscale modelling. Molecular dynamics was used to study the nanocomposite at nano scale and finite element analysis at macroscale to complete the multiscale modeling. Coupling of these two scales was done by the use of a property averaging method known as Irving Kirkwood method. One to three sheets (1.8 %, 3.7 % and 5.4 % graphene weight fraction) of graphene were respectively reinforced with epoxy polymer to form a graphene epoxy nanocomposite. The normal and shear forces at the interfacial region of graphene epoxy nanocomposite were investigated by displacing graphene from epoxy to analyze the mechanical properties including the Youngs Modulus, shear modulus and traction forces. Molecular dynamics simulations were further studied through radial distribution function and molecular energy. The effects of graphene on the density distribution of epoxy in the nanocomposites were also analyzed. The results showed that the density when graphene is added sheet by sheet relatively increases until saturation, and then progressively decreases to a bulk value in regions further away from the interface. Improvements in Youngs Modulus and shear modulus of graphene epoxy model compared to normal epoxy resin were noticed. The dispersed graphene sheet improved the Elastic Modulus more than the agglomerated graphene sheets. The normal and shear forces versus displacement were plotted in order to characterize the interfacial region properties. The elastic constants determined by molecular dynamics were higher than those predicted at macroscale analysis due to the difference in scales. The nanocomposite with 3.7 % weight fraction of graphene gave the best properties of the interfacial region. The results from this model also showed close agreement with the available numerical experiments results from the literature data.

...

# Contents

<b>Declaration of Authorship</b>	<b>i</b>
<b>Acknowledgements</b>	<b>iii</b>
<b>Abstract</b>	<b>iv</b>
<b>List of Figures</b>	<b>viii</b>
<b>List of Tables</b>	<b>xi</b>
<b>1 Introduction</b>	<b>1</b>
1.1 Background . . . . .	1
1.2 Interfacial Region and Properties . . . . .	2
1.3 Multiscale Modelling . . . . .	3
1.4 Research Problem (Research Questions) . . . . .	4
1.5 Research Objective . . . . .	5
1.6 Study Layout . . . . .	5
<b>2 Literature Review</b>	<b>7</b>
2.1 Composites . . . . .	7
2.2 Nanocomposites . . . . .	8
2.2.1 Nanocomposites applications . . . . .	9
2.2.2 Nanocomposites Properties . . . . .	10
2.2.3 Preparation of Nanocomposites . . . . .	12
2.3 Nanocomposites interfacial region . . . . .	16
2.3.1 Matrix and Nanoreinforcement Interaction within the Interfacial region . . . . .	17
2.3.2 Enhancement of Polymer Properties due to Nano-filler . . . . .	17
2.4 Materials . . . . .	20
2.5 Graphene . . . . .	20
2.5.0.1 Graphene Fabrication . . . . .	21
2.5.1 Graphene Properties . . . . .	23
2.5.2 Epoxy . . . . .	28
2.6 Numerical Modelling . . . . .	34

2.6.1	Numerical modeling steps . . . . .	34
2.7	Molecular dynamics . . . . .	35
2.7.1	MD Simulation Methods . . . . .	35
2.7.2	MD Forces . . . . .	36
2.7.3	MD Potentials/Energies . . . . .	37
2.7.4	MD Atomic Interactions . . . . .	39
2.8	Finite Element Analysis . . . . .	41
2.8.1	Multiscale Modelling . . . . .	42
<b>3</b>	<b>Methodology</b>	<b>45</b>
3.1	General Methodology layout . . . . .	45
3.2	Molecular Dynamics Modeling and Finite Element Analysis Procedure . .	46
3.2.1	MD Interaction Forces and Potentials . . . . .	46
3.2.2	MD Boundary Conditions and Force Calculations . . . . .	49
3.2.3	FEA Displacement properties . . . . .	51
3.2.4	Coupling MD with FEA . . . . .	52
3.3	Molecular Dynamics modeling of Graphene-Epoxy Nanocomposite . . . . .	54
3.3.1	Matrix modeling . . . . .	54
3.3.2	Nanoreinforcement modeling . . . . .	56
3.3.3	Interfacial Region Modeling . . . . .	58
3.3.4	MD Interfacial region properties . . . . .	62
3.4	Finite Element Analysis Procedure . . . . .	64
3.4.1	Macroscale Model . . . . .	64
3.4.2	Analysis Procedure . . . . .	65
<b>4</b>	<b>Results and Discussion</b>	<b>67</b>
4.1	MD modelling of graphene functionalization . . . . .	67
4.2	Graphene and Epoxy cross-linking . . . . .	69
4.3	Interfacial region properties . . . . .	70
4.3.1	Traction separation of Graphene (normal displacement) . . . . .	72
4.3.2	Traction separation of graphene (shear displacement) . . . . .	72
4.3.3	Radial distribution function . . . . .	73
4.3.4	Graphene Epoxy Nanocomposite RDF . . . . .	74
4.4	Atom density . . . . .	75
4.5	Bond Stretching During Deformation . . . . .	76
4.6	Angle Bending for Epoxy Nanocomposite . . . . .	77
4.7	Molecular Energy . . . . .	78
4.8	Stress/strain for graphene epoxy nanocomposite . . . . .	79
4.8.1	Dispersion and agglomeration effects . . . . .	80
4.9	Effects of number of graphene sheets . . . . .	81
4.10	Validation of numerical results with available literature data . . . . .	83
4.10.1	Mechanical properties . . . . .	83
4.10.2	Radial Distribution Function Validation . . . . .	84
4.10.3	Thermal Properties . . . . .	85
<b>5</b>	<b>Conclusion</b>	<b>87</b>

<b>A</b>	<b>An Appendix</b>	<b>89</b>
A.1	Appendix A . . . . .	89
	A.1.1 Epoxy LAMMPS input file . . . . .	89
	A.1.2 Epoxy Coordinate Datafile . . . . .	90
A.2	Appendix B . . . . .	94
	A.2.1 Graphene sheet LAMMPS input file . . . . .	94
	A.2.2 Functionalized graphene sheet LAMMPS input file . . . . .	95
	A.2.3 Functionalized graphene sheet coordinate LAMMPS file . . . . .	98
A.3	Appendix C . . . . .	100
	A.3.1 Graphene epoxy nanocomposite system LAMMPS input file . . . . .	100
	A.3.2 Graphene epoxy nanocomposite interfacial region LAMMPS input file . . . . .	102
A.4	Appendix D . . . . .	104
A.5	Appendix E . . . . .	105
	 <b>Bibliography</b>	 <b>106</b>

# List of Figures

1.1	An overview of multiscale modelling, showing the increase in scale (length nm-m) with time (sec)[1] . . . . .	4
2.1	Introduction to composites schematic (G. Hu and Sridhae Komarneni 2017)	7
2.2	Structure of a nanoreinforcement with a matrix to create a nanocomposites (L.S. Brinson and W.G Sawyer 2015) . . . . .	8
2.3	Different types of dispersion of clay layers in polymer matrix[2]. . . . .	13
2.4	Effect of nano OPEFB filler loading on tensile strength of epoxy composites[3].	14
2.5	The dielectric permittivity and nominal breakdown strength of all these four types nanocomposites as a function of filler volume fraction[4]. . . . .	16
2.6	Silicate nanoreinforcement polymer nanocomposite interfacial region . . .	17
2.7	Particle size distribution size within a nanocomposite [2]. . . . .	18
2.8	Thermal properties of graphene/metal composites with aligned graphene[5].	20
2.9	Graphene sheet [6] . . . . .	21
2.10	An AFM (Atomic Force Microscopy) is used to locate individual sheets[7]	22
2.11	Investigation of the size, shape, and number density of deposits in the deposition of graphene on highly oriented pyrolytic graphite substrates[8]	24
2.12	Structural models of surfaces and layers built to explore electronic and optical properties of generated TiO <sub>2</sub> composites[9] . . . . .	27
2.13	Diglycidyl ether of bisphenol A, DGEBA[10] . . . . .	29
2.14	EPN, R = H, ECN, R = CH <sub>3</sub> (Y. Takagi and H. Hirayama 2017) . . . . .	29
2.15	(triglycidyl-p-aminophenol) 8.3 (triglycidyl-p-aminophenol) and (tetraglycidyl-4,4'-diaminodiphenylmethane) TGDDM, Araldite MY 720 (CIBA-GEIGY) ERL 0510 (CIBA-GEIGY) (Y. Takagi and H. Hirayama 2017) . . . . .	30
2.16	Diglycidyl ester of hexahydrophthalic acid (Y. Takagi and H. Hirayama 2017) . . . . .	30
2.17	Dielectric constants (a) and dielectric losses (b and c) of MWCNTs/epoxy resin composites[11]. . . . .	33
2.18	Flow-chart depicting the general steps of a typical MD simulation[12] . . .	36
2.19	Atom positons and velocities in a system to calculate forces (M. Parrinello and A. Rahman 2014). . . . .	38
2.20	Atom positons and velocities in a system to calculate forces (M. Parrinello and A. Rahman 2014). . . . .	38
2.21	Atomic interactions due to van der waal attractions (Matthew Dedmom and C. Dobson 2015). . . . .	39
3.1	General steps of the computational details . . . . .	45
3.2	(a) Bond stretching, (b) Bond rotating (c) Bond bending (d) Mixed (improper)[13] . . . . .	47

3.3	Lennard Jones potentials for MD simulations[14]	48
3.4	Two-dimensional schematic of periodic boundary conditions. The particle trajectories in the central simulation box are copied in every direction	49
3.5	Coupling of molecular dynamics with finite element analysis	52
3.6	a) DGEBA resin molecular structure and b) Molecular structure of DETA hardener.	55
3.7	Change in cross-linking density with time.	56
3.8	Molecular structures of epoxy from LAMMPS simulation post processing software (VMD).	57
3.9	Schematic diagram of a hexagonal graphene sheet, zigzag, and armchair graphene sheet[15].	58
3.10	Lammps model for the graphene sheet	58
3.11	Functionalized graphene sheet	60
3.12	a) 3D model for the graphene epoxy nanocomposite 1 structure and b) 2D 1, 2 and 3 graphene sheets configurations within the graphene epoxy nanocomposite.	61
3.13	Normal and shear displacement of graphene sheet in graphene epoxy nanocomposite	63
3.14	Extraction of initial conditions and boundary conditions from MD scale to macro scale (FEA)	65
3.15	a) 3D cubic RVE filled with grapheme nanoreinforcement with aspect ratio of 100. b) Flexible meshing of RVEs, each disc was partitioned into four symmetric parts	66
4.1	Graphene functionalization grafting percentage with time	68
4.2	Specific volume vs temperature for epoxy nanocomposite	69
4.3	Mechanical properties change with addition of graphene sheets	70
4.4	Normal force verses displacement plots at the interfacial region.	71
4.5	Shear force verses displacement plots at the interfacial region.	72
4.6	Traction separation of graphene under NVT ensemble (Normal)	73
4.7	Traction on graphene under NVT ensemble (shear)	73
4.8	RDF pattern for graphene and epoxy particles in a epoxy nanocomposite.	74
4.9	Atom densities as a function of graphene concentrations	75
4.10	Bond stretch under applied strain for graphene epoxy nanocomposite.	76
4.11	Angle bending under applied strain for epoxy nanocomposite	77
4.12	Molecular energy variation with strain for graphene epoxy nanocomposite.	78
4.13	Stress-strain responses of graphene sheets nanocomposite	79
4.14	Longitudinal modulus of the RVEs versus number of graphene sheets.	81
4.15	Transverse modulus of the RVEs versus number of graphene sheets.	82
4.16	Normal modulus of the RVEs versus number of graphene sheets.	82
4.17	Comparing numerical results with experimental results of graphene epoxy nanocomposite.[8]	84
4.18	Molecular dynamics results validation with literature data for RDF of graphene epoxy nanocomposite.	84
4.19	MD calculation of thermal expansion compared with an experimental data.	85
4.20	Comparing the multiscale modeling results with experimental results of graphene epoxy nanocomposite.	86

A.1	Matlab script for the Macroscale RVE of the nanocomposite system . . .	104
A.2	Matlab script for the Macroscale RVE of the nanocomposite system . . .	105

# List of Tables

3.1	MD initial setup for epoxy matrix modeling. . . . .	55
3.2	MD initial setup for graphene nanoreinforcement modeling . . . . .	57
3.3	Change in number of atoms during functionalization . . . . .	59
3.4	Graphene weight fraction calculation . . . . .	60
3.5	Material configurations of graphene epoxy nanocomposite system . . . . .	61
3.6	The nanocomposite properties extracted from the nanoscale transferred to the macroscale. . . . .	66
3.7	Averaged properties for FEA modelling . . . . .	66
4.1	Validation of MD results with experimental data. . . . .	68
4.2	Youngs modulus E and shear modulus G of graphene epoxy nanocomposites	79
4.3	Dispersion and agglomeration effects . . . . .	81
4.4	Experimental results for epoxy composites with varying GNP volume frac- tions. . . . .	83

# Chapter 1

## Introduction

### 1.1 Background

Nanocomposite materials are extending the horizons of designers in all branches of engineering. They are a combination of matrix and nano-scale reinforcement with the size of less than 100 nano-meters [16]. Nanocomposites have numerous advantages such as improved structural properties, high scratching resistance and the fibres have high surface to volume ratio due to the small size of nano-reinforcements. This has led to their use in a number of applications i.e. automobile and aircraft components, high speed transistors and solar cells.

There are different combinations of nano-fillers (graphene, carbon nanotubes, cellulose, silica, etc.) and polymers to produce various nanocomposites. Graphene-epoxy nanocomposites are one of the few materials that has ignited interest in researchers due to graphenes remarkable properties [17]. Graphene is a monolayered structure in which the carbon atoms are arranged in a hexagonal pattern [18]. The carbon atoms in graphene are in-plane (two-dimensional) carbon-carbon bonded which are known to be the strongest bonds [18] and hence give graphene its excellent mechanical and physical properties. Graphene is therefore 100 times stronger than steel with tensile strength of 130 GPa, a Young's modulus (stiffness) of 1 TPa and stretchable up to 20% of its initial length [19].

The above mentioned properties have made graphene a favourable reinforcement for improving the structural properties of nanocomposites. For instance, epoxy has been utilized in numerous applications, but as a structural material it has a few distinctive drawbacks such as poor mechanical properties like a low tensile strength of 85 MPa and an elongation of 0.8% [19]. However, reinforcing it with a nano-reinforcements with stronger mechanical properties such as graphene is expected to enhance its properties.

## 1.2 Interfacial Region and Properties

Researches [20, 21] have shown that properties of nanocomposite are influenced by a number of factors such as dispersion, weight fraction of nano-reinforcements and the interfacial adhesion between the nano-reinforcement and matrix. Previous works [18, 22] on the characterisation of graphene-epoxy nanocomposites have shown that the strength of the interfacial region between a single graphene sheet and the epoxy matrix define the macro properties of nanocomposite material. This is because the interfacial region properties embody a combination of both graphene reinforcement and epoxy matrix properties and thus defines the overall properties of the nanocomposite material[22]. Since the interfacial region properties differ from the matrix and reinforcement properties, understanding and characterization of the interfacial region would help in improving and tailoring the nanocomposite properties for the required engineering applications[22].

In addition, within the interfacial regions the chemical bond between the nanoreinforcement and the matrix plays a crucial role in improving the overall composite properties. Research [23] showed that the surface treatment (functionalization) of the nano reinforcement could improve the chemical bond between graphene and epoxy matrix. Functionalization is the process, in which the new functionality such as OH, COOH, HNO<sub>3</sub> functional groups, are added. This creates covalent bonds at the edges of graphene nonreinforcement leading to an optimized interaction of the graphene sheet with the polymer matrix improving the interfacial adhesion.

Furthermore, the interfacial region strength is also highly dependent on the alignment of graphene within the polymer matrix. The reactivity of graphene varies at the edges[24]. This alignment of graphene is therefore an important factor as the change in position will affect the reactivity of the graphene nano-reinforcement. The carbon-carbon bonds in graphene are formed by mixing different orbitals (describes the wave-like behaviour of either one electron or a pair of electrons in an atom), namely s- and p-orbital also known as  $sp^2$  hybridized structure [24]. These have saturations of hydrogen and oxygen functionalities at the edges after functionalization[24]. Hence the graphene sheet should be aligned with that edges with high reactivity positioned closer to the polymer chain.

Lastly, weight fraction is one of the important factors affecting the interfacial region of a nanocomposite[21]. A single layer of graphene is almost 10 times more reactive than bi or multi-layered graphene sheets. Hence, aligned and functionalized graphene with high weight fraction results in better interfacial region properties with improved nanocomposite properties[24].

A detailed study of these interfacial region properties not only requires a macro-scale analysis, but also an atomic study should be included for better characterization of

the interfacial region[24]. Research has shown that it is challenging to experimentally characterize the interfacial region of nanocomposites. Most experimental methods generally focus on macro-scale properties and cannot give details at nanoscale[25]. Hence an attempt to improve and further understand the nanocomposite properties can be done by characterizing the interfacial region using numerical methods such as multiscale modelling (MSM)[25].

### 1.3 Multiscale Modelling

The method of coupling models at different time and length scales is known as multiscale modelling (MSM). There are several reasons why this method is necessary. Macro-scale models are not accurate enough even though they have an advantage of covering a larger unit cell of a material for analysis. This is because taking a larger unit cell for analysis eventually misses the nano scale details of the interfacial properties[20]. Therefore multiscale modelling is an alternative numerical tool which can bridge the wide range of time and length scales that are inherent in a number of phenomena and processes in materials science and engineering[25].

The advantage of this hybrid approach is that it incorporates both macro-scale and nano scale analysis into a single simulation. Figure 1.1 illustrates an overview of multiscale modelling with different time and length scales. A combination of quantum, molecular and continuum level computational tools within the various length and time scales can provide different characterization of the nanocomposite interfacial region properties.

Over the past decade, various multiscale modelling methods (adaptive, heterogeneous, quantum coupled with molecular mechanics (QM-MM)) [13] have been developed to address the problems involving different length and time scales[13]. Adaptive mesh refinement method is a multiscale method that analyses crack propagation at different scales of length and time[26]. It is used to model dynamic and turbulent regions without affecting the precision of the solution but limited to pre-determined measured computational grids[26]. QM-MM combines the strengths of the QM (accuracy) and MM (speed) approaches[27]. In this method, simulation regions are also limited[27]. MM simulations (nano-scale) in QM-MM multiscale method may be accurate, but passing the MM boundary conditions to macroscale analysis (coupling) results in inaccuracies due to the change in computational domain size[13].

The most challenging part is the coupling of molecular with continuum scales where the formulation of a seamless connection between material representations at different scales is required to relate the actual material behaviour within the multiscale domain.

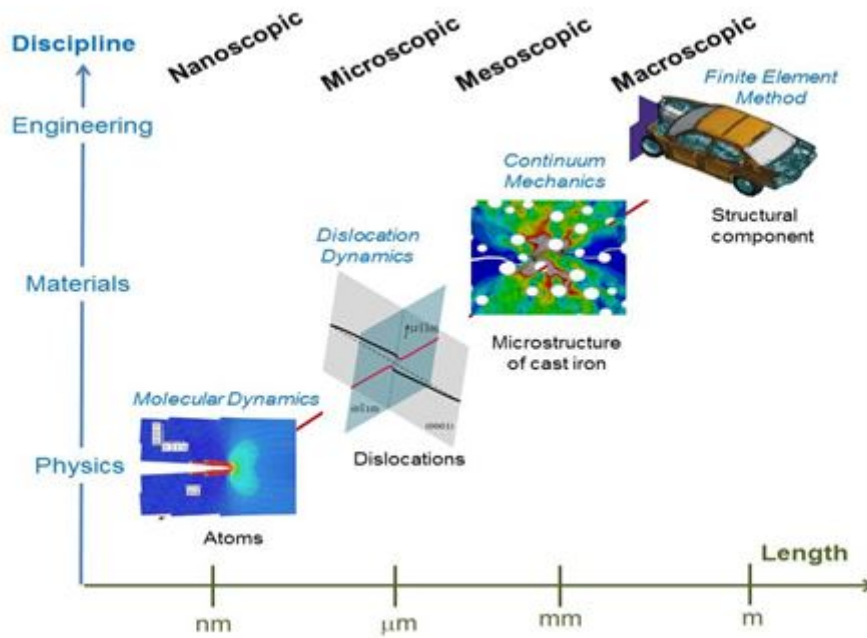


FIGURE 1.1: An overview of multiscale modelling, showing the increase in scale (length nm-m) with time (sec)[1]

In coupling atomistic and continuum material representations, the continuity of material properties must be maintained while the transition is made from individual atoms interaction to the stress/strain field of continuum mechanics[1].

These limitations in computational domain size and proper boundary conditions transfer from macro to nanoscale models have shown not to be an issue in heterogeneous multiscale method. Heterogeneous multiscale modelling follows a top down strategy[28]. The basic starting point is an incomplete macroscale model with the micro or nano scale used as a supplement to supply the missing data including boundary conditions from the nanoscale analysis[28]. This was therefore the reason why multiscale method was chosen to characterize the interfacial region properties of the graphene epoxy nanocomposite in this research.

## 1.4 Research Problem (Research Questions)

Although graphene-epoxy nanocomposites have sparked a lot of interest in the manufacturing and other engineering fields, improving and further understanding its mechanical properties is still an issue. This is because the nanocomposite properties depend on the interfacial region properties which is characterized by different factors such as dispersion, alignment, weight fraction and adhesion of the nano-reinforcement to the polymer

matrix. To improve the interfacial region properties, graphene should be functionalized for improving the bond strength between the graphene and the polymer molecules. Therefore to further understand these issues, the interfacial region must be characterized. Experimental methods have proven ineffective in characterising the nanocomposite interfacial region as they are limited to the macro-scale and cannot analyze properties at nano-scale. This limitation in experimental methods brings forth the need for multiscale modelling that can study the nanocomposite interfacial properties at different scales of length and time and also the properties of the nanocomposite at macro scale.

## 1.5 Research Objective

The objectives of this research are:

- To characterize the interfacial region properties of graphene epoxy nanocomposite using molecular dynamics coupled with finite element analysis based on alignment and dispersion of graphene and the interfacial adhesion between epoxy and graphene reinforcement.
- To optimise the various functionalized groups and their effect on improving the interfacial strength of nanocomposites using molecular dynamics coupled with finite element analysis.
- Experimentally validate the MSM results of the nanocomposite.

## 1.6 Study Layout

Chapter one entails an introductory section for graphene epoxy nanocomposite and the interfacial region coupled with multiscale modelling of this interfacial region.

Chapter two will consist of the literature study and historical review for the project. This will entail looking at the current and proposed methods for characterizing the interfacial region of graphene epoxy nanocomposite.

Chapter three discusses the methodology of the interfacial analysis, preliminary simulation procedure and final post processing specifications which will be used throughout the study. The multiscale modelling technique will also be elaborated on.

In Chapter four, the results from the interfacial region multiscale modelling will be analyzed and discussed with reference to existing data compilation to determine the adequacy for the procedure.

In Chapter five concluding remarks concerning the post processing phase and results will be declared. Recommendations will be stipulated for further reference work.

## Chapter 2

# Literature Review

### 2.1 Composites

Composite materials are one of the most used materials in the engineering industry. They exist in a number of natural forms e.g. bone, wood etc.[29]. Man made composites were the first composite material made out of mud and grass straws to build bricks for construction [29]. Gluing of wood parts into different shapes has also been used by early Egyptians [29]. Concrete is another ancient composite made of stones, sand and cement (binder) and is still in use to construct buildings, roads, etc.

Composite materials consist of matrix and reinforcement. Examples of matrix includes metal, ceramic, and polymer while the reinforcement is particulate and fibres etc [30]. Usually this combination produces a light weight composite material with high specific strength (strength-to-density), high specific modulus (stiffness-to-density), better corrosion, thermal and impact resistance [30]. Composites can be classified in terms of reinforcement as shown in the schematic below.

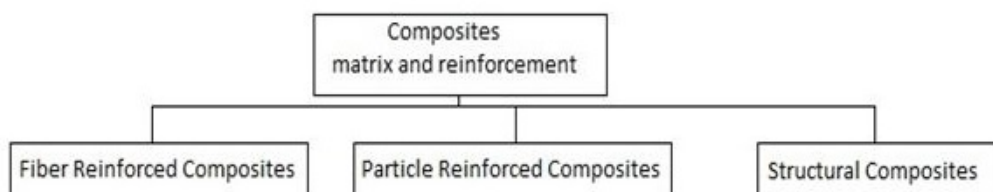


FIGURE 2.1: Introduction to composites schematic (G. Hu and Sridhae Komarneni 2017)

Components made of composite materials can replace an assembly of metal parts for the same purpose and have a more aesthetic appeal than conventional materials. Unlike conventional materials, composites structural properties can be designed as per requirements [29] e.g. laminate pattern can be manufactured from multiple lamina with desirable mechanical properties in different directions[30]. These properties have increased the use and demand of better composites, which has attracted researchers. Main focus for most researchers is the nanocomposites as they display better properties compared to other types of composites[30].

## 2.2 Nanocomposites

Nanocomposites have sparked interest to most researchers in recent years. They have become an alternative to conventional composites due to the improvement in properties. These are composites in which the fillers are less than 100 nm in at least one dimension [31]. This morphology of nanoscale dispersion of the filler phase in the polymer matrix leads to tremendous interfacial contact of the nanoparticles with the polymer matrix, and subsequently to confined polymer chains in between the nanometer thick delaminated elementary layers [32].

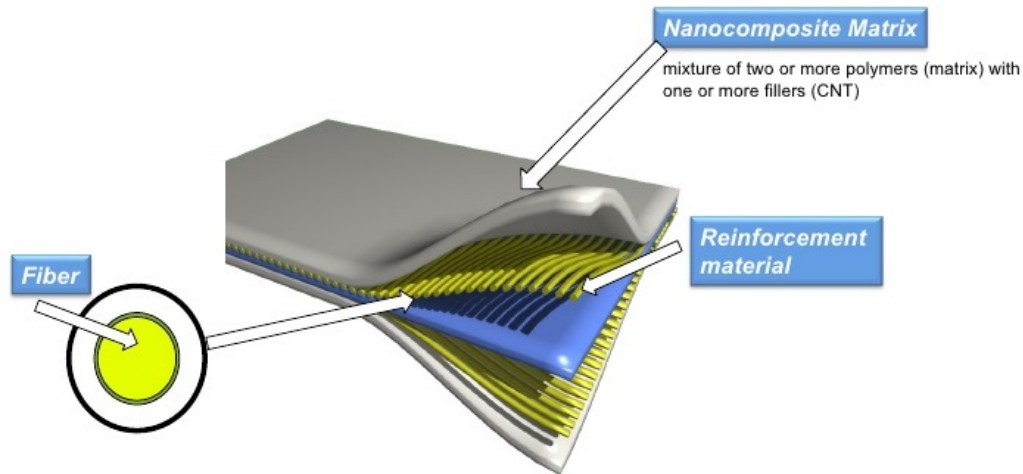


FIGURE 2.2: Structure of a nanoreinforcement with a matrix to create a nanocomposites (L.S. Brinson and W.G Sawyer 2015)

Furthermore, at nano-scale dimensions the interaction at the interfacial region is improved and therefore improving the material properties. In this context, the surface area/volume ratio of reinforcement materials employed in the preparation of nanocomposites is crucial to the understanding of their structure property relationships [31]. Further, discovery of CNTs (carbon nanotubes) and their subsequent use to fabricate

composites exhibiting some of the unique CNT related mechanical, thermal and electrical properties added a new and interesting dimension to this area. Figure 2.2 shows a structure of a nanoreinforcement with a matrix to create a nanocomposites.

### 2.2.1 Nanocomposites applications

Pedro Henrique[33] studied the synthesis, structure, new application opportunities and properties of nanocomposites[33]. In his unified overview the three types of matrix nanocomposites were presented underlining the need for these materials, their processing methods and some recent results on structure, properties and potential applications, perspectives including need for such materials in future space missions and other interesting applications together with market and safety aspects[33].

Possible uses of natural materials such as clay based minerals, chrysotile and lignocellulosic fibers were highlighted. Being environmentally friendly, Pedro study found that applications of nanocomposites offer new technology and business opportunities for several sectors of the aerospace, automotive, electronics and biotechnology industries[33]. The study therefore concluded that nanocomposites are suitable materials to meet the emerging demands arising from scientific and technologic advances.

In 2013, Charles Chikwendu [34] did a study on the properties of nanocomposites. The research showed that nanocomposites have broadened significantly to encompass a large variety of systems such as one-dimensional, two-dimensional, three-dimensional and amorphous materials, made of distinctly dissimilar components and mixed at the nanometer scale[34]. This research presents a detailed definition of nanocomposites, its origin, classification, properties, benefits, as well as its future.

The application possibilities of nanocomposites for packaging was shown by the study including food and non-food films and rigid containers[34]. In the engineering plastics arena, a host of automotive and industrial components can be considered, making use of lightweight, impact, scratch-resistant and higher heat distortion performance characteristics[34]. In plastics the advantages of nanocomposites over conventional ones do not stop at strength. The high heat resistance and low flammability of some nanocomposites also make them good choices to use as insulators and wire coverings[34]. Nadeesh Madusanka[35] prepared a dielectric nanocomposite based on cyanoethylated-cellulose (CRS) and montmorillonite (MMT) nanoclay with different weight percentages (5%, 10% and 15%) of MMT[35]. MMT nanoplatelets obtained via sonication of MMT nanoclay in acetone for a prolonged period was used in the preparation of CRS-MMT nanocomposites[35]. CRS-MMT thin films on SiO<sub>2</sub>/Si wafers were used to form metal-insulator-metal (MIM) type capacitors. At 1 kHz CRS-MMT nanocomposites exhibited

high dielectric constants ( $\epsilon$ ) of 71, 55 and 42 with low leakage current densities ( $106107 \text{ A/cm}^2$ ) for nanocomposites with 5%, 10% and 15% weight of MMT respectively, higher than values of pure CRS (21), Na-MMT(10) [35]. Reduction of  $\epsilon$  with higher MMT loading can be attributed to a network formation as evidenced via strong bonding interactions between CRS and MMT leading to a lower molecular mobility[35]. The leakage was studied using conductive atomic force microscopy (C-AFM) indicated that leakage pathways were associated with MMT nanoplatelets embedded in the CRS polymer matrix[35].

### 2.2.2 Nanocomposites Properties

S. Anandhan[36] conducted a study on the properties of nanocomposites. The study showed that in nanocomposites, as dimensions reach the nanometer level, interactions at the interfacial region become largely improved, and this is important to enhance materials properties[36]. In this context, the surface area/volume ratio of reinforcement materials employed in the preparation of nanocomposites is crucial to the understanding of their structure property relationships.

Further this research showed that discovery of CNTs (carbon nanotubes) and their subsequent use to fabricate composites exhibiting some of the unique CNT related mechanical, thermal and electrical properties added a new and interesting dimension to this area[36]. The possibility of spinning CNTs into composite products and textiles made further inroads for the processing and applications of CNT-containing nanomaterials. The study also showed that rubber based nanocomposites are attracting considerable interest in polymer science research. Incorporation of different nanoreinforcements such as layered silicate clays, carbon nanotubes, nanofibers and silica nanoparticles into elastomers significantly enhances their mechanical, thermal, dynamic mechanical, and barrier properties along with noticeable improvements in adhesion, rheological and processing behavior[36].

In 2016, Farzana Hussain[37] also made a review of nanocomposites processing, manufacturing and applications[37]. In addition to presenting the scientific framework for the advances in polymer nanocomposite research, this review focused on the scientific principles and mechanisms in relation to the methods of processing and manufacturing with a discussion on commercial applications and health/safety concerns (a critical issue for production and scale-up) [37]. Hence, this review offered a comprehensive discussion on technology, modeling, characterization, processing, manufacturing, applications, and health/safety concerns for polymer nanocomposites[37].

Dimitirios G. Papageorgiou[3] examined the current status of the intrinsic mechanical properties of the graphene-family of materials along with the preparation and properties of bulk graphene based nanocomposites[3]. The usefulness of Raman spectroscopy for the characterization and study of the mechanical properties of graphene flakes and their composites was clearly exhibited[3]. Furthermore, the preparation strategies of bulk graphene based nanocomposites were discussed and the mechanical properties of nanocomposites reported in the literature were analyzed[3].

K. Naresh [38] carried out experiments to determine the tensile strength of laminates, for three different orientations of glass/epoxy and carbon/epoxy composites. Using two-parameter Weibull distribution, the theoretical tensile strength values are determined for Glass Fiber Reinforced Polymer (GFRP) and Carbon Fiber Reinforced polymer (CFRP) composites for different strain rates by a linear curve fitting[38]. The theoretical and experimental values matched well. The deviation between the theoretical and experimental values was less than 12% for GFRP laminates and less than 13% for CFRP laminates[38]. Normally the mean values of mechanical properties are sufficient to use theoretical models, whereas all tested specimen data are considered (including the mean values) in the Weibull distribution[38]. Therefore, Weibull distribution contains more information and it will be useful for designers and composite manufacturers to ensure the reliability of structures[38].

In particular, through the analysis of several hundred literature papers on graphene composites, Dimitirios G. Papageorgiou found a unique correlation between the filler modulus, derived from the rule of mixtures, and the composite matrix[3]. This correlation was found to hold true across a wide range of polymer matrices and thus suggested that the common assumption that the filler modulus was independent of the matrix was incorrect, explaining the apparent under performance of graphene in some systems[3]. The presence of graphene even at very low loadings can provide significant reinforcement to the final material, while the parameters that affect the nanocomposite strongly were thoroughly reviewed[3]. Finally, the potential applications and future perspectives were discussed with regard to scale up capabilities and possible developments of graphene-based nanocomposite materials[39].

Incorporation of different nano-reinforcements such as layered silicate clays, carbon nanotubes, nanofibers, graphene and silica nanoparticles into elastomers significantly enhances their mechanical, thermal, dynamic mechanical, and barrier properties along with noticeable improvements in adhesion, rheological and processing behaviour [32]. Nowadays, nanocomposites offer new technology and business opportunities for all sectors of the industry, in addition to being environmental- friendly.

In 2017, O. Richard Alonge[40] conducted a study on the compressive strength and durability potentials of hybrid cementitious composites (HCC) that contain metakaolin (MK). The HCC specimens contain 10% metakaolin (MK), 1% colloidal nanosilica (CNS) and 1% epoxy resins and the specimens were examined for early ages of 7, 28, and 90 days of exposure in both water and seawater[40]. The durability properties investigated in this research study comprise of water absorption, intrinsic air permeability, chloride penetration and porosity. All tests were conducted to assess the influence of MK, CNS and epoxy on the compressive strength and the durability properties of the HCC specimens[40]. The result showed that HCC specimens with 10% MK, 1% CNS was durable relative to all the properties such as Young's Modulus and Elastic Modulus [40]. Nevertheless, the addition of both natural fibers (coconut and oil palm fruit bunch fibers) and synthetic fiber (bar chip fiber) had a slight negative impact on the durability properties of HCC specimens. Conclusively, the results showed that the menace of water, liquid and gas transportation by water absorption, capillary suction, porosity, chloride penetration, and intrinsic air permeability of HCC were lesser than that of the control specimen[40].

### **2.2.3 Preparation of Nanocomposites**

Zapata Etal [2] conducted a study on nanocomposites and explained that the preparation of nanocomposites can be done by three ways, which are solution blending, the molten state, and in situ polymerization. They pointed out that the latter consists in placing the monomer and the catalyst between the clay layers and polymerization takes place in the gap. As polymerization progresses, the spacing between the clay's layers increases gradually and the dispersion state of the clays changes from intercalated (the ordered of layered silicate gallery is retained) to exfoliated (delamination with destruction of the clay sheet order)[2]. The advantages of this method are the one step synthesis of the metallocene polymer nanocomposites, improved compatibility of the clay and the polymer matrix and enhanced clay dispersity.

Nanocomposites can also be prepared by dispersing nano-particles into a host polymer. This process is also termed exfoliation[41]. When the nano-particles are substantially dispersed, it is known to be exfoliated. Exfoliation is facilitated by surface compatibility chemistry[42], which expands the nano-particles to the point where individual particles can be separated from one another by mechanical shear as shown in Figure 2.3.

Nanocomposites can again be prepared using both thermoplastic and thermoset polymers, and the specific compatibility chemistry designed and employed are necessarily a function of the host polymers unique chemical and physical characteristics [43]. In

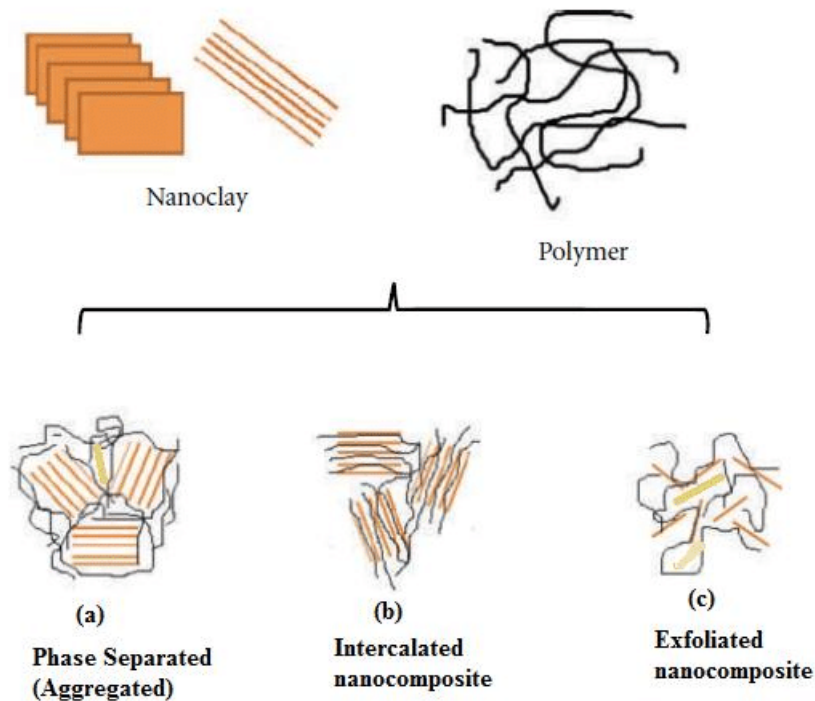


FIGURE 2.3: Different types of dispersion of clay layers in polymer matrix[2].

some cases, the final nanocomposite will be prepared in a reactor during the polymerization stage. For other polymer systems, processes have been developed to incorporate nano-particles into a hot-melt compounding operation[42].

In general, nanocomposites exhibit gains in barrier, flame resistance, structural, and thermal properties yet without significant loss in impact or clarity. Because of the nanometer-sized dimensions of the individual platelets in one direction, exfoliated nanoparticles are transparent in most polymer systems[44]. However, with surface dimensions extending to one micron, the tightly bound structure in a polymer matrix is impermeable to gases and liquids, and offers superior barrier properties over the neat polymer[45]. Nanocomposites also demonstrate enhanced fire resistant properties and are finding increasing use in engineering plastics.

With the proper choice of compatibility chemistries, the nanometer-sized particles interact with polymers in unique ways. Application possibilities for packaging include food and non-food films and rigid containers. In the engineering plastics arena, a host of automotive and industrial components can be considered, making use of lightweight, impact, scratch-resistant and higher heat distortion performance characteristics[46].

N. Saba and M. Jawaid[3] used a novel flame retardant nano filler developed from oil palm empty fruit bunch (OPEFB) fibre for the fabrication of nanocomposites. The nanocomposites were prepared by dispersing 1, 3 and 5 wt.% nano OPEFB filler in

an epoxy matrix using a high speed mechanical stirrer[3]. Physical, structural, and thermomechanical analyses of the obtained nano OPEFB/epoxy nanocomposites were carried out and the results were compared with those for pure epoxy composites[3]. Their findings revealed that the incorporation of the nano OPEFB filler in the epoxy matrix increased the density of the nanocomposites from 1.13 to 1.25  $g/cm^3$  [3]. The pattern of the pure epoxy composites displayed sharp and highly intense peaks at a  $2\theta$  value of  $21^\circ$ , whereas all OPEFB/epoxy nanocomposites showed relatively less intense peaks that shifted to lower  $2\theta$  values[3]. The coefficient of thermal expansion of the epoxy composites decreased with increasing OPEFB nano filler content up to 3%, while beyond 3% it slightly increased[3]. Overall, the results revealed that the thermomechanical properties reached maximum values for 3% loading, due to homogeneous dispersion and improved interfacial bonding between the epoxy and the dispersed nano OPEFB filler[3] as shown in Figure 2.4.

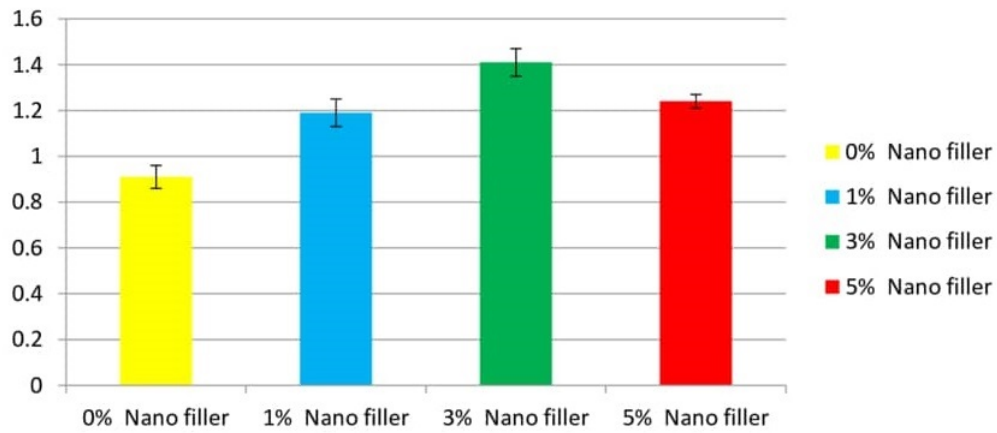


FIGURE 2.4: Effect of nano OPEFB filler loading on tensile strength of epoxy composites[3].

In 2017, Jaemin Cha[47] conducted research on the improvement of modulus, strength and fracture toughness of CNT/Epoxy nanocomposites through the functionalization of carbon nanotubes[47]. The CNTs were functionalized by attaching melamine to improve the dispersibility in epoxy matrix and to enhance the interfacial bonding between CNTs and matrix[47]. The tensile tests and single edge notch bending (SENB) tests were performed for CNT/Epoxy and Multiwalled-CNT/Epoxy nanocomposites at various weight fractions of functionalized CNTs[47].

The M-CNT/Epoxy nanocomposites with addition of 2wt% functionalized CNTs exhibited enhancements of Young's modulus by 64% and ultimate tensile strength by 22%. Furthermore, a significant increase of fracture toughness by 95% was observed for 2wt% M-CNT/Epoxy nanocomposite[47]. The homogeneity of CNTs in epoxy matrix has been

analyzed and related to the improvement of modulus and strength[47]. The phenomena of crack propagation has been investigated and related to the improvement of fracture toughness[47].

Refik Arat[48] conducted a study using the melt blending method to prepare the polystyrene nanotubes (PS/NTs) nanocomposites instead of in-situ bulk polymerization of styrene monomer in the presence of HNTs[48]. Surface modification of HNTs with styrene-maleic anhydride copolymers (SMA) was performed in the medium to improve the HNTs distribution and compatibility in the PS matrix. PS/HNTs nanocomposites were prepared in a twin-screw micro compounder containing 5, 10, and 15 wt.% of nanoclays[48]. The influences of the surface modification of HNTs on the properties of the nanocomposites were studied by XRD, SEM, DSC, TGA, and tensile test.

The SEM images showed that the modified HNTs samples were uniformly distributed in the PS matrix compared to the pristine HNTs[48]. The thermal stability of nanocomposites was also improved by increasing of modified HNTs content[48]. Consequently, the surface modification increased the dispersion of HNTs in the PS nanocomposites prepared by melt blending method[48].

C Ziming and X Wang[4] also studied the hierarchical-structured dielectric permittivity and breakdown performances of polymer-ceramic nanocomposites. Polymer-ceramic nanocomposites with high dielectric permittivity, breakdown strength and energy storage density are of urgent demand in advanced electronics industry[4]. The interface between polymer matrix and ceramic fillers plays an essential role in dielectric performances of nanocomposite due to the interfacial polarization[4].

In this contribution, four types of nanocomposites with different hierarchical structures, namely poly vinylidene fluoride (PVDF) with BaTiO<sub>3</sub> nanofibers, TiO<sub>2</sub> nanofibers, BT nanoparticles inside TO nanofibers, BT nanofibers inside TO nanofibers are proposed[4]. The dielectric permittivity and breakdown strength were respectively calculated through a finite element method and a phase field method. Results indicated that as the volume fraction of ceramic increases, the dielectric permittivity raises while the breakdown strength decreases[4] as shown in Figure 2.5.

Nanocomposites with *BT<sub>n</sub>fs* (BaTiO<sub>3</sub>) show the highest dielectric permittivity but lowest breakdown strength. Meanwhile nanocomposites with *TO<sub>n</sub>fs* perform exactly the opposite way[4]. Nanocomposites with *TO<sub>n</sub>fs@BT<sub>n</sub>fs* demonstrated both high dielectric permittivity and breakdown strength[4].

Hyuk-Gi Lee[49] conducted a study using modified cellulose nanocrystals (AF-CNCs) with (3-aminopropyl) triethoxysilane (APTES) to prepare poly (amic acid)/AF-CNC nanocomposite films by spin coating[49]. To convert poly (amic acid) into polyimide

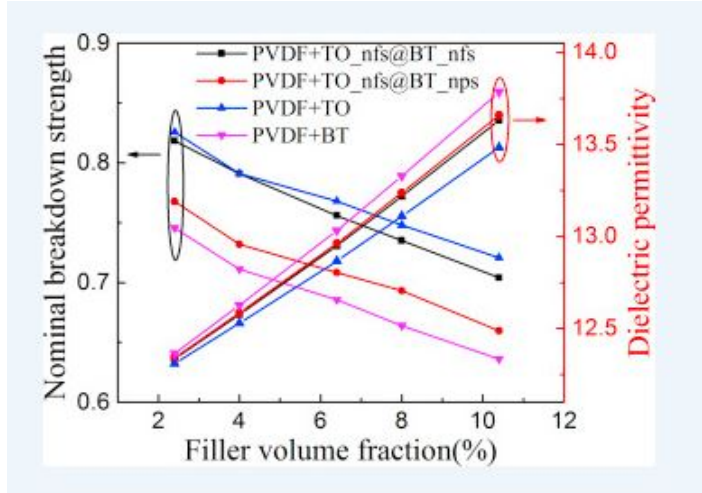


FIGURE 2.5: The dielectric permittivity and nominal breakdown strength of all these four types nanocomposites as a function of filler volume fraction[4].

(PI), the films were thermally imidized after spin coating. The effects of AF-CNC content on the tensile properties, thermo-mechanical properties, optical transmittance, morphology and barrier properties of PI/AF-CNC nanocomposite films were investigated[49]. With increasing content of AF-CNC from 0 wt% to 3 wt%, tensile modulus and storage modulus of PI/AF-CNC nanocomposite films increased without decrease in their optical transmittance[49]. The water vapor transmission rate and tan peak height of PI/AF-CNC nanocomposite films decreased with increasing AF-CNC content from 0 wt% to 3 wt%[49]. For comparison, PI/CNC nanocomposite films with 2 wt% of unmodified CNC were also prepared. PI/AF-CNC (2 wt%) nanocomposite films showed better mechanical and physical properties than PI/CNC (2 wt%) nanocomposite films[49].

### 2.3 Nanocomposites interfacial region

Using nanocomposites in designing critical applications requires an understanding of their structure property function relationships[50]. Furthermore, the ability to tailor the nanoreinforcement/matrix interaction and an understanding of the impact that the interfacial region has on macroscopic properties are important to obtaining nanocomposites with the desired properties[50].

### 2.3.1 Matrix and Nanoreinforcement Interaction within the Interfacial region

Understanding the nature and chemistry of the interfacial region introduces tailor ability of the nanocomposite, providing compatibility with a number of different polymer matrices[51]. Tailoring is often achieved by grafting short molecules or polymer chains with precise chemical structure from the nanoparticle surface[52]. Korley et al [51] reported the tailor ability of an elastomeric polyurethane nanocomposite through selective interactions between a layered silicate clay and the matrix as shown in Figure 2.6.

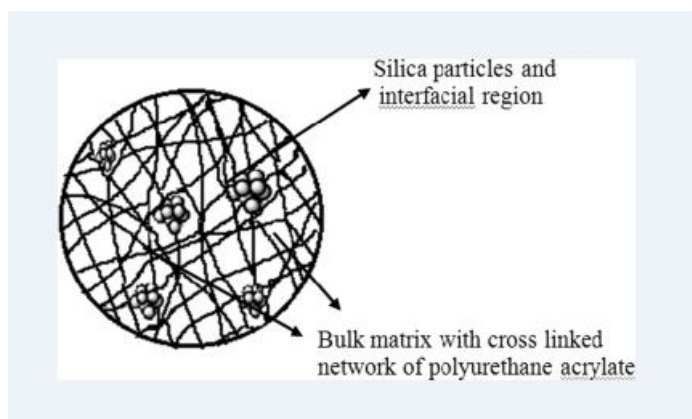


FIGURE 2.6: Silicate nanoreinforcement polymer nanocomposite interfacial region

Their research found that in one system, the hydrophilic polar soft block polyurethane segments dominated the clay/polyurethane interactions[51]. In this case, strain induced alignment of the soft segment chains was suppressed within the nanocomposite, resulting in a reduction of polymer toughness and extensibility, as compared to the neat resin[53]. Comparably, the silicate layers in a polyurethane containing a hydrophobic soft segment resulted in the clay favouring interaction with the hard segment. This morphology offered enhanced polymer toughness and modulus[51].

### 2.3.2 Enhancement of Polymer Properties due to Nano-filler

Enhancements in polymer properties as a result of nano-filler addition vary from polymer to polymer and can be dependent on the level of nanoreinforcement dispersion[50]. Increased strength, modulus, barrier properties, and dimensional stability have been observed in most systems as a result of dispersing the rigid nanoparticle in the softer polymer matrix[54]. However, many nanocomposites exhibit a toughness lower than the corresponding neat resin[51].

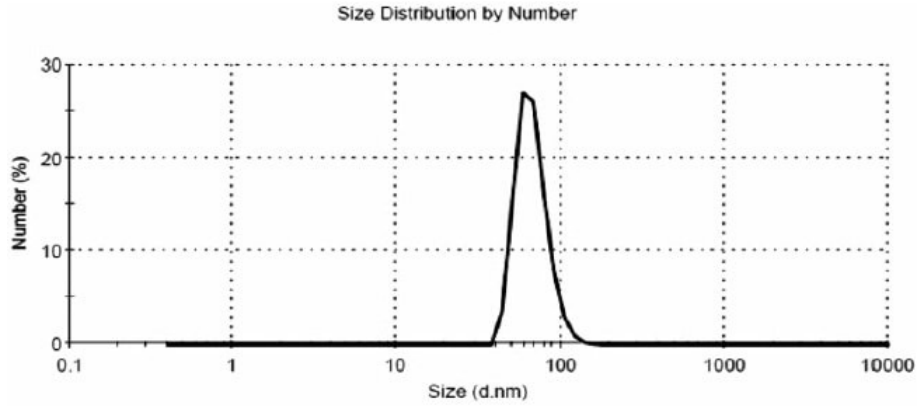


FIGURE 2.7: Particle size distribution size within a nanocomposite [2].

Drzal [55] dispersed layered nano-particles into an amine cured diglycidyl ether of bisphenol A (epoxy resin). The research showed the variation of the nanoparticle size with the number of nanoparticles as shown in Figure 2.7. They reported a 50% increase in the room temperature storage modulus at a 10 wt% clay loading[55]. Enhancements in the tensile strength were only observed with 2.5 wt% loading, and the impact strength was radically decreased with increasing clay loading[55].

Bao et al.[56] also reported a reduction in impact toughness following dispersion of nanoreinforcement in high density polyethylene, where the reduction in toughness corresponded with an increase in Young's modulus[56]. A reduction in impact toughness was also observed on clay dispersion in HDPE as well as in rubber toughened HDPE[57]. Other researchers have noted that the negative influence of the nanoreinforcement on toughness is not observed when testing above the glass transition temperature. Misra et al[15] reported that the addition of clay to polypropylene increased the impact strength in the temperature range, whereas the clay had little to no effect at higher temperatures.

Pinnavaia [58] noted that flexible resin systems with low glass-transition temperature ( $T_g$ ) showed a much larger increase in modulus and tensile strength with the addition of an organoclay, than did rigid systems. Giannelis et al [58] provided experimental evidence that tensile loading of a nanocomposite at a temperature much higher than  $T_g$ , allowed nanoparticle alignment in the direction of the stress and thereby provided a mechanism for energy dissipation[59].

Generalized statements regarding the strength of the polymer-graphene interface may be made by examining the nanocomposite fracture surface at break. Drzal et al [60] worked to improve the graphite interface and dispersion in a polypropylene matrix. They functionalized graphite by application of a PP coating onto the graphite surface, followed by sonication in alcohol to reduce aggregate size[60].

Zheng and Wong[61] dispersed both graphite and expanded graphite into a polymethyl matrix and compared the electrical conductivity of the resulting nanocomposites[62]. The percolation threshold was reached at 1 wt% loading of the expanded graphite, whereas addition of 3.5 wt% graphite was necessary for conductivity[61]. The conductivity after percolation was an order of magnitude greater for the expanded graphite composites as compared to the graphite composites. This difference was attributed to the greater dispersion of the expanded graphite[61].

Ke Chu and Xiao-hu Wang[5] investigated the thermal properties of graphene/metal composites with aligned graphene. Graphene holds great potential in metal matrix composites for thermal management due to its excellent thermal properties[5]. However, the graphene/metal composites possessing both high thermal conductivity (TC) and low coefficient of thermal expansion (CTE) have not yet been realized[5]. Herein, Ke Chu and Xiao-hu Wang reported an efficient strategy to achieve a high alignment of graphene nanosheets (GNSs) in GNS/Cu composites through a vacuum filtration method followed by spark plasma sintering[5] shown in Figure 2.8. Because of the highly aligned GNSs and laminated structure, the GNS/Cu composites exhibited notably anisotropic thermal properties[5]. Intriguingly, the composites showed a reversed anisotropic behavior between TC and CTE as a function of GNS fraction, in which the in-plane TC was substantially higher than through-plane TC, whereas oppositely the through-plane CTE displayed a larger drop than in-plane CTE[5]. Promisingly, the composite with 30 vol% GNSs delivered a high in-plane TC of 458 W/mK and a low through-plane CTE of 6.2 ppm/K, corresponding to a 35 % TC enhancement and a 64 % CTE reduction compared to pure Cu, respectively[5]. The present GNS/Cu composites with high in-plane TC and low through-plane CTE are promising candidates for specific thermal management applications that require an efficient inplane heat dissipation but a good through-plane dimensional stability[5].

Kim et al [63] added 10 wt% of expanded graphite to a polystyrene matrix. The graphite was initially intercalated with potassium metal of varying molar ratios to expand the distance between graphene layers[63]. They provided Extensively Drug Resistant (XRD) and Transmission Electron Microscopy (TEM) analysis. Both suggested that the graphite remained aggregated in groups of several graphene layers in 50 thickness. Regardless of the poor dispersion, they reported over 100-fold improvement in conductivity[64].

She et al.[65] employed an unsaturated polyester resin to modify expanded graphite. The modified graphite was then powdered into small particles to facilitate dispersion in a high density polyethylene matrix. In this case, percolation was reached at 5.7 wt% of the modified expanded graphite, whereas 22 wt% of the conventional expanded graphite was required to reach percolation[65].

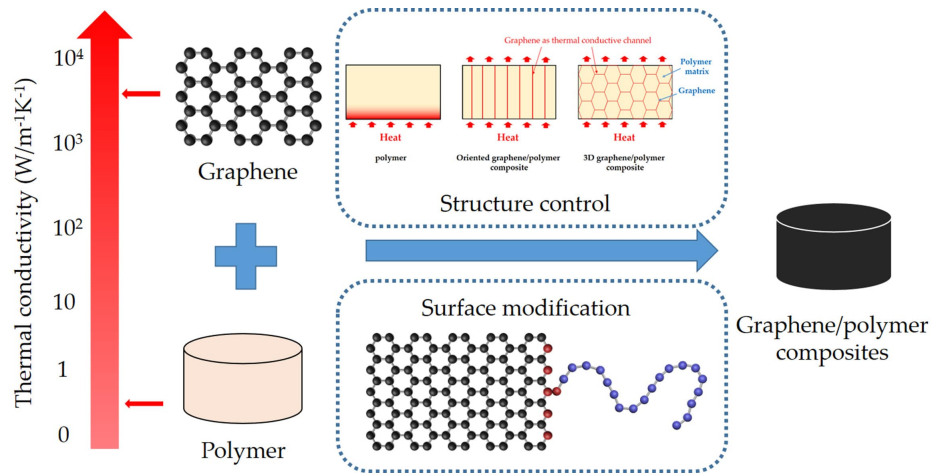


FIGURE 2.8: Thermal properties of graphene/metal composites with aligned graphene[5].

Drzal,[66] dispersed expanded graphite into a high temperature, thermosetting, polyimide (PETI-5). The graphite particle size was reduced by sonication, then further reduced by vibratory ball-milling. They reported a significant increase in storage modulus as graphite concentration increased, and particle size decreased[66].

Yasmin and Daniel,[67] however, observed negative effects on the mechanical performance of graphite nanocomposites from continued sonication. They reported reinforcing epoxy with 1-2 wt% of EG by direct mixing, sonication, shear mixing, and a combination of shear and sonication[68]. They found that combining shear mixing with 52 sonication produced enhanced resin elastic modulus and tensile strength. However, as sonication times were increased, the mechanical properties degraded[67].

## 2.4 Materials

## 2.5 Graphene

Graphene is a single layer of carbon atoms packed in a hexagonal (honeycomb) lattice, with a carbon-carbon distance of 0.142 nm [69]. It is the first truly two-dimensional crystalline material and it is representative of a whole class of 2D materials including for example single layers of Boron-Nitride (BN) and Molybdenum-disulphide ( $\text{MoS}_2$ )[70], which have both been produced after 2004 [69].

Figure 2.9 Below shows the schematic of a graphene sheet. A review of recent research papers by Chun Hung Lui[6], investigating the mechanical and vibration properties of graphene by various techniques, including atomic-force microscopy (AFM)[71], Raman,

infrared (IR) and ultrafast optical spectroscopy concluded that graphene exhibits remarkable physical mechanical properties even though it is governed by strong Van Der Waal forces [6].

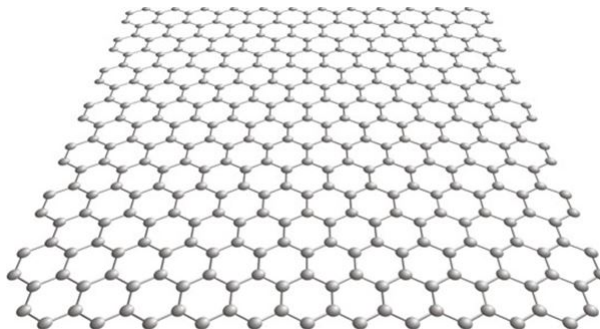


FIGURE 2.9: Graphene sheet [6]

### 2.5.0.1 Graphene Fabrication

Earlier attempts to isolate graphene concentrated on chemical exfoliation. To this end, bulk graphite was first intercalated (to stage I)[72] so that graphene planes became separated by layers of intervening atoms or molecules. This usually resulted in new 3D materials[72]. However, in certain cases, large molecules could be inserted between atomic planes [73], providing greater separation such that the resulting compounds could be considered as isolated graphene layers embedded in a 3D matrix[74].

There are recent attempts to improve the quality and yield of exfoliation techniques. These include stamping methods which use silicon pillars to transfer graphene flakes and electrostatic voltage assisted exfoliation which uses electrostatic forces to controllably separate graphene from bulk crystals [75]. These are very recent developments and only time will tell whether they yield significant improvement over standard exfoliation[76].

Another common graphene fabrication technique is to disperse graphene from solution. In this method graphite flakes are sonicated in a solution and then dispersed onto a wafer[77]. An AFM (Atomic Force Microscopy) is used to locate individual sheets making this technique very time consuming as shown in Figure 2.10 relative to the optical detection scheme[75]. Long sonication times are needed to break the graphite down and this typically results in small flakes. Recently a similar technique was used to fabricate graphene ribbons with nm-scale widths[7].

One of the difficulties in dispersing graphene from solution is separating the layers without breaking them. A way around this is to intercalate the graphite and dissolve it in a solvent[78]. When the intercalant dissolves it separates the graphene sheets[79]. This

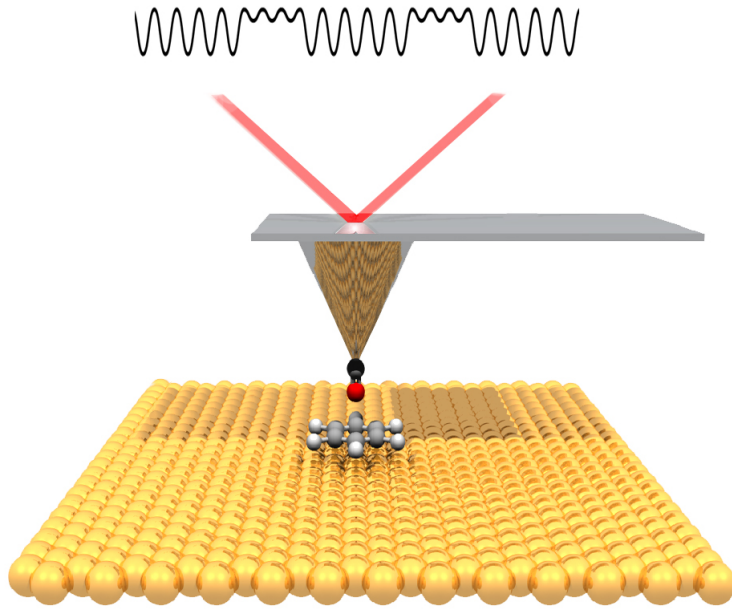


FIGURE 2.10: An AFM (Atomic Force Microscopy) is used to locate individual sheets[7]

technique was shown to work effectively for graphene oxide. However, the success of similar techniques on graphene is limited due to the chemistry required to keep individual graphene sheets from aggregating in solution[80].

Long Chen Tang in 2013[39] investigated the effect of dispersion state of graphene on mechanical properties of graphene/epoxy composites[39]. The graphene sheets were exfoliated from graphite oxide by thermal reduction. Different dispersions of graphene sheets were prepared with and without ball mill mixing[39]. It was found that the composites with highly dispersed graphene sheets showed higher glass transition temperature ( $T_g$ ) and strength than those with poorly dispersed graphene sheets, although no significant differences in both the tensile and flexural moduli were caused by the different dispersion levels. In particular, the  $T_g$  was increased by nearly  $11^{\circ}C$  with the addition of 0.2 wt.% well dispersed graphene to epoxy[39].

As expected, the highly dispersed graphene sheets also produced one or two orders of magnitude higher electrical conductivity than the corresponding poorly dispersed graphene[81]. Furthermore, an improved quasi-static fracture toughness was measured in the case of good dispersion[81]. The poorly and highly dispersed graphene sheets at 0.2 wt.% loading resulted in about 24% and 52% improvement in quasi-static fracture toughness of cured epoxy thermosets, respectively[81]. Graphene sheets were observed to bridge the micro-crack and debond/delaminate during fracture process due to the poor filler/matrix and filler/filler interface, which should be the key elements of the toughening effect[81].

In 2013 Yan Jun Wan[82] prepared epoxy composites filled with both graphene oxide (GO) and diglycidyl ether of bisphenol-A functionalized GO (DGEBAfGO) sheets at different filler loading levels[82]. The correlations between surface modification, morphology, dispersion/exfoliation and interfacial interaction of sheets and the corresponding mechanical and thermal properties of the composites were systematically investigated[82]. The surface functionalization of DGEBA layer was found to effectively improve the compatibility and dispersion of GO sheets in epoxy matrix[82]. The tensile test indicated that the DGEBAfGO/epoxy composites showed higher tensile modulus and strength than either the neat epoxy or the GO/epoxy composites[82].

In this research by Yan Jun Wan[82], for epoxy composites with 0.25 wt% DGEBA, the tensile modulus and strength increased from 3.15 GPa to 3.56 GPa and 52.98 Mpa to 92.94 MPa[82], respectively, compared to the neat epoxy resin. Furthermore, enhanced quasi-static fracture toughness was measured in case of the surface functionalization[82]. The GO and DGEBAfGO at 0.25 wt% loading produced 26% and 41% improvements in KIC values of epoxy composites, respectively[82]. Fracture surface analysis revealed improved interfacial interaction between DGEBAfGO and matrix[82]. Moreover, increased glass transition temperature and thermal stability of the DGEBAfGO/epoxy composites were also observed in the dynamic mechanical properties and thermo-gravimetric analysis compared to those of the GO/epoxy composites[82].

### 2.5.1 Graphene Properties

Nabil A. Abdel Ghany[83] conducted a study on the revolution of graphene for different applications[83]. The study showed that this one-atom-thick crystal of carbon has distinctive physicochemical properties, tremendous mechanical performance and outstanding electrical and thermal conductivities[83]. These characteristics are making graphene as an alternative to replace many traditional materials for many applications. There are different methods to fabricate and characterize 2D graphene, some of these methods are currently scalable and others still on the lab scale[83]. This state-of-the-art, aimed to achieve three goals: that is provide a background that is easy to follow, to make a short survey on graphene history, properties, and different preparation methods, and current and future applications of graphene and graphene based materials[83].

In 2017, Ting Wang[84] studied the effect of different sizes of graphene on thermal transport performance of graphene paper[84]. The study showed that as a two dimensional material, graphene attracts great attention as heat dissipation material due to its excellent thermal transport property[84]. Herein, three kinds of graphene papers

were fabricated with three different thickness graphene nanoplatelets (GNP) by simple vacuum filtration method[84].

The effects of the different size of GNP on the thermal conductivity of graphene papers were investigated systematically[84]. The in-plane thermal conductivity of GNP-7 (the thickness of GNP approximately 7 nm) paper achieved  $149.2 \text{ Wm}^{-1}\text{K}^{-1}$ , was about 7 times compared to that of GNP-3 (3 nm) and GNP-5 (5 nm), which indicated that thermal conductivity of graphene film increased with increasing the thickness of GNP[84]. Furthermore, the in-plane thermal conductivity of GNP-7 could be increased by 25% and raised up to  $187.4 \text{ Wm}^{-1}\text{K}^{-1}$  after cold-compaction as cold-compaction will further tighten the loose stacked layers, making the paper more anisotropic in heat conduction[84]. The excellent heat conductive properties of the paper are expected to use as efficient heat spreader for thermal management applications[84].

Yuka Takag[8] also investigated the size, shape, and number density of deposits in the deposition of graphene on highly oriented pyrolytic graphite substrates by the graphene solution liquid droplet method[8] explained in Figure 2.11. Block-shaped aggregates of graphene and sheet-like graphene deposits were observed[8]. The number density of the block-shaped graphene was about 50 times larger than that of the sheet-like graphene due to the aggregation of the graphene films in the pristine graphene solution[8]. Ultrasonication fragmented the block-shaped graphene and increased the number density of sheet-like graphene by about ten times[8]. The remaining block-shaped graphene with heights greater than 25 nm was almost eliminated selectively by centrifugation[8].

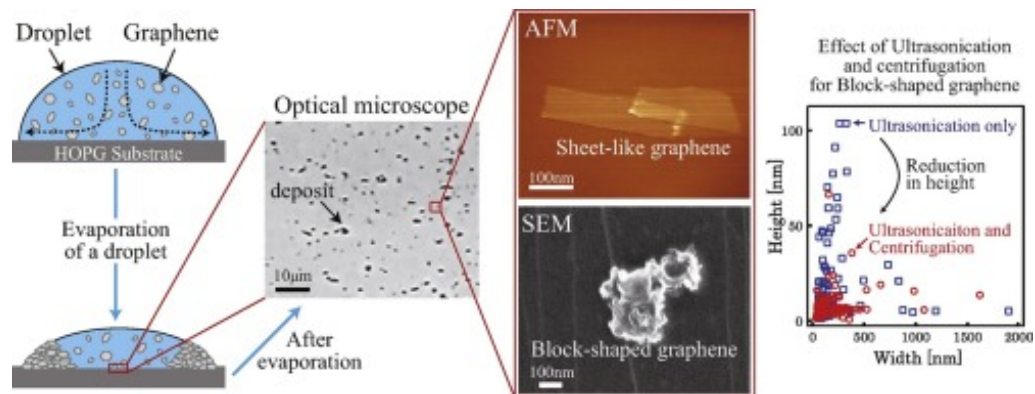


FIGURE 2.11: Investigation of the size, shape, and number density of deposits in the deposition of graphene on highly oriented pyrolytic graphite substrates[8]

In 2015, Junwei Gu[85] used graphite nanoplatelets (GNPs) to fabricate GNPs/bisphenol-A epoxy resin (GNPs/E-51) nanocomposites with high thermal conductivity by casting method[85]. The two-step method of methanesulfonic acid/c-glycidoxypropyltrimethoxysilane (MSA/KH-560) was introduced to functionalize the surface of GNPs (fGNPs). The KH-560 molecules were successfully grafted onto the surface of GNPs[85]. The thermal

conductivities of the fGNPs/E-51 nanocomposites was increased with the increasing addition of fGNPs, and the corresponding thermally conductive coefficient of the fGNPs/E-51 nanocomposites was improved to 1.698 W/mK with 30 wt% fGNPs, 8 times higher than that of original E-51 matrix[85]. The flexural strength and impact strength of the fGNPs/E-51 nanocomposites are optimal with 0.5 wt% fGNPs[85]. The thermal stabilities of the fGNPs/E-51 nanocomposites were also increased with the increasing addition of fGNPs. For a given GNPs loading, the surface functionalization of GNPs by MSA/KH-560 exhibited a positive effect on the thermal conductivities and mechanical properties of the nanocomposites[85].

Yan-Jun Wan[86] also fabricated epoxy composites with highly dispersed graphene by a facile surfactant-assisted process, and investigated the correlations between surface modification, morphologies, dispersion, re-agglomeration behavior and interfacial interaction of graphene and the corresponding thermal and mechanical properties of the composites[86]. It was found that the surfactant treatments of graphene were effective to improve their dispersion stability in water and inhibit their re-agglomeration during the curing of resin[86].

Scanning and transmission electron microscopy analysis demonstrated that the dispersion/exfoliation level of graphene in the composites was greatly improved after surface treatments[86]. These above ameliorating effects along with improved interface between the matrix and graphene arising from the hydrophilic and hydrophobic molecules of non-ionic surfactant resulted in increased tensile properties compared with those without surface modification[86].

In 2014, Yan-Jun Wan[14] then investigated the effects of Graphen Oxide (GO) and silane functionalized GO (silane-f-GO) loading and silane functionalization on the mechanical properties of epoxy composites and compared[14]. Such silane functionalization containing epoxy ended-groups was found to effectively improve the compatibility between the silane-f-GO and the epoxy matrix[14]. Increased storage modulus, glass transition temperature, thermal stability, tensile and flexural properties and fracture toughness of epoxy composites filled with the silane-f-GO sheets were observed compared with those of the neat epoxy and GO/epoxy composites[14].

The findings of this research confirmed the improved dispersion and interfacial interaction in the composites arising from covalent bonds between the silane-f-GO and the epoxy matrix[14]. Moreover, several possible fracture mechanisms, i.e. crack pinning/deflection, crack bridging, and matrix plastic deformation initiated by the debonding/delamination of GO sheets, were identified and evaluated[14].

Junsu Lee[87] conducted a study on two-dimensional van der Waals materials such as graphene and hexagonal boron nitride. The two-dimensional material of polyphenylene superhoneycomb network (PSN) was of similar interest because it is a type of periodic porous graphene. In this research[87], it was reported a first-principles study of the geometric and electronic properties of vertical heterostructures comprising graphene and PSN. AA, AA0, and AB stacking configurations of a graphene sheet on a PSN sheet produce band gaps of 63, 16, and 3 meV, respectively[87]. Jansu also determined the relationships between the band gap and the interlayer distance between the graphene and PSN sheets[87]. Finally, computationally simulated scanning tunneling microscopy images were presented, which indicate the local electronic structures of the surfaces of the graphene and PSN sides[87].

In 2017, H. Li and Y.J. Zeng[88] presented a comparative study of magnetoresistance (MR) behaviors in few-layer graphene (FLG) and multilayer graphene (MLG) with various thicknesses[88]. A maximum MR as large as 9500% was observed in a 23 nm sample at 2.5 K, with a non-saturating linear characteristic up to 7 T[88]. MR decreases with increasing temperature and was proportional to the average mobility in 23 nm and 12 nm thick samples[88]. In a thinner sample with thickness of 1.6 nm, the maximum MR value was only 68% at 7 T at 280 K, which is two orders of magnitude smaller than those in the thicker samples[88]. H. Li and Y.J. Zeng then attributed the MR mechanism of the FLG to mobility fluctuations  $\Delta m$ .

Both the above situations follow the classical Parish and Littlewood model[88]. Through comparison they unveiled that both changes in the band structure resulting from a different sample thickness and the disorder induced by sample preparation and graphene/substrate interface were responsible for the MR behavior in the thickness variation[88]. The results indicated that MR tuning can be realized by precise thickness control in multilayer graphene[88].

Poh Choon Ooi[38] also fabricated graphene-based non-volatile memory device by solution-processed route. Thermally reduced graphene oxide (rGO) on quartz substrate prepared in the ambient of acetylene/hydrogen plasma treatment was used as bottom conductive electrode to replace the commonly-used bottom conductive indium-tin-oxide layer[38]. The morphology of the rGO film was characterized and used for device fabrication.

The device was fabricated in the simple structure of silver nanowires/nanocomposite/rGO/quartz and the nanocomposite was prepared by mixing the graphene quantum dots and graphene oxide in ethanol[38]. Current-voltage ( $I$ - $V$ ) measurement of the fabricated device showed current bistability with the similar behavior as write-once-read-many-times (WORM) memory device[38]. The direct tunneling, trapped-charge

limited-current, and Ohmic conduction were proposed as dominant conduction mechanisms through the fabricated NVM devices based on the obtained IeV characteristics[38].

Ephraim M. Kiarri and Krishna K. Govender[9] conducted a first principles study of the Titania as used in photo-catalysis to generate charge carries[9]. Models of titania, silica, graphene, epoxy graphene monoxide, single wall Carbon nanotubes and their respective layer were studied in order to investigate their morphological, electronic and optical properties as well as electrostatic potentials[9] shown in Figure 2.12. The calculations were performed using density functional theory to ascertain the properties of the starting bulk molecules and understand the surface properties, a slab surface of 101, and 111 was cut from the bulk  $TiO_2$  and  $SiO_2$ , respectively. A physical study was carried out on the layers generated in relation to their electronic and optical properties[9]. To understand the electron movement during photocatalysis, a projected density of state study was conducted in order to assess the orbital contribution in the charge transfer[9].

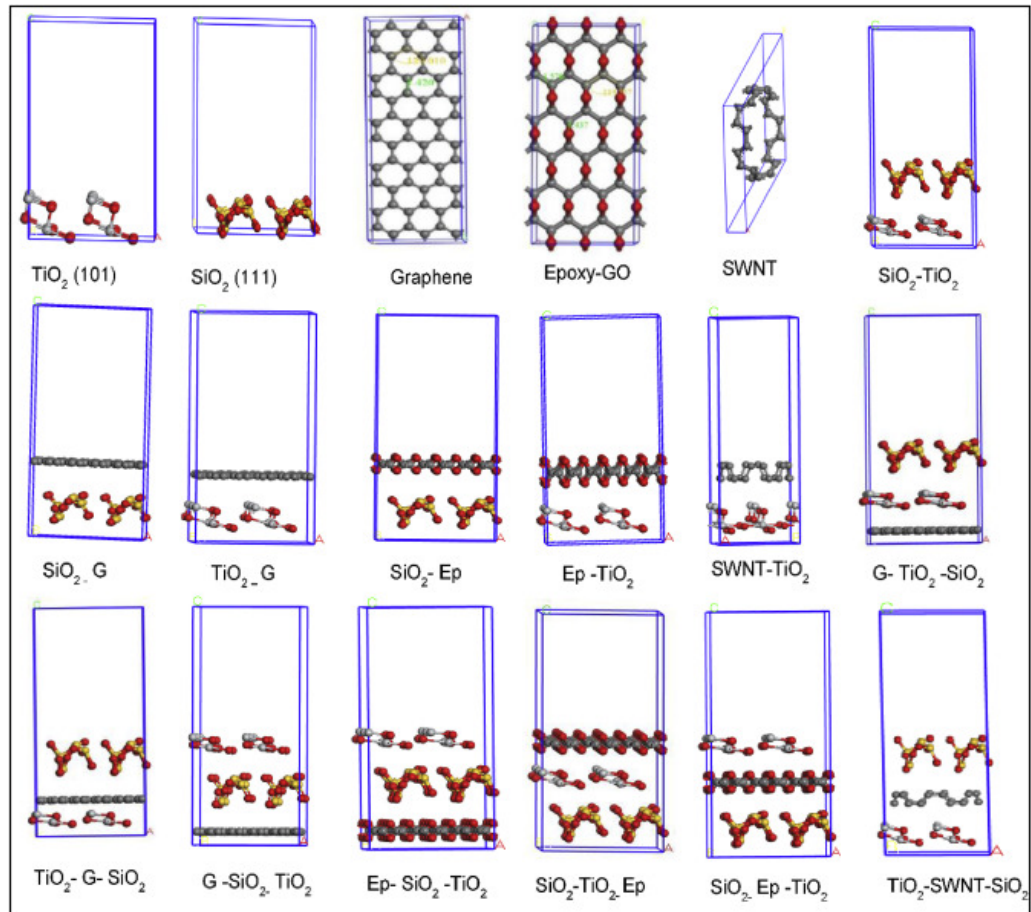


FIGURE 2.12: Structural models of surfaces and layers built to explore electronic and optical properties of generated  $TiO_2$  composites[9]

Kaushal Kumar[89] conducted a study on the matrix modification of relatively low viscous epoxy based polymer treated under ultrasonic mixing (UM) and ultrasonic mixing

with simultaneous stirring by a rotating impeller, referred to as ultrasonic dual mixing (UDM), and the effect of processing techniques has been investigated in terms of the formation of nanocavities in the epoxy matrix[89]. Nanocavities of different sizes have been formed uniformly in the epoxy matrix by UDM[89]. The effect of a change in matrix morphology on the visco elastic, tensile and thermal properties of the cured epoxy resin was studied[89]. The UDM processed cured epoxy matrix showed 18.26% and 88.34% improvement in tensile strength and toughness respectively as compared to unprocessed epoxy[89]. Thermal gravimetric analysis (TGA) of UDM processed epoxy showed significant enhancement in the thermal stability of the epoxy matrix[89].

Mu Ee Foo[90] conducted a study on the biomedical applications of graphene. Nanotechnology is the developing field, bringing the materials in the nanoscale level, has been applied in the interdisciplinary sciences[90]. Different nanomaterials, such as gold, silver, zinc, copper and graphene are shown to have a wide range of applications. Among these, graphene is one of the faster upcoming two-dimensional nanomaterials utilized in various fields due to its positive features including the properties of thermal, electrical, strength and elasticity[90]. Biomedical applications of graphene have been widely attested to be popular among academician and industrial partners for creating next generation medical systems and therapies[90]. Mu Ee Foo selectively revealed the current applications of graphene in the interdisciplinary medical sciences[90].

### **2.5.2 Epoxy**

Epoxy resins were first commercialized in 1946 and are widely used in industry as protective coatings and for structural applications, such as laminates and composites, tooling, moulding, casting, bonding and adhesives, and others [42]. Epoxy can react with different substrates, this therefore gives it adaptability[91]. Treatment with curing agents gives insoluble and intractable thermoset polymers[10]. Some of the characteristics of epoxy resins are high chemical and corrosion resistance, good mechanical and thermal properties, outstanding adhesion to various substrates, low shrinkage upon cure, good electrical insulating properties, and the ability to be processed under a variety of conditions[92]. Depending on the specific needs for certain physical and mechanical properties, combinations of choices of epoxy resin and curing agents can usually be formulated to meet the market demands[93]. However, in terms of structural applications, epoxy resins are usually brittle and notch sensitive[92]. As a result, tremendous effort has been focused on toughness improvement during past three decade[94].

Epoxy resins are compounds containing more than one epoxide group per molecule on average. Commercial epoxy resins contain aliphatic, cycloaliphatic, or aromatic

backbones[95]. They are prepared from either epichlorohydrin or by direct epoxidation of olefins with peracids. The most important intermediate for epoxy resins is the diglycidyl ether of bisphenol A (DGEBA) [10], which is synthesized from bisphenol A and excess epichlorohydrin (Figure 2.13).

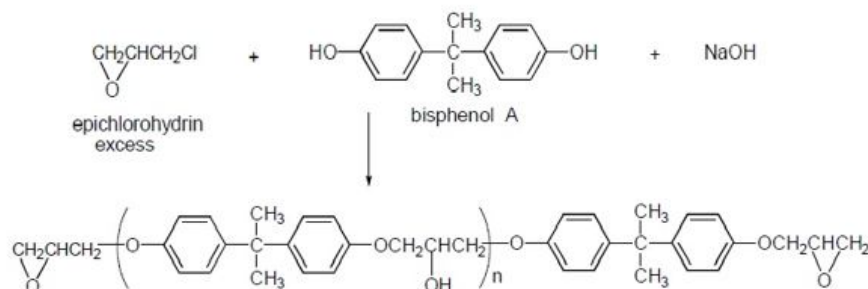


FIGURE 2.13: Diglycidyl ether of bisphenol A, DGEBA[10]

Commercial liquid epoxy prepared by two process. Lower molecular weight solid resins with n values up to 3.7 are prepared directly from epichlorohydrin [10], bisphenol A and a stoichiometric amount of NaOH (taffy process[96]). Higher molecular weight solid resins are prepared by chain extension reaction of liquid epoxy resin (crude DGEBA) with bisphenol A [92] using basic inorganic reagents such as NaOH or  $\text{Na}_2\text{CO}_3$  as catalysts (advancement or fusion process)[97].

Multifunctional epoxy resins such as aromatic glycidyl ether resins and aromatic glycidyl amine resins are commercially available [10]. Commercially important epoxy phenol Novolac resins and epoxy cresol Novolac resins ( are prepared from excess epichlorohydrin and phenol-formaldehyde or o-cresol-formaldehyde resins [98].

The high functionality of the these Novolac resins increases crosslink density and improves thermal stability and chemical resistance[92]. Epoxy resins derived from multifunctional aromatic glycidyl amine resins such as triglycidyl-p-aminophenol and tetreglycidyl-4,4-diaminodiphenylmethane have excellent elevated temperature properties[99].

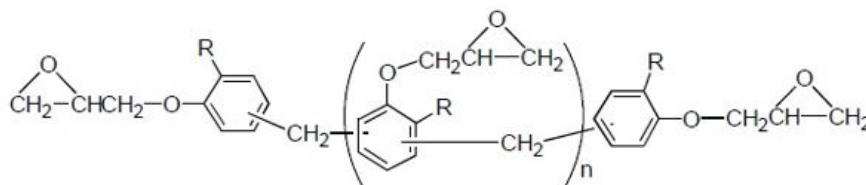


FIGURE 2.14: EPN, R = H, ECN, R =  $\text{CH}_3$  (Y. Takagi and H. Hirayama 2017)

Epoxy resins are prepared using different molar ratios of epichlorohydrin to bisphenol A to afford different molecular weight products[92]. High molecular weight solid epoxy resins

with n values ranging from 2 to 30 are Glycidyl esters prepared from cycloaliphatic carboxylic acid and cycloaliphatic epoxy resins based on the epoxidation of cycloolefins are also commercially available[100].

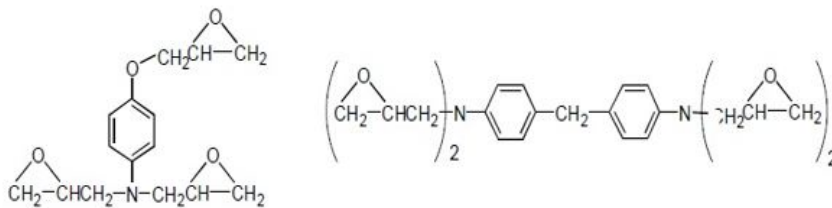


FIGURE 2.15: (triglycidyl-p-aminophenol) 8.3 (triglycidyl-p-aminophenol) and (tetraglycidyl-4,4'-diaminodiphenylmethane) TGDDM, Araldite MY 720 (CIBA-GEIGY) ERL 0510 (CIBA-GEIGY) (Y. Takagi and H. Hirayama 2017)

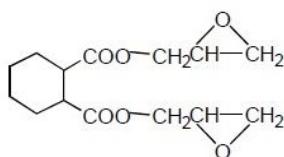


FIGURE 2.16: Diglycidyl ester of hexahydrophthalic acid (Y. Takagi and H. Hirayama 2017)

Treatment of epoxy resins with curing agents or hardeners gives three-dimensional insoluble and infusible networks[92]. Epoxy resins can be cured with a wide variety of curing agents[101]. The choice of curing agents depends on the required physical and chemical properties, processing methods and curing conditions[102]. Epoxy resins can be cured with either catalytic or coreactive curing agents. Catalytic curing agents function as initiators for epoxy ring-opening homo-polymerization[92]. Epoxy resins can be catalytically cured by Lewis bases such as tertiary amines, or Lewis acids such as borontrifluoridemonoethylamine[103]. These catalytic curing agents can be used for homo-polymerization, as accelerators or supplemental curing agents for other curing agents[104].

In 2017, Fariba Safaei[105] conducted a systematic investigation on the properties of microcapsules affected by the synthesis procedure. Scanning Electron Microscopy (SEM), Fourier Transform Infrared Spectroscopy (FTIR) and Thermogravimetric Analysis (TGA) were applied to study morphology, chemical structure, mean size, size distribution and thermal properties of the resulting microcapsules[105]. The morphological study showed the microcapsules prepared by SDBS (0.5 wt.%) are of spherical nature with few adhesions and the average diameter 2.13 nm for encapsulation of epoxy resin[105]. The yield and core content for those microcapsules were determined 50 (wt.%) and 54 (wt.%), respectively.

Investigating the microcapsules chemical structure revealed successful encapsulation of the epoxy resin in PUF shell and the results were confirmed by thermal analysis[105]. Self-healing performance of the coatings containing epoxy-microcapsule was evaluated by salt fog corrosion tested by ASTM B117 and eventually showed excellent corrosion resistance in scratched coatings confirming self-healing properties[105]. Furthermore, electrochemical tests were employed for quantitative investigations of self-healing performance of the coating which confirmed the salt fog corrosion results[105]. Pei YuKuo[105] developed a bio-nanocomposite with an enhanced fibre/resin interface using a hybrid-toughened epoxy[3].

A strong reinforcing effect of NCFs was achieved, demonstrating an increase up to 88% in tensile strength and 298% in tensile modulus as compared to neat petro-based P-epoxy[3]. The toughness of neat P-epoxy was improved by 84% with the addition of 10 wt% bio-based E-epoxy monomers, which also mitigated the amount of usage of bisphenol A (BPA) [105]. The morphological analyses showed that the hybrid epoxy improved the resin penetration and fibre distribution significantly in the resulting composites[105]. Thus, Pei YuKuos findings demonstrated the promise of developing sustainable and high performance epoxy composites combing NCFs with a hybrid petro-based and bio-based epoxy resin system[105].

Peerapan Dittanet[106] also conducted an investigation of the thermo-mechanical behavior of silica nanoparticle reinforcement in two epoxy systems consisting of diglycidyl ether of bisphenol F (DGEBF) and cycloaliphatic epoxy resins[106]. Silica nanoparticles with an average particle size of 20 nm were used. The mechanical and thermal properties, including coefficient of thermal expansion (CTE), modulus (E), thermal stability, fracture toughness ( $K_{IC}$ ), and moisture absorption, were measured and compared against theoretical models[106].

It was revealed that the thermal properties of the epoxy resins improved with silica nanoparticles, indicative of a lower CTE due to the much lower CTE of the fillers, and furthermore, DGEBF achieved even lower CTE than the cycloaliphatic system at the same wt.% filler content[106]. Equally as important, the moduli of the epoxy systems were increased by the addition of the fillers due to the large surface contact created by the silica nanoparticles and the much higher modulus of the filler than the bulk polymer[106]. In general, the measured values of CTE and modulus were in good agreement with the theoretical model predictions[106]. With the Kerner and Halpin-Tsai models, however, a slight deviation was observed at high wt.% of fillers.

The addition of silica nanoparticles resulted in an undesirable reduction of glass transition temperature (Tg) of approximately 20 C for the DGEBF system, however, the

T<sub>g</sub> was found to increase and improve for the cycloaliphatic system with silica nanoparticles by approximately 16°C[106]. Furthermore, the thermal stability improved with addition of silica nanoparticles where the decomposition temperature (T<sub>d</sub>) increased by 10°C for the DGEBF system and the char yield significantly improved at 600°C[106]. The moisture absorption was also reduced for both DGEBF and cycloaliphatic epoxies with filler content. Lastly, the highest fracture toughness was achieved with approximately 20 wt.% and 15 wt.% of silica nanoparticles in DGEBF and cycloaliphatic epoxy resins, respectively[106].

In 2017, Yun Chen and Donghai Zhang[11] conducted an experimental study to improve the electrical insulation of epoxy resin. The effects of boehmite,  $\gamma$ -alumina and alumina nanoparticles on the volume resistivity, dielectric strength and glass transition temperature of epoxy nanocomposites were investigated[11]. The results showed that  $\gamma$ -alumina nanoparticles displayed obvious advantages in enhancing electrical insulation performance of epoxy nanocomposites, compared to boehmite nanoparticles[11] as shown in Figure 2.17. The direct current volume resistivity and breakdown strength of epoxy nanocomposite with 2.0 wt%  $\gamma$ -alumina nanoparticles was improved to 2.2 and 76.1 kV mm<sup>-1</sup> respectively[11]. And these improved values of electrical insulation properties are much higher than these of epoxy nanocomposites reported in previous studies[11]. The main reason of these improvements may be that the epoxy/ $\gamma$ -alumina interaction zone was enhanced by crosslink[11].

Camille Franois[107] conducted a study on biobased diepoxy synthons derived from isoeugenol, eugenol or resorcinol (DGE-isoEu, DGE-Eu and DGER, respectively) have been used as epoxy monomers in replacement of the diglycidyl ether of bisphenol A (DGEBA)[107]. Their curing with six different biobased anhydride hardeners lead to fully biobased epoxy thermosets. These materials exhibited interesting thermal and mechanical properties comparable to those obtained with conventional petrosourced DGEBA-based epoxy resins cured in similar conditions[107]. In particular, a high T<sub>g</sub> in the range of 90°C and instantaneous moduli higher than 4.3 GPa have been recorded[107]. These good performances were very encouraging, making these new fully biobased epoxy thermosets compatible with the usual structural application of epoxy materials[107].

However, it was found that the skid resistance could be a concern when the vehicle speed is higher than a certain level according to the dynamic friction test[108]. The results suggested that to control the traffic speed when epoxy asphalt concrete is applied as steel bridge pavement. In terms of the raveling and stripping, it was found that the epoxy asphalt mixture has an excellent anti-stripping performance based on the Cantabro and Hamburg wheel tracking test results[108]. The yield point was not reached after 20,000

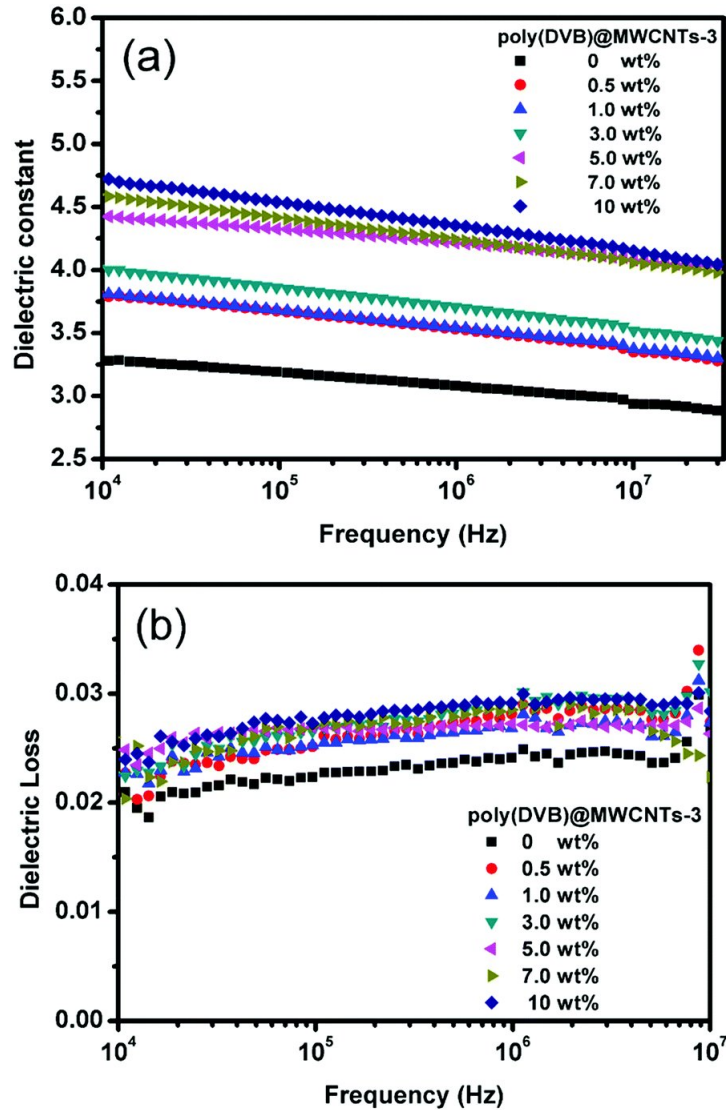


FIGURE 2.17: Dielectric constants (a) and dielectric losses (b and c) of MWCNTs/epoxy resin composites[11].

loading cycles at 60C in the immersed Hamburg wheel tracking test. The mean profile depth of the epoxy asphalt concrete is 0.305 mm, much lower than conventional asphalt concrete indicating a very fine surface texture[108].

Linna Su and Xiaoliang Zeng[109] fabricated kaolinite/epoxy resin nanocomposites using functionalized kaolinite (KGS) as a filler[109]. The KGS was prepared by silylation of 3-aminopropyltriethoxysilane onto the surface of mechanically ground kaolinite[109]. The addition of KGS into epoxy resin matrix improved the storage modulus and glass-transition temperature, compared to those of epoxy resin nanocomposites filled with raw kaolinite[109]. Furthermore, with the increase of KGS loading, the coefficient of thermal expansion decreased gradually, and the dielectric constant slightly increased when compared to that of pure epoxy resin[109]. The presence of kaolinite led to an improvement in the water resistance property of kaolinite/epoxy resin nanocomposites[109].

Linna Su and Xiaoliang Zeng's research provided guidance to construct high-performance kaolinite/epoxy resin nanocomposites[109]. Wei QiXie[110] reported on a new method for the determination of epoxy groups in epoxy resins by reaction-based headspace gas chromatography (HS-GC) [110]. After epoxy resins reacted with hydrochloric acid (HCl) solution, the remaining HCl reacted with bicarbonate solution in a closed headspace vial to form carbon dioxide that was measured by HS-GC[110]. It was found that the first reaction can be finished in 30 min at room temperature and the second reaction, together with headspace equilibration, can be achieved within 15 min at 60°C[110]. The results showed that the method has a good precision and accuracy, in which the relative standard deviation in the repeatability measurement was 4.20%, and the relative differences between the data obtained by the HS-GC method and the reference method were within 8.04%[110]. The present method is simple, efficient, and suitable for use in the epoxy resin related research[110].

## 2.6 Numerical Modelling

Modelling has been a useful tool for engineering design and analysis. The definition of modelling may vary depending on the application, but the basic concept remains the same: the process of solving physical problems by appropriate simplification of reality[92]. In engineering, modelling is divided into two major parts: physical/empirical modelling and theoretical/analytical modelling[111]. Laboratory and in situ model tests are examples of physical modelling, from which engineers and scientists obtain useful information to develop empirical or semi-empirical algorithms for tangible application[112]. This research will be focusing more on theoretical modelling.

### 2.6.1 Numerical modeling steps

Theoretical modelling usually consists of four steps. The first step is construction of a mathematical model for corresponding physical problems with appropriate assumptions[113]. This model may take the form of differential or algebraic equations. In most engineering cases[114], these mathematical models cannot be solved analytically, requiring a numerical solution[115]. The second step is the development of an appropriate numerical model or approximation to the mathematical model[116]. The numerical model usually needs to be carefully calibrated and validated against pre-existing data and analytical results[111].

Error analysis of the numerical model is also required in this step. The third step of theoretical modelling is actual implementation of the numerical model to obtain

solutions[117]. The fourth step is interpretation of the numerical results in graphics, charts, tables, or other convenient forms, to support engineering design and operation[111]. With the increase in computational technology, many numerical models and software programs have been developed for various engineering practices[118].

Fundamental scientific studies and thorough understanding of the physical phenomena provide a reliable and solid guideline for engineering modelling[119]. In this project, the focus is on the multiscale analysis of graphene polymer nanocomposite interfacial region[111]. Molecular dynamics was a tool used to study the interfacial region at nano-scale and finite element analysis for macro-scale analysis [120]. The numerical models developed in this research are based on well-developed theories and constitutive laws in engineering[111], as well as numerical methods widely accepted in engineering. The numerical results are also carefully analyzed against existing experimental data[121].

## 2.7 Molecular dynamics

Molecular dynamics (MD) emerged as one of the first simulation methods from the pioneering applications to the dynamics of liquids by Alder and Wainwright and by Rahman in the late 1950s and early 1960s[122]. Due to the revolutionary advances in computer technology and algorithmic improvements, MD has subsequently become a valuable tool in many areas of physics and chemistry[123]. Since the 1970s, MD has been used widely to study the structure and dynamics of macromolecules, such as proteins or nucleic acids[122].

### 2.7.1 MD Simulation Methods

There are two main families of MD methods[124], which can be distinguished according to the model (and the resulting mathematical formalism) chosen to represent a physical system[125]. In the classical mechanics approach to MD simulations molecules are treated as classical objects, resembling very much the ball and stick model[124]. Atoms correspond to soft balls and elastic sticks correspond to bonds[126]. The laws of classical mechanics define the dynamics of the system. The quantum or first-principles MD simulations, which started in the 1980s with the seminal work of Car and Parinello[122], take explicitly into account the quantum nature of the chemical bond[127]. The electron density function for the valence electrons that determine bonding in the system is computed using quantum equations, whereas the dynamics of ions is followed classically[128].

Shuishi Nose [129] proposed a molecular dynamics simulation method which can generate configurations belonging to the canonical (T, V, N) ensemble or the constant temperature constant pressure (T, P, N) ensemble[129]. He generated a molecular dynamics simulation based on the steps illustrated on the flow chat shown in Figure2.18. The research focused on modeling the silica composite properties using molecular dynamics and results gave matching results to experimental results[129].

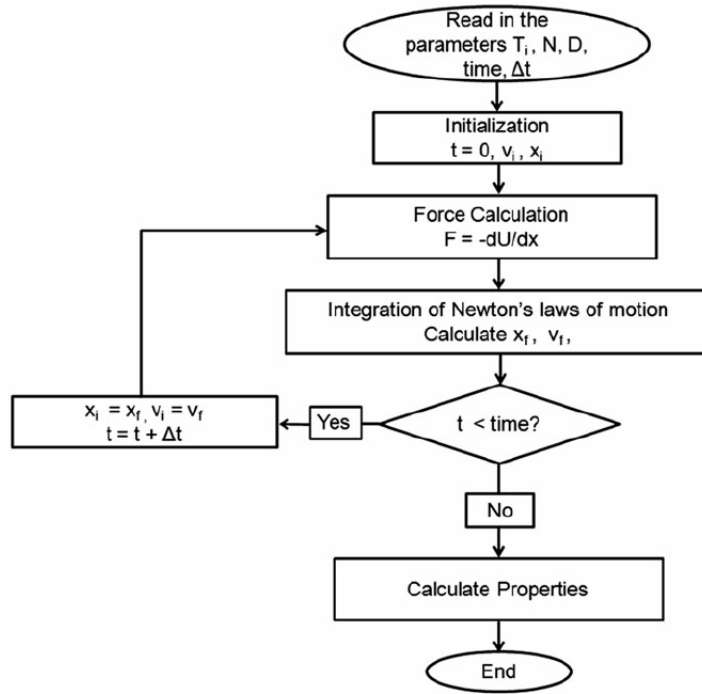


FIGURE 2.18: Flow-chart depicting the general steps of a typical MD simulation[12]

Using a transformation of the rigid body equations of motion Denis J. Evans and Sohail Murad[130] also put in play the algorithm presented in Figure 2.18 for the molecular dynamics simulation of rigid poly-atomic molecules[130]. Using the molecular dynamics initialization and force calculations for the positions of molecules the mechanical properties of the nanocomposite were characterized[130].

Quantum MD simulations represent an important improvement over the classical approach and they are used in providing information on a number of biological problems[131]. However, they require more computational resources. At present only the classical MD is practical for simulations of biomolecular systems comprising many thousands of atoms over time scales of nanoseconds[132].

### 2.7.2 MD Forces

The atomic force field model describes physical systems as collections of atoms kept together by interatomic forces[131]. In particular, chemical bonds result from the specific

shape of the interactions between atoms that form a molecule[133]. The interaction law is specified by the potential  $U(r_1, \dots, r_N)$ , which represents the potential energy of  $N$  interacting atoms as a function of their positions[134]. Given the potential, the force acting upon the  $i$ th atom is determined by the gradient (vector of first derivatives) with respect to atomic displacements, as shown in the equation below[135].

$$F_i = -\frac{\partial U(r_1, \dots, r_N)}{\partial r_i} = -\frac{\partial U}{\partial x_i}, \frac{\partial U}{\partial y_i}, \frac{\partial U}{\partial z_i}$$

The notion of atoms in molecules is only an approximation of the quantum-mechanical picture, in which molecules are composed of interacting electrons and nuclei[136]. Electrons are to a certain extent delocalized and shared by many nuclei and the resulting electronic cloud determines chemical bonding[137]. It turns out, however, that to a very good approximation, known as the adiabatic (or Born-Oppenheimer) approximation and based on the difference in mass between nuclei and electrons, the electronic and nuclear problems can be separated[138].

Mark E. Tuckerman and Bruce J. Berne[130] worked on the simulation of condensed systems and analyzing interaction forces as represented in Figure 2.19. Every atom has a unique position and velocity within the simulation, and all of the atomistic properties associated with that specific atom: atomic name, atomic mass, atomic radius, and the interatomic potential functions[130]. All of the atoms are treated as if they are classical particles that move according to Newton's laws of motion (i.e.  $F=ma$ ; thus, the acceleration ( $a$ ) acting on any atom is determined by the net interatomic force ( $F$ ) acting on the atom divided by the atom's mass ( $m$ )) presented in Figure 2.19.

### 2.7.3 MD Potentials/Energies

The electron cloud equilibrates quickly for each instantaneous configuration of the heavy nuclei[139]. The nuclei, in turn, move in the field of the averaged electron densities[136]. As a consequence, one may introduce a notion of the potential energy surface, which determines the dynamics of the nuclei without taking explicit account of the electrons[140].

With use of a Lagrangian[141] which allows for the variation of the shape and size of the periodically repeating molecular-dynamics cell, it is shown that different pair potentials can lead to different crystal structures[141]. The potential consists of bonded and nonbonded potentials. Within the bonded and nonbonded potentials, the van der

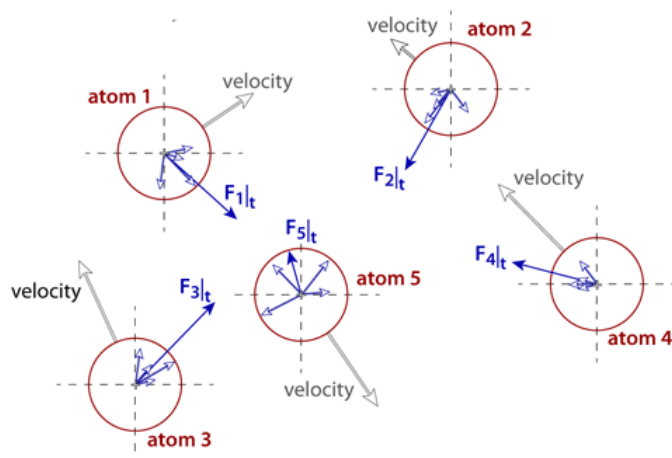


FIGURE 2.19: Atom positions and velocities in a system to calculate forces (M. Parrinello and A. Rahman 2014).

van der Waals interactions, Lennard Jones, angle, bond length are defined to characterize atomic interactions[141].

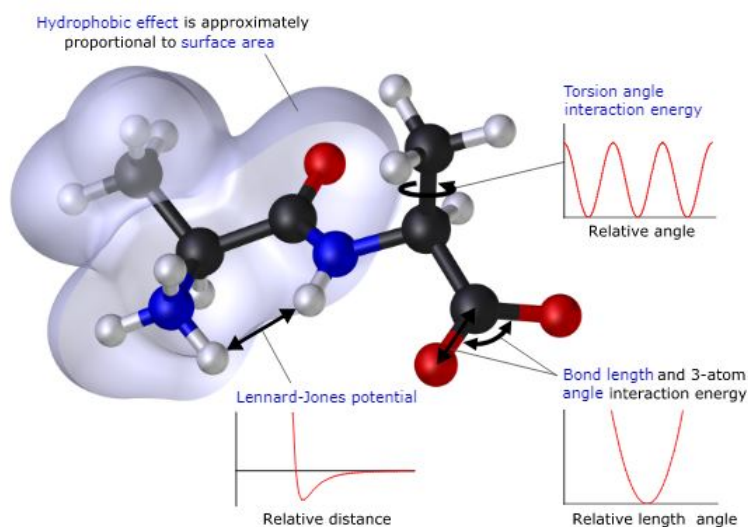


FIGURE 2.20: Atom positions and velocities in a system to calculate forces (M. Parrinello and A. Rahman 2014).

Given the potential energy surface, we may use classical mechanics to follow the dynamics of the nuclei[142]. Identifying the nuclei with the centres of the atoms and the adiabatic potential energy surface with the implicit interaction law[131], we obtain a rigorous justification of the intuitive representation of a molecule in terms of interacting atoms[143]. The separation of the electronic and nuclear variables implies also that, rather than solving the quantum electronic problem (which may be in practice infeasible), we may apply an alternative strategy, in which the effect of the electrons on the nuclei is expressed by an empirical potential[136].

The problem of finding a realistic potential that would adequately mimic the true energy surfaces is nontrivial but it leads to tremendous computational simplifications[144]. Atomic force field models and the classical MD are based on empirical potentials with a specific functional form, representing the physics and chemistry of the systems of interest[145]. The adjustable parameters are chosen such that the empirical potential represents a good fit to the relevant regions of the ab initio Born-Oppenheimer surface[122], or they may be based on experimental data.

#### 2.7.4 MD Atomic Interactions

Molecular dynamics interactions are defined by the summation of all the bonds, angles and torsion angles defined by the covalent structure of the system. This therefore ensures the atom pairs correct chemical structure[136], but prevents modelling chemical changes such as bond breaking[146]. The rotations around the chemical bond, which are characterized by periodic energy terms[131] are also defined in the atom interactions. The Van Der Waals repulsive and attractive (dispersion) interatomic forces in the form of the Lennard Jones 12-6 potential are also introduced which are short distance forces between molecules in a unit cell, and lastly the Coulomb electrostatic potential[147] as shown in Figure 2.21. Some effects due to specific environments can be accounted for by properly adjusted partial charges (and an effective value of the constant  $k$ ) as well as the van der Waals parameters[124].

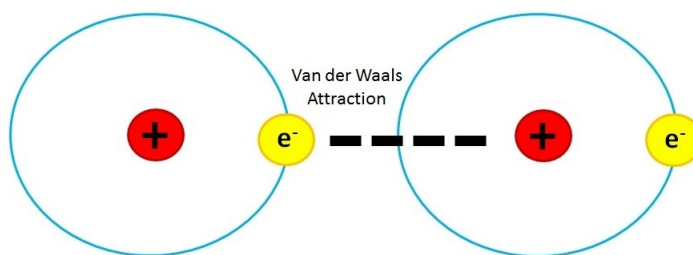


FIGURE 2.21: Atomic interactions due to van der waal attractions (Matthew Dedmom and C. Dobson 2015).

In MD simulations the time evolution of a set of interacting particles is followed via the solution of Newtons equations of motion. Particles usually correspond to atoms, although they may represent any distinct entities (e.g. specific chemical groups)[122] that can be conveniently described in terms of a certain interaction law[148]. To integrate the above second order differential equations the instantaneous forces acting on the particles and their initial positions and velocities need to be specified[136]. Due to the

many-body nature of the problem the equations of motion are discretized and solved numerically. The MD trajectories are defined by both position and velocity vectors and they describe the time evolution of the system in phase space[149].

Accordingly, the positions and velocities are propagated with a finite time interval using numerical integrators, for example the Verlet algorithm. The (changing in time) position of each particle in space is defined by  $r_i(t)$ , whereas the velocities  $v_i(t)$  determine the kinetic energy and temperature in the system[131]. As the particles move their trajectories may be displayed and analysed, providing averaged properties[150]. The dynamic events that may influence the functional properties of the system can be directly traced at the atomic level, making MD especially valuable in molecular biology[122].

In 2016 Matthieu Chavent[151], conducted a molecular dynamics simulation of membrane proteins and their interactions: from nanoscale to mesoscale[151]. Building on the success of proteinlipid interaction simulations, larger scale simulations of their research revealed crowding and clustering of proteins, resulting in slow and anomalous diffusional dynamics, within realistic models of cell membranes[151]. Current methods allow near atomic resolution simulations of small membrane organelles, and of enveloped viruses to be performed, revealing key aspects of their structure and functionally important dynamics[152]. This showed the interaction of organic atoms in the presence of Van Der Waal interactions and potentials[151].

In 2017, Hongshu Zhang[153] performed a molecular dynamics simulation to study segments of SDS bilayers (as part of vesicles) in the bulk solution systematically, at the moment that the lower leaflet of bilayers already detached from solid surfaces[153]. The SDS membrane would rather keep their bilayers structure than return to micelles when the initial interdigitated degree ( $i$ ) between alkyl chains is more than 1.4%[153]. And the interdigitated degree is always approaching to 2.0% while the equilibrium was reached. The aggregates behaved as curved bilayers, planar bilayers, perforated bilayers, and micelles with the increase of the lower leaflet cross-sectional area[153]. Besides, the structures of salt bridge and water bridge structures were formed between DS and Na<sup>+</sup> ions or water molecules, which contributed to the stability of SDS bilayers[153]. The distribution difference of the salt bridges along the direction of S-O axis between the two leaflets leads to the asymmetry of the bilayers, which played supplementary role to the formation of bilayers curvature[153].

## 2.8 Finite Element Analysis

Finite element analysis (FEA) has become commonplace in recent years, and is now the basis of a multibillion dollar per year industry. Numerical solutions to even very complicated stress problems can now be obtained routinely using FEA, and the method is so important that even introductory treatments of Mechanics of Materials such as these should outline its principal features[154].

In 2011, PingZhu and Lei [155] presented bending and free vibration analyses of thin to moderately thick composite plates reinforced by single-walled carbon nanotubes using the finite element method based on the first order shear deformation plate theory[155]. The effects of different boundary conditions were examined. Numerical examples were computed by an in-house finite element code and their results showed good agreement with the solutions obtained by the FE commercial package ANSYS[155].

Gusev [156] described barrier properties of a nanocomposite comprised of perfectly aligned randomly dispersed platelets using finite-element based methodology. The finite element based methodology employed was generic and could readily be used to identify the role of various morphological imperfections typical of nanocomposites[156]. A periodic multi-inclusion computer model that comprised of 25 identical parallel non-overlapping identical platelets of aspect ratio 50 was showed from their research[156].

Young [157] predicted the effective thermal conductivity of the polymeric composites filled with carbon nanotubes (CNTs) using FEA homogeneous technique, which made it possible to localize and homogenize a heterogeneous medium. This homogenization technique yielded the effective thermal conductivity in accordance with experimental results[157]. In the case that a heterogeneous material had anisotropic properties or geometrical complexity, the homogenization technique was an efficient method to obtain averaged material properties equivalent to those of the real heterogeneous medium[157].

The organic layers in the composite play a significant role in the mechanical response of nacre to stresses. Katti [158] used three dimensional finite element models of nacre to study influence of nonlinear response of organic components. The resulting yield stress of nacre was compared to experimentally obtained value[158]. This indicated that a much higher yield stress of organic is necessary to obtain the experimentally obtained yield stress of nacre[158].

In 2015, Haibo Yang[159] conducted a study on the effect of nanofiller shape on the visco elasticity of rubber nanocomposites investigated by FEA[159]. Based on the micromechanical theory, the effect of the shapes of nanofillers on the visco elasticity of rubber nanocomposites was evaluated by the finite element analysis. The shapes of nanofillers

discussed included spheres, cylinders, tube, plate, ring, and spring[159]. Two types of interphase bonding interphase and frictional interphase which represented the strong interphase and the weak interphase respectively were assumed to discuss the effect of interphase on the viscoelasticity of rubber nanocomposites[159].

The dissipation and loss factors were calculated and discussed[159]. The predicted results showed that the shapes of nanofillers have great effect on the visco elasticity of the rubber nanocomposite[159]. Including spring nanofillers in the rubber matrix can greatly decrease the loss factor of the nanocomposite when the interphase is a bonding interphase, including the ring nanofillers in the rubber matrix can greatly increase the loss factor of the nanocomposite when the interphase is a frictional interphase[159].

Dimitrios Tzetzis[160] conducted research on a continuous Finite Element Analysis (FEA) simulation method of the ball indentation hardness test is introduced in order to describe the deformation behavior of nanosilica composites and with this to extract precisely the material's stress-strain behavior[160]. The developed procedure demonstrated in particular the adequacy of this method to determine the nanocomposites' elastic modulus which was compared with the Halpin-Tsai and Lewis-Nielsen[160] models as well as with experimental measurements taken from uniaxial tensile tests[160]. The fracture area of all the tensile specimens was examined using a scanning electron microscope (SEM)[160]. It was shown that the correlation between the experimental results, the semi-empirical models and the FEA computational models concerning the elastic modulus values was satisfactory with very small deviations[160].

Finite element codes are less complicated than many of the word processing and spreadsheet packages found on modern microcomputers. Nevertheless, they are complex enough that most users do not find it effective to program their own code[161].

### **2.8.1 Multiscale Modelling**

A trend which has gained momentum during the last decade is a loose integration of computational methods under the banner of multiscale modelling. The core idea of multiscale modelling is not in the effusive complication of materials related modelling tasks, but the realization that present day material modelling means can be effectively used in solving materials related engineering problems and systematically aim towards optimal material solutions on a component specific case by case basis[162]. These abilities were previously unobtainable due to affiliated limitations in available computational methodologies and resources, but have reached a degree of maturity during the last five to ten years. Thus, the argument is that incorporation of material modelling systematically in material development, tailoring and selection processes enables the development of

materials with improved performance, better utilization and leads to more cost effective solutions[163].

Carrying out modelling in a productive manner requires tight integration of experimental and modelling activities, experimental activities being for example material characterization and testing in the context of the desired function. Modelling is a synonym for understanding and quantifying what actually takes place when the material performs the critical functions it is supposed to, such an activity cannot be effectively carried out solely from a modelling standpoint[163], when the methods being applied to a particular case have not matured to a status with predictive abilities. As such, in an optimal scenario material processing, characterization, testing and modelling activities form a tightly knit cross-linked bundle. In a material design task, one such way of operation is the process-structure properties- performance (PSPP) methodology[164].

The purpose in utilization of such concepts is to provide tools which integrate the various necessary means and methods into a workable whole, enabling and defining the required interactions between the various manufacturing, experimental and modelling activities[164].

Spanos and Konotsos[165] introduced a multiscale Monte Carlo finite element method (MCFEM) for determining mechanical properties of polymer nanocomposites (PNC) that consist of polymers reinforced with single-walled carbon nanotubes (SWCNT) [165]. Their method used a multiscale homogenization approach to link the structural variability at the nano-/micro scales with the local constitutive behaviour[165]. Subsequently, the method incorporated a FE scheme to determine the Youngs modulus and Poisson Ratio of PNC[165]. The use of the computed properties in macroscale modelling was validated by comparison with experimental tensile test data.

In 2011 Montazeri[166] employed a combination of molecular dynamics, molecular structural mechanics, and finite element method to compute the elastic constants of a polymeric nanocomposite embedded with graphene sheets, and carbon nanotubes[166]. The reinforcement role of these nanofillers was investigated in transverse directions. Moreover, the dependence of the nanocomposites axial Young modulus on the presence of ripples on the surface of the embedded graphene sheets, due to thermal fluctuations, was examined via MD simulations[166].

Chandra[167] introduced a multiscale modelling approach to simulate the nonlinear tensile behaviour of nanocomposites with single layer graphene (SLG) reinforcement. The graphene nano inclusions were represented at the nanoscale through an atomistic finite element model and the matrix material was approximated by continuum 3D elements.

The multiscale model presented in this work was able to predict features such as debonding, nonlinearity in polymer and strain based damage criteria for the matrix[167]. Stiffness and strength values computed with this model compared well with experimental results available in open literature[167].

Cho and Lau[168] studied the mechanical properties of nanocomposites consisting of epoxy matrix reinforced with randomly oriented graphite platelets by the MoriTanaka approach in conjunction with molecular mechanics as multiscale modelling method[168]. Their calculations confirmed that the modulus of the nanocomposites studied here was strongly dependent on the aspect ratio of the reinforcing particles, but not on their size[168]. The predicted moduli compared favourably with experimental results of several nanocomposites with graphite particles of various aspect ratios and sizes[168].

The different types of multiscale modelling techniques are adaptive, quantum mechanics-molecular mechanics (QM-MM) and heterogeneous multiscale modelling method[28] have been developed to address the problems involving different length and time scales. Adaptive mesh refinement multiscale method is applied in the analysis of crack propagation at different scales of length and time [169]. It can model dynamic and turbulent regions without affecting the precision of the solution but it is limited to pre-determined measured grids as in the cartesian plane which creates the computational grid [28]. QM-MM combines the strengths of the QM (accuracy) and MM (speed) approaches[170]. In this multiscale modelling method, simulation regions are also limited. Moving the limitation borders can affect the results and the time of computing the results [28].

MD simulations (nano-scale) in QM-MM multiscale method may be accurate, but passing the MD boundary conditions to macroscale analysis results in inaccuracies due to the change in computational domain size [169]. These limitations in computational domain size and proper boundary conditions transfer from macro to nanoscale models has shown not to be an issue in heterogeneous multiscale method. Heterogeneous multiscale modelling follows a top down strategy[28]. The basic starting point is an incomplete macroscale model with the micro or nano scale used as a supplement to supply the missing data including boundary conditions from the interfacial region analysis at nanoscale.

# Chapter 3

## Methodology

### 3.1 General Methodology layout

The main focus of the current research is to characterize the interfacial region of graphene-epoxy nanocomposites for improving the overall mechanical properties. In order to characterize the interfacial region properties, the constituents of the nanocomposite were modeled using a multiscale method. At first a unit cell was extracted from the FEA macroscopic model, which consists of an epoxy matrix, a graphene nano-reinforcement and the interfacial region as shown in Figure 3.1. These individual constituents were modelled and analyzed using Molecular dynamics (MD) simulation for obtaining the interfacial region properties which were then linked with FEA macro model to obtain the nanocomposite macro properties.

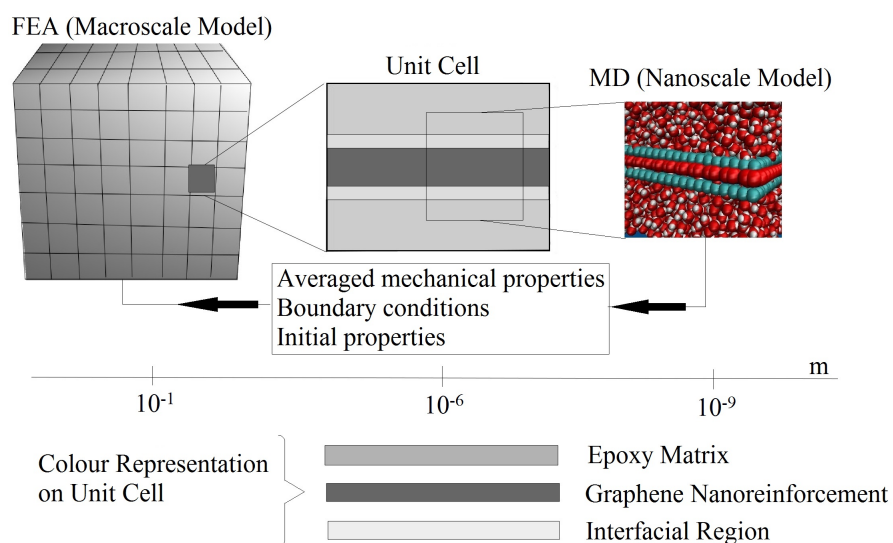


FIGURE 3.1: General steps of the computational details

## 3.2 Molecular Dynamics Modeling and Finite Element Analysis Procedure

### 3.2.1 MD Interaction Forces and Potentials

The MD technique is based on Newton's equations of motion which are used to describe the molecular interactions of particles within a MD model. These interactions between molecules are grouped into bonded and non-bonded interactions. For a successful modeling of interactions, the required parameters are position ( $r$ ) of individual atoms, momentum of each atom within the system, charge ( $q$ ) of each atom and bond information. Based on the above parameters, the interaction force on each particle is represented by,

$$F_i = m_i a_i \quad (3.1)$$

Where  $m_i$  is the mass of each atom and  $a_i$  is the acceleration. For the total number ( $N$ ) of atoms in the unit cell, the interaction force acting on the  $i_{th}$  atom at a given time can also be determined using the interatomic potential  $V_i(r_1, r_2, r_3, \dots, r_N)$  as given below,

$$F_i = -V_i(r_1, r_2, r_3, \dots, r_N) \quad (3.2)$$

In addition, the interaction forces could also be obtained by the spatial derivative of the potential energy function which is again defined by the interatomic potential. Since the atoms within the unit cell have both bonded and non-bonded interactions, hence the total potential energy ( $E(r^N)$ ) is therefore represented by,

$$E(r^N) = E_{bonded} + E_{non-bonded} \quad (3.3)$$

The bonded interactions are due to the covalent bonds between nanoreinforcement and matrix atoms within a unit cell. There are three types of interactions between bonded atoms, which are bonds stretching, bending between the bonds and rotating around the bonds as shown in Figure 3.2.

The bonded interactions are calculated using the Optimized Potentials Liquid Simulation (OPLS) which is the sum of all the bonded interaction energies ( $E_{bonded}$ ) as defined below,

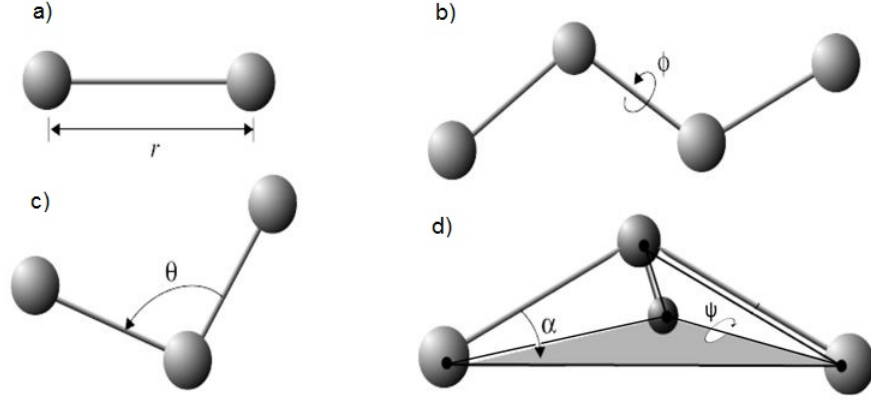


FIGURE 3.2: (a) Bond stretching, (b) Bond rotating (c) Bond bending (d) Mixed (improper)[13]

$$E_{bonded} = E_{bondstretching} + E_{anglebending} + E_{dihedrals} \quad (3.4)$$

The bond stretching energy, ( $E_{bondstretching}$ ) represents the bond stretching interactions and is expressed as

$$E_{bondstretching} = \sum_{bonds} k_r (r - r_0)^2 \quad (3.5)$$

Where  $k_r$  is the bond constant which is predefined in MD simulations and  $r$  the bond length.

The angle bending energy is expressed as:

$$E_{anglebending} = \sum_{angles} k_\theta (\theta - \theta_0)^2 \quad (3.6)$$

Where,  $k_\theta$  is the angle energy constant,  $\theta$  is the actual bond angle and  $\theta_0$  the reference bond angle.

The dihedral energy is expressed as

$$E_{dihedrals} = \sum_{dihedral} \left( \frac{W_1}{2} [1 + \cos(\phi - \phi_1)] + \frac{W_2}{2} [1 + \cos(2\phi - \phi_2)] \right. \\ \left. + \frac{W_3}{2} [1 + \cos(3\phi - \phi_3)] + \frac{W_4}{2} [1 + \cos(4\phi - \phi_4)] \right) \quad (3.7)$$

$W$  is OPLS dihedral constants and  $\phi$  defines an equilibrium angle.

The non-bonded interactions consist of two potential functions, such as Van Der Waals potentials for close interactions (short distances potentials) and electrostatic potentials for the atoms within one electric field (long range interactions) and defined by the equation bellow,

$$E_{non-bonded} = E_{van-der-waals} + E_{electrostatic} \quad (3.8)$$

The electrostatic long range interactions go beyond the interaction range, hence only the van der waals interactions are considered for MD simulations. One of the most widely used functions for the van der Waal interactions is the Lennard-Jones potential ( $U(r)$ ) and defined by,

$$U(r) = 4\epsilon \left[ \left( \frac{\sigma_{ij}}{r} \right)^{12} - \left( \frac{\sigma_{ij}}{r} \right)^6 \right] = \frac{A_{ij}}{r_{ij}^{12}} - \frac{B_{ij}}{r_{ij}^6}$$

$\epsilon$  is the measurement of the Van der Waals attraction between the united atoms

$\sigma$  is the measurement of distance between two nonbonded united atoms

$r$  is the distance of separation between united atoms.

$$A_{ij} = 4\epsilon_{ij}\sigma_{ij}^{12}$$

$$B_{ij} = 4\epsilon_{ij}\sigma_{ij}^6$$

$$\epsilon_{ij} = \sqrt{\epsilon_i\epsilon_j}$$

$$\sigma_{ij} = \frac{1}{2}(\sigma_i + \sigma_j)$$

$\frac{\sigma_{ij}}{r}$  Represents the repulsive properties of the united atoms (steep side of the curve).

$\frac{\sigma_{ij}}{r}$  Represents the attraction properties of the united atoms (smooth side of the curve).

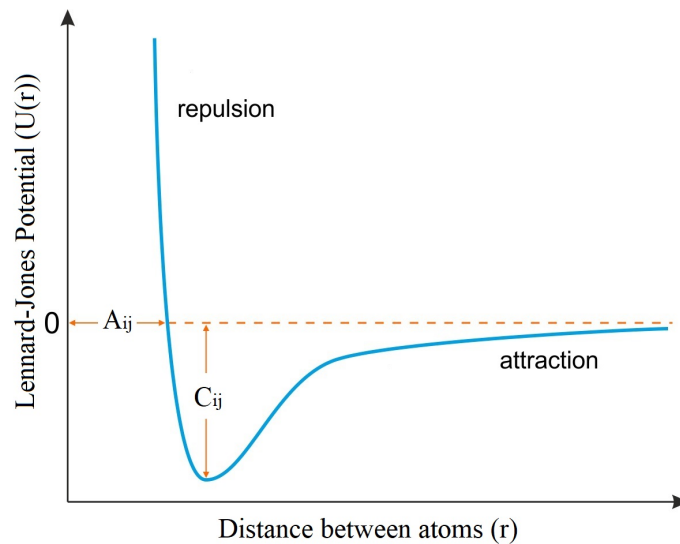


FIGURE 3.3: Lennard Jones potentials for MD simulations[14]

The constants  $A_{ij}$  and  $C_{ij}$  depend on the atom types and are derived from the model being simulated.  $r_{ij}$  represents the distance between the atoms. The term  $r_{ij}^{1/2}$  is for the short range attraction and the term  $r_{ij}^6$  is for the long-range attraction of atoms. This phenomenon is shown in Figure 3.3.

These potentials are used to define the motion and interaction of atoms for both bonded and non-bonded interaction within a composite unit cell.

### 3.2.2 MD Boundary Conditions and Force Calculations

Since the motions and interactions of atoms can alter the size and the force calculations within a unit cell, boundary constraints are essential for maintaining the size of the unit cell and controlling the atomic interactions. Therefore the boundary conditions are set within a unit cell. The periodic boundary conditions are used in MD simulations which state that an atom moves out of a unit cell, will appear on the adjacent unit cell as shown in Figure 3.4.

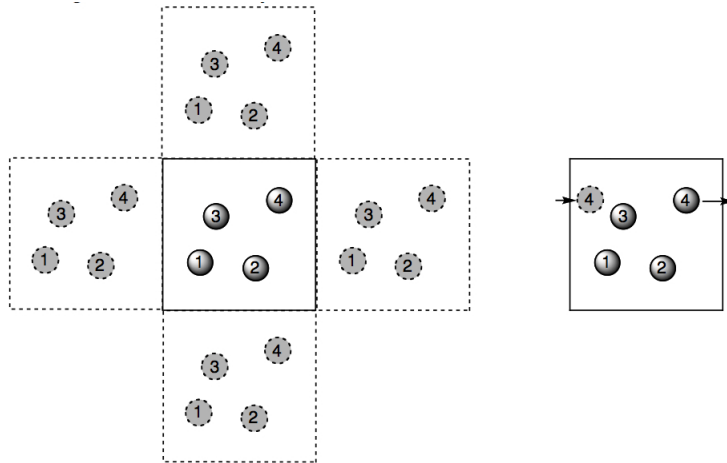


FIGURE 3.4: Two-dimensional schematic of periodic boundary conditions. The particle trajectories in the central simulation box are copied in every direction

Ideally, every atom interacts with every other neighboring atoms located within a certain distance and is known as a cutoff distance. In order to define the cutoff distance, the coordinates of the individual atoms and their movement path (trajectories) within a unit cell are required. Since the interatomic potential ( $F_i = -V_i(r_1, r_2, r_3, \dots, r_N)$ ) is used to define the force acting on atoms, LAMMPS integrates the interatomic potential using a numerical method called, verlet integration for obtaining the required coordinates and trajectories [104]. Using the ensemble of the position vector  $x(t) = (x_1(t), \dots, x_N(t))$ , the interatomic potential can be used to define the force as represented in equation 3.9,

$$F_i(t) = -\nabla V(x(t)) = m \frac{d^2 x(t)}{dt^2} \quad (3.9)$$

where,

$t$  is the time

$F_i$  is the ensemble of forces on the atoms

$\frac{d^2 x(t)}{dt^2}$  is the acceleration (a)

and velocity  $v$  within the acceleration is  $\frac{dx(t)}{dt}$ .

The verlet algorithm is formulated by differentiating the interatomic potential (Equation 3.9) to the fourth order with respect to time and summed up using the Taylor series as given below,

$$x(t + \delta t) = x(t) + \frac{dx(t)}{dt} \delta t + \frac{d^2 x(t)}{dt^2} \frac{\delta t^2}{2} + \frac{d^3 x(t)}{dt^3} \frac{\delta t^3}{6} + \vartheta(\delta t^4) \quad (3.10)$$

The time step  $t$  represents the time taken for an atom to move from  $(x_i)$  to  $(x_{i+1})$  and could be calculated using the optimized potential for liquid simulations (OPLS) united-atom force field. In addition, as the atom moves from one place to another, the velocity of an atom needs to be controlled for stabilizing the verlet algorithm. Since the change in velocity within the algorithm depends on the change in temperature of the system, hence the Verlet integration is performed within the constant number of atoms (N), volume (V) and temperature (T) ensemble. However, for the stabilization of velocity or acceleration of atoms, the maximum temperature should reach to a value of approximately 300 or 400 K. In order to achieve the required temperature, a Nose-Hoover thermostat (NHT) algorithm is introduced. Within this algorithm, a friction dynamic variable ( $\xi$ ) is added, which slows down or accelerates atoms until the maximum temperature is reached. This algorithm is therefore shown in the equation below,

$$\xi(t + \delta t) = \xi\left(t + \frac{dx(t)}{2}\right) + \frac{dx(t)}{Q} \left[ \sum_{i=1}^N m_i \frac{v_i\left(t + \frac{dx(t)}{2}\right)^2}{2} - \frac{3N+1}{2} k_B T \right] \quad (3.11)$$

where,

$Q$  is an effective mass of the system associated to  $\xi$

$T$  denotes the target temperature,

$\frac{3N+1}{2} k_B$  represents the kinetic energy of the united atoms within the unit cell.

The verlet algorithm (Eq.3.10) gives the trajectories and coordinates of the atoms within the MD simulation while NHT (Eq.3.11) algorithm maintains the accuracy of the simulation results.

### 3.2.3 FEA Displacement properties

The macroscale model was defined using a finite element method. Here the displacement (U) for an isotropic material is defined in terms of the Cartesian x, y and z coordinates.

$$U = \begin{bmatrix} u \\ v \\ w \end{bmatrix} \Rightarrow \begin{bmatrix} \epsilon_{xx}, \\ \epsilon_{yy}, \\ \epsilon_{zz} \end{bmatrix} = \begin{bmatrix} \frac{\partial u}{\partial x} \\ \frac{\partial v}{\partial y} \\ \frac{\partial w}{\partial z} \end{bmatrix} \quad (3.12)$$

The strain  $\epsilon$  is defined as

$$\epsilon = \begin{bmatrix} \epsilon_{xx} \\ \epsilon_{yy} \\ \epsilon_{zz} \\ \epsilon_{xy} \\ \epsilon_{yz} \\ \epsilon_{xz} \end{bmatrix} = DU = \begin{bmatrix} \frac{\partial}{\partial x} & 0 & 0 \\ 0 & \frac{\partial}{\partial y} & 0 \\ 0 & 0 & \frac{\partial}{\partial z} \\ \frac{\partial}{\partial y} & \frac{\partial}{\partial x} & 0 \\ 0 & \frac{\partial}{\partial y} & \frac{\partial}{\partial z} \\ \frac{\partial}{\partial z} & 0 & \frac{\partial}{\partial x} \end{bmatrix} U \quad (3.13)$$

Where D is the matrix differentiation operator.

The Hooke's law is used to define the over all response of the macroscale model,

$$\sigma_{ij} = c_{ijkl}\epsilon_{kl} \quad (3.14)$$

where i, j, k, l = 1,2,3 and three dimensional equations for the macroscale mode are given as,

$$\sigma_{xx} = \frac{E}{(1+v)(1-2v)} [(1-v)\epsilon_{xx} + v(\epsilon_{yy} + \epsilon_{zz})] \quad (3.15)$$

$$\sigma_{yy} = \frac{E}{(1+v)(1-2v)} [(1-v)\epsilon_{yy} + v(\epsilon_{xx} + \epsilon_{zz})] \quad (3.16)$$

$$\sigma_{zz} = \frac{E}{(1+v)(1-2v)} [(1-v)\epsilon_{zz} + v(\epsilon_{xx} + \epsilon_{yy})] \quad (3.17)$$

The material constant  $c_{ijkl}$  under plane strain condition is given by,

$$c_{ijkl} = \frac{E}{1-\nu^2} \begin{bmatrix} 1 & \nu & 0 \\ \nu & 1 & 0 \\ 0 & 0 & \frac{1-\nu}{2} \end{bmatrix} \quad (3.18)$$

For the simplification of plane stress, where the stresses in the z direction are considered to be negligible,  $\sigma_{zz} = \sigma_{yz} = \sigma_{xz} = 0$ , the stress-strain compliance relationship for the nanocomposite can also be obtained by replacing E and  $\nu$  in Equation 3.18 with  $\frac{E}{1-\nu^2}$  and  $\frac{\nu}{1-\nu}$  therefore giving the plain stress as:

$$c_{ijkl} = \frac{E(1-\nu)}{(1+\nu)(1-2\nu)} \begin{bmatrix} 1 & \frac{\nu}{1-\nu} & 0 \\ \frac{\nu}{1-\nu} & 1 & 0 \\ 0 & 0 & \frac{1-2\nu}{2(1-\nu)} \end{bmatrix} \quad (3.19)$$

From FEA, the displacements of the nanocomposite macroscale model were obtained.

### 3.2.4 Coupling MD with FEA

The first step in coupling MD with FEA was to create a seamless connection between nano and macroscale. A schematic of the coupling process is shown Figure 3.5. In order to achieve this, the MD nanocomposite parameters (atom coordinates and trajectories) were averaged using Irving Kirkwood method (LAMMPS plugin) and transferred to the macroscale model (FEA model) nodes and elements.

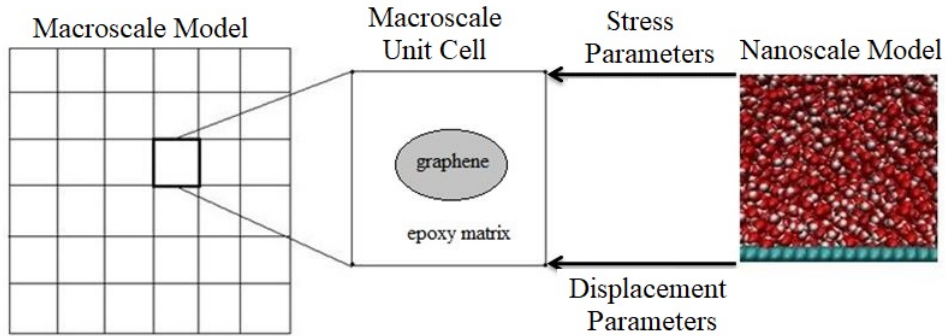


FIGURE 3.5: Coupling of molecular dynamics with finite element analysis

To initiate coupling of these two scales, the macroscale unit cell was modelled based on the parameters acquired from the nanoscale model unit cell. These parameters used to calculate the displacement and momentum using the verlet integration,

$$x(t + \delta t) = x(t) + \frac{dx(t)}{dt}\delta t + \frac{d^2x(t)}{dt^2} \frac{\delta t^2}{2} + \frac{d^3x(t)}{dt^3} \frac{\delta t^3}{6} + \vartheta(\delta t^4) \quad (3.20)$$

This therefore gave coordinates for the initial atom  $x_i$  to the next one  $x_i + 1$  coordinates after time step (t) formulating the macroscale unit cell. The next step was to assign boundary conditions to the macroscale unit cell nodes and elements based on the nanoscale model properties.

This boundary conditions were used to complete the macroscale model by defining the degrees of freedom (using momentum and force). To define the degrees of freedom, LAMMPS extracted parameters (mass and velocity) in addition to the coordinates from the verlet integration scheme to calculate momentum from the nanoscale Newtons equations of motion by the equation below,

$$\frac{d}{dt} \sum_{i=1}^N q_i(x, t) = \sum_{i=1}^N m_i \frac{dv}{dt} \quad (3.21)$$

Where,

$x_i$  represents a set of molecules defined in terms of their time dependent coordinates and  $q_i$  the momentum. Using  $q_i = m_i \frac{dx_i}{dt}$ , the time evolution of momentum from nanoscale to macroscale was written as,

$$\frac{d}{dt} \sum_{i=1}^N q_i(t) v_i(x_i(t), x) = \sum_{i=1}^N \left[ q_i \frac{dx_i}{dr} \frac{dv_i}{dr_i} + \frac{dq_i}{dt} v_i \right] \quad (3.22)$$

This resulted in the attainment of the momentum equation assigned to the nodes in macroscale model and therefore giving a rotational degree of freedom to the nodes and elements represented by,

$$q_i(x_i, t) = \sum_i m_i v_i(x - x_i(t)) \quad (3.23)$$

Where,

$(x - x_i(t))$  represents the displacement of the united atoms with respect to time.

The next boundary conditions to be assigned to the nodes and elements extracted from the nanoscale model was the deflection and stresses (defined by force) of the nodes. These deflections and stresses were defined within the displacement matrix where force (normal or shear) was equivalent to a translation degree of freedom in the macroscale unit cell. The properties of the nodal displacements matrix and of element nodal forces were therefore derived from the Irving Kirkwood stress formula within the LAMMPS plugin represented by,

$$\sigma(\xi, t; x) = - \sum_i (m_i v_i \otimes v) \delta(r_i - \xi) - \frac{1}{2} \sum_{j \neq i} ((r_i - r_j) \otimes f_{ij}) \int_0^1 \delta(\lambda r_i + (1 - \lambda)r_j - \xi) d\lambda \quad (3.24)$$

Where,

$f_{ij}$  represents the force acting on the i-th atom by the j-th atom defining the translation DOF in the macroscale unit cell.

$\sigma$  represents the stress ( $\sigma_{ij} = c_{ijkl} \epsilon_{kl}$ ).

This aligned the properties assigned to the elements and nodes in the macroscale model with the nanoscale model properties therefore completing the coupling of the molecular dynamics model with the macroscale model for the nanocomposite.

### 3.3 Molecular Dynamics modeling of Graphene-Epoxy Nanocomposite

The MD analysis procedure explained in the previous paragraphs was used to model the constituents of the graphene-epoxy nanocomposites. First the matrix was modelled, followed by the nano-reinforcement and finally the interfacial region to study the mechanical properties of this nanocomposite.

#### 3.3.1 Matrix modeling

For the current study, the epoxy (diglycidyl ether of bisphenol A (DGEBA)) was selected as base resin and a diethylenetriamine (DETA) as hardener. The basic atomic structures of the resin and the hardener is shown in Figure 3.6

The epoxy and the hardener chemical reaction was modeled as a non-bonded interactions. Hence the Lennard Jones (LJ) potential was used to define the non-bonded interactions. The resin and hardener atoms were grouped as one united atom and were modeled using optimized potential for liquid simulations (OPLS) force field.

The LJ potential within the nonbonded energy introduces the Van Der Waal interactions between the individual atoms ( $CH_3$ ,  $CH_2$ , CH,  $NH_2$ , NH and alkyl groups) of both resin and the hardener. This combinations were modeled as one united atom corresponding to

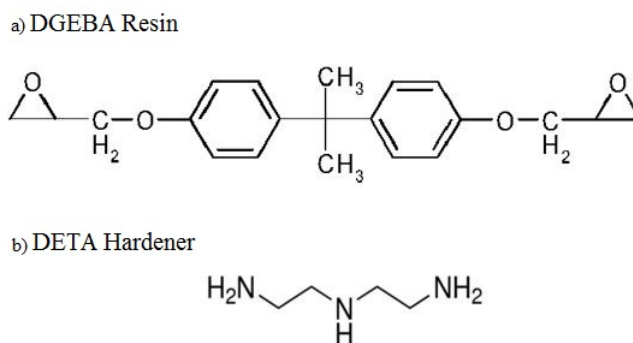


FIGURE 3.6: a) DGEBA resin molecular structure and b) Molecular structure of DETA hardener.

the masses of the individual constituents. This simplifications reduces the computation time of the LAMMPS code (provided in Appendix A).

The first step in this simulation was to model a epoxy unit cell with a stoichiometric ratio of 2 molecules of resin and one molecule of hardener (2:1). This unit cell contains the total of 117 atoms. Their initial coordinates and details for bonds, angles and dihedrals were written in LAMMPS and periodic boundary conditions were applied in all directions. The use of united atoms concept reduce the total atoms of unit cell from 117 individual atoms to 83 united atoms. Furthermore, due to the difference in mass of each atoms within the resin and hardener system, the LAMMPS code reduces the 83 united atoms to 52 united atoms. This represents the 2:1 ratio of resin and hardener epoxy system to an approximate number of 31 resin and 21 hardener united atoms. Therefore a epoxy unit cell contains a total of 52 united atoms. This initial setup is summarized in Table 3.1.

TABLE 3.1: MD initial setup for epoxy matrix modeling.

MD model setup	DGEBA and DETDA hardener (epoxy)
Stoichiometric ratio	2 : 1
Unit cell size	10 x 10 x 10
Boundary conditions	Periodic
Force Field	OPLS (Optimized Potentials for Liquid Simulations)
Cutoff radius	10Å
Total number of atoms	EPON 862 = 31 DETDA = 21

Within one united atom, the cross-linking of resin and harder occurs at the controlled constant temperature which was then equilibrated by Nose Hoover thermostat (NVT) method. This equilibration was run (NVT) at 600 K and low density of  $0.6 \text{ g/cm}^3$ . However, for maintaining the required weight fraction, the simulation box will be reduced

using the NVT method for 100 ps at 450 K and constant density of  $0.9 \text{ g/cm}^3$ . In addition, the maximum atom movements were limited to  $0.2 \text{ \AA}$  in order to smooth the energy changes during simulation. The cross linking reaction of hardener and resin density was recorded with time and shown in Figure 3.7. It shows that the cross linking quickly increases at early stages of the simulation and then slows down while the network grows continuously. This shows that the perfect cross linking of resin to hardener was achieved.

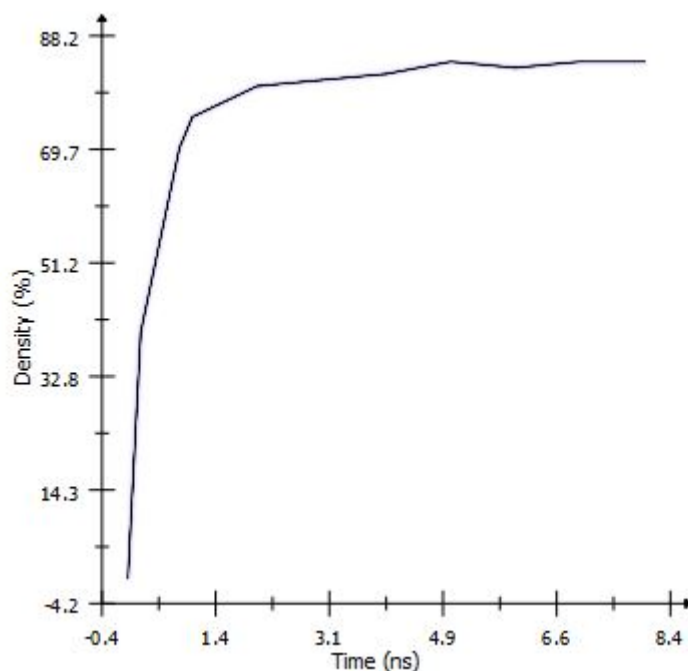


FIGURE 3.7: Change in cross-linking density with time.

The resultant MD model of epoxy matrix is shown in Figure 3.8. The cross linked network had the density of  $1.12 \text{ g/cm}^3$  at low pressure around 1 atm. The obtained density was in close agreement with [98] of  $1.13 \text{ g/cm}^3$  for DGEBA-hardener with DETA epoxy. This epoxy model was then reinforced with functionalized graphene nanoreinforcement.

### 3.3.2 Nanoreinforcement modeling

Graphene was modeled using LAMMPS code. The bonded interactions between carbon-carbon atoms were modeled using original Tersoff and optimized Tersoff potentials. The nonbonded van der Waals interactions between individual carbon atoms at different atomic planes were modeled by Lennard-Jones (LJ) potentials.

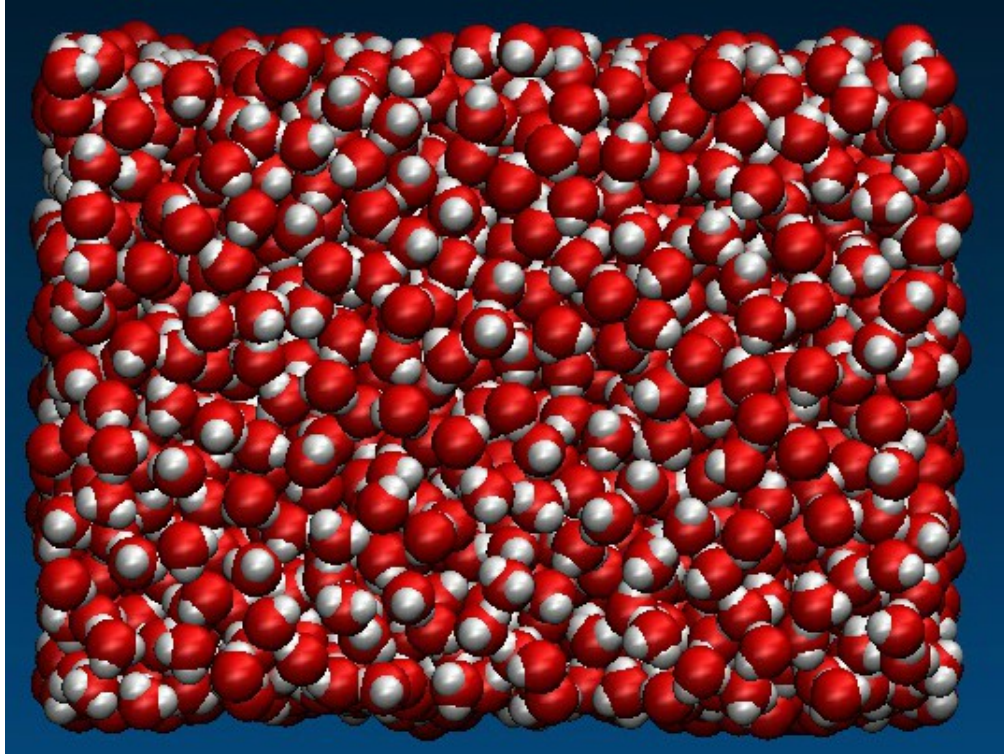


FIGURE 3.8: Molecular structures of epoxy from LAMMPS simulation post processing software (VMD).

TABLE 3.2: MD initial setup for graphene nanoreinforcement modeling

MD model setup	Graphene sheet
Units	Metal (atomic style)
Unit cell size	4 x 4
Boundary conditions	Periodic
Interatomic Potentials	Tersoff
Ensemble	NVT (T=300K)
Total number of atoms	32 Carbon atoms

In order to satisfy the bulk density of graphene ( $2.2 \text{ g/cm}^3$ ), the equilibrium distance between each carbon atom should be equal to  $3.4 \text{ \AA}$  as part of the initial conditions of MD simulation as shown in Table 3.2.

The LAMMPS code for modelling the graphene is given in Appendix B. The graphene sheet size was set as 5nm along x-direction and 10 nm along y-direction for matching with 2:1 stoichiometric ratio after blending with the epoxy matrix. The chirality angles of graphene were equal to  $0^\circ$  and  $30^\circ$  for armchair and zigzag configuration respectively and shown in Figure 3.9.

Here the periodic boundary conditions (PBC) were applied along the x direction of graphene edge for removing the finite length effect. The free boundary conditions were applied along the y direction. The applied boundary conditions prepare the graphene

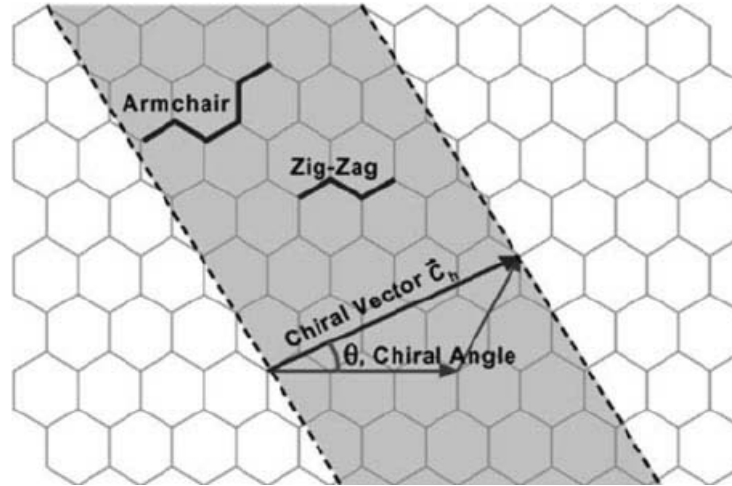


FIGURE 3.9: Schematic diagram of a hexagonal graphene sheet, zigzag, and armchair graphene sheet[15].

sheet for proper cross linking with epoxy matrix and the LAMMPS model is shown in Figure 3.10.

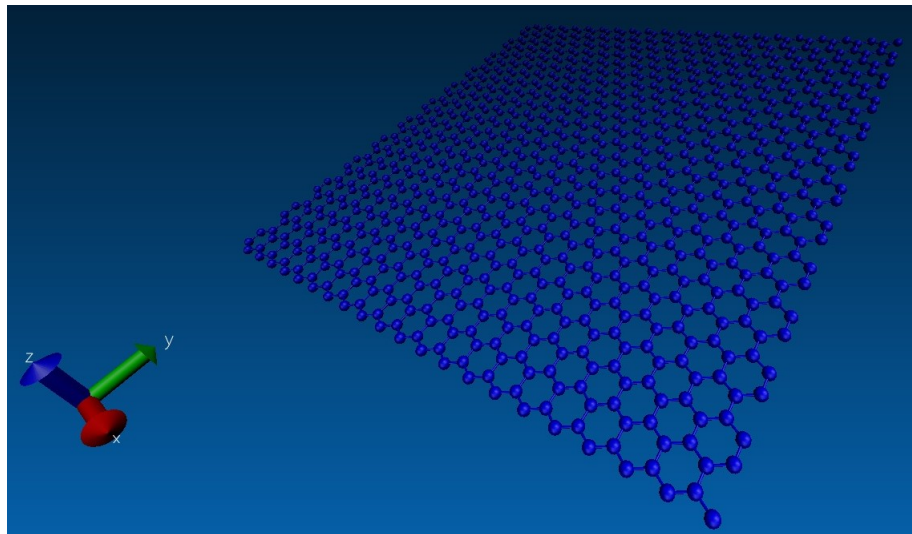


FIGURE 3.10: Lammps model for the graphene sheet

### 3.3.3 Interfacial Region Modeling

In order to produce good interfacial region and interfacial adhesion, the graphene sheet needs to be functionalized. The functional groups of OH and COOH were added on to the edges and also on to the surface of the graphene sheet in the LAMMPS model. The graphene sheet has two types of edges such as zigzag and armchair and the functional groups pair with them differently. Each carbon atom on the zigzag edge has an unpaired electron, making it easy to bond with the COOH and OH functional groups. However, at the armchair edge side, the carbon atoms are more stable due to the presence of triple

TABLE 3.3: Change in number of atoms during functionalization

Graphene sheet (32 atoms)	Functional groups percentage (%)	Number of atoms added by functional groups	Total number of atoms in graphene sheet
	3.0	7	39
	6.0	14	46
	9.8	23	55

covalent bonds and hence the functional groups leave a valency of oxygen atoms at the edges during functionalization.

These functional groups were randomly grafted onto the 36 carbon atoms from the graphene layer using LAMMPs code (refer Appendix C). The influence of grafting density on the mechanical properties of graphene was studied by randomly grafting these functional groups to the graphene sheet in different percentages, 3.0 % , 6.0 % and 9.8 %. The approximate number of atoms added to the graphene sheet by the functional groups is shown in Table 3.3. The effect of distribution of the COOH and OH functional groups on the graphene sheet showed optimum functionalization at 6.0 % of functional groups. The further increase in functionalization to 9.8 % distribution showed saturation and no improvement of properties.

Thus a functionalized graphene sheet to reinforce the epoxy matrix in a LAMMPs code will have 46 atoms (6% functional groups) (refer Appendix C). Further, these 46 atoms within the graphene system have similar interactions and properties (Covalent bonds of COOH, OH and one valency oxygen atom) and hence was defined as one united atoms. The functionalized graphene model is shown in Figure 3.11.

The functionalized graphene sheets were then used to develop the graphene epoxy nanocomposite models with one, two and three graphene sheets which represents 1.8 wt%, 3.7 wt% and 5.5 wt% respectively. The weight fraction of the nanoparticles were calculated using the total number united atoms modeled in LAMMPs code. For example, a functionalized graphene sheet consists of one united atom, whereas the epoxy resin consist of 52 united atoms. Thus adding one graphene sheet (1 united atom) with 52 united atoms epoxy gives the weight fraction of 1.8 wt% ( Refer Equation 3.23)

Based on the above calculation, the nanocomposites with three weight fraction (1.8 wt%, 3.7 wt% and 5.5 wt%) of graphene were modeled (Table 3.4). The graphene sheets were stacked normal to the loading axis (x axis) and parallel to each other during the modelling process. The free oxygen atoms within the functionalized graphene sheet formed covalent bonds with carbon atoms of the epoxy while developing the nanocomposite model. This mimics strong interfacial region bond between the graphene sheet and epoxy matrix. The average spacing (cutoff distance) between the two individual

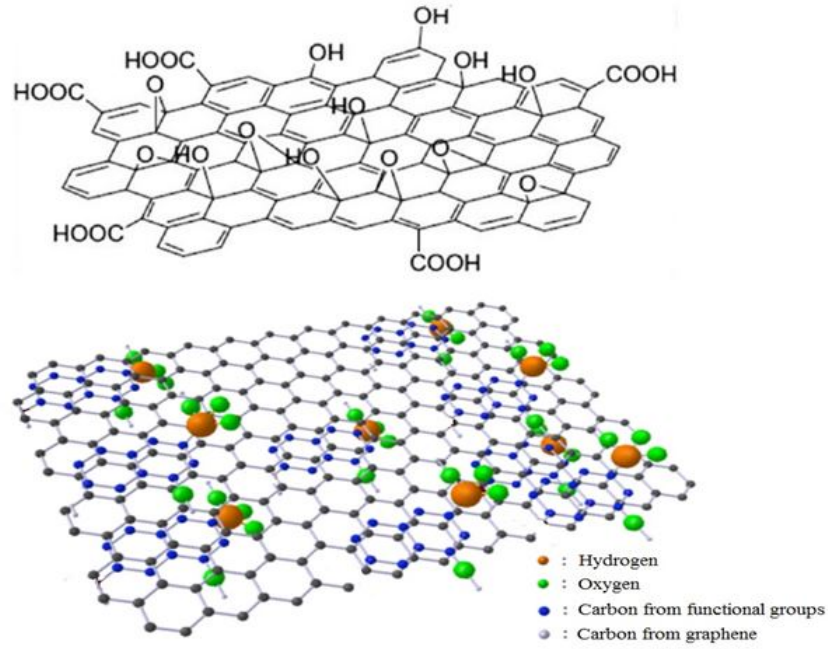


FIGURE 3.11: Functionalized graphene sheet

TABLE 3.4: Graphene weight fraction calculation

Model	Epoxy United atoms	Graphene United atoms	Weight Fraction %
1.8 % Graphene nanocomposite	52	1	1.8
3.7 % Graphene nanocomposite	52	2	3.7
5.4 % Graphene nanocomposite	52	3	5.4

constituents united atoms was set to be approximately  $2A^0$ . If the cutoff distance is not within the limit, the covalent bonds between the united atoms will be broken and thus reduce the bonding strength. Therefore for a better interfacial bonds within the nanocomposites unit cell, the interatomic forces between the constituents united atoms would be minimized to maintain the cutoff distance. This was achieved by pulling the united atoms together using the conjugate gradient [1] method and therefore improving the interfacial bond.

$$\frac{\text{Total number of united atoms in a Functionalized graphene sheet}}{\text{Total number of united atoms in Epoxy-graphene composite}} \times 100 = \text{weight fraction} \quad (3.25)$$

$$\frac{1}{52 + 1} \times 100 = 1.8\% \text{weight fraction} \quad (3.26)$$

TABLE 3.5: Material configurations of graphene epoxy nanocomposite system

Model	Unit cell dimension (Å)	Number of graphene sheets
1.8 % Graphene nanocomposite	a=9.84, b=19.02, c=1056.42	1
3.7% Graphene nanocomposite	a=9.84, b=19.02, c=2116.24	2
5.4% Graphene nanocomposite	a=9.84, b=19.02, c=3104.21	3

The size of the unit cell for the different weight fractions of graphene reinforcement configurations are listed in Table 3.5 where the unit cell dimensions are represented by length(a), breath(b) and width(c). Figure 3.12a shows a 3D model of a graphene epoxy nanocomposite structure and Figure 3.12b shows 2D model with 1, 2 and 3 graphene sheets configurations within the graphene epoxy nanocomposite.

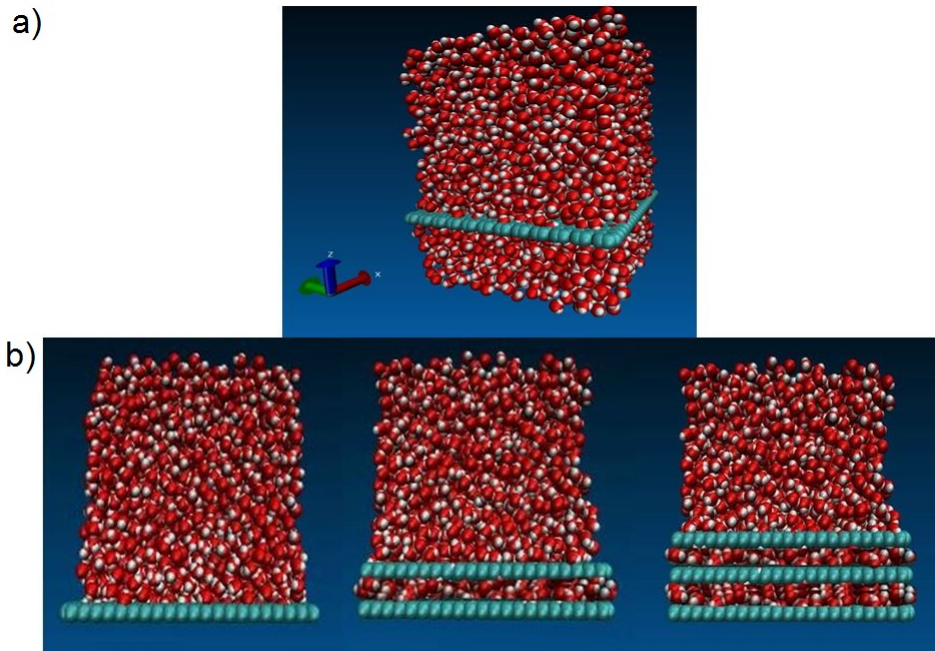


FIGURE 3.12: a) 3D model for the graphene epoxy nanocomposite 1 structure and b) 2D 1, 2 and 3 graphene sheets configurations within the graphene epoxy nanocomposite.

The next step was to define the interactions (bonding characteristics) between the united atoms of functionalized graphene sheet and epoxy within the nanocomposite unit cell. This modeling process was carried out using NVT based Molecular dynamic ensemble with 5000 time steps at 300K temperature. Time step size was maintained at 0.8-1.0 fs and the cut-off distance was  $2A^0$ . The positions and velocities of the united atoms were updated using verlet integration scheme[171] for every time steps. As the modeling analysis progress, the united atoms position change due to the change in temperature

and therefore the verlet integration update is essential for positioning the plane of the graphene sheets perpendicular to the loading axis.

To control the graphene weight fraction in the system, a number of graphene sheets were added one by one. The united atoms of the first graphene sheet shown in Figure 3.12a were then replicated for the second and third graphene sheets. This was done to manage the graphene concentration within the nanocomposite. After the addition of each sheet, verlet intergration scheme was used again to update the position and the velocities of the united atoms so as to determine the interaction and bond strength. The model of the graphene epoxy nanocomposite with different graphene weight fractions is shown in Figure 3.12b.

### 3.3.4 MD Interfacial region properties

For obtaining the interfacial region properties, both normal and shear traction-separation numerical experiments were conducted by slowly displacing the graphene sheet under displacement control within the unit cell in normal and shear directions. As specified before, the cut-off distance between the epoxy and graphene sheet united atoms was maintained at  $2A^0$  and the debonding cutoff distance was kept at  $20A^0$ . Beyond this value, the graphene sheet starts debonding from the epoxy matrix. The boundary conditions for both normal and shear traction numerical experiments were non-periodic along z-axis and non-periodic along xy plane respectively.

The rate of loading for the normal traction separation (pull out) experiment was at  $0.01 A^0/\text{fs}$  for the period 3 ps and for the shear traction separation (cohesive) experiment was at  $0.001- 0.0001 A^0/\text{fs}$  for the period 1.5 ps. The positions and velocities of the united atoms for each time steps were updated using the verlet time integration scheme. The tested model after final failure (beyond  $20A^o$ ) is shown in Figure 3.13.

As the graphene sheet was pulled, the reaction force ( $f_{ij}$ ) was developed at the interface between united atoms due to the nonbonded interactions (Lenard-Jones (LJ) potentials) by which the force versus displacement plots was obtained.

$$f_{ij} = -\frac{\partial}{\partial r_{ij}} 4\epsilon \left[ \left(\frac{\sigma}{r}\right)^{12} - \left(\frac{\sigma}{r}\right)^6 \right] \quad (3.27)$$

This induced reaction force causes the change in bond stretching, bond angle and deiheral within the optimized potentials for liquid simulations (OPLS), which was defined by the total potential energy ( $E(r^N)$ ) of the nanocomposite system. Then the elastic constants ( $C_{ij}$ ) for the MD model was obtained using the second derivative of the total

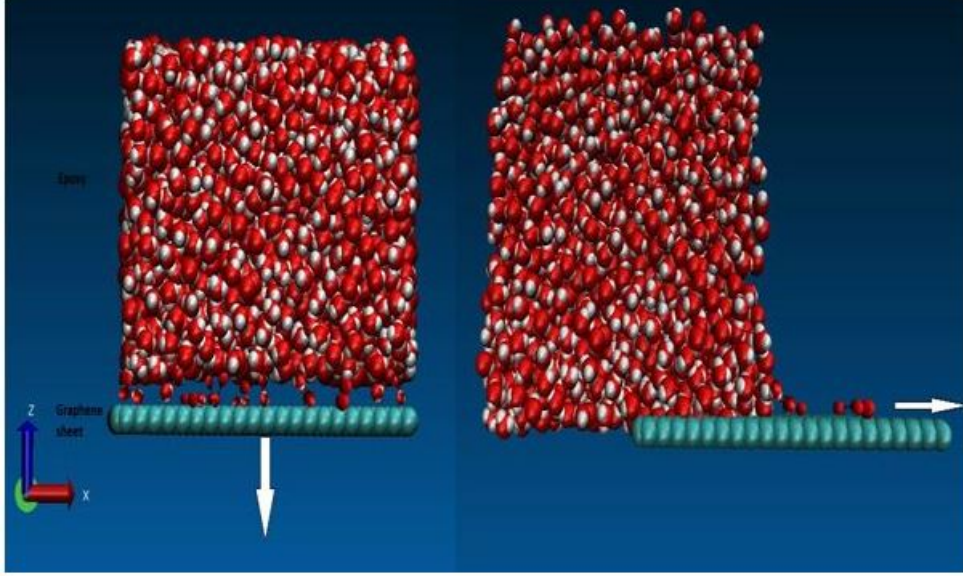


FIGURE 3.13: Normal and shear displacement of graphene sheet in graphene epoxy nanocomposite

potential energy (OPLS) with respect to the lateral strain components and the equation is given below,

$$C_{ij} = \frac{1}{V} \left( \frac{\partial^2 (E(r^N))}{\partial \varepsilon_i \partial \varepsilon_j} \right) \quad (3.28)$$

Where

$\varepsilon_i, \varepsilon_j$  are strain components,

$(E(r^N))$  is potential energy,

$V$  is simulation cell volume

The elastic properties can be written using Hooke's law as,

$$\sigma_{ij} = \sum_{i=0}^6 C_{ij} \varepsilon_{ij} \quad (3.29)$$

Where  $\varepsilon_{ij}$  represents the strain.

The elastic constants ( $C_{ij}$ ) for the united atoms  $i$  and  $j$  can be written as an elastic matrix. This is a  $6 \times 6$  matrix which describes the stress-strain behaviour of the nanocomposite and the elastic constant coefficients ( $\lambda$  and  $\mu$ ) within it. For the graphene epoxy nanocomposite system, the elastic moduli was therefore calculated within LAMMPS by following this equations,

$$\text{Young's modulus (E)} = \mu \left( \frac{3\lambda + 2\mu}{\lambda + \mu} \right) \quad (3.30)$$

$$\text{Bulk modulus (K)} = \lambda + \frac{2}{3}\mu \quad (3.31)$$

$$\text{Shear modulus (G)} = \mu \quad (3.32)$$

$$\text{Poisson's ratio (v)} = \frac{\lambda}{2(\lambda + \mu)} \quad (3.33)$$

All the properties of the interfacial region are calculated within the LAMMPS code and then tabulated for obtaining the over all mechanical properties of the graphene epoxy nanocomposite materials. Finally, when the bond stretching energy of the united atoms reached a point closer to the failure (beyond  $20A^0$ ), the united atoms were debonded and the associated angles and dihedrals were deleted resulting in separation along both normal and shear direction. This displacement and stress properties were then used in coupling of molecular dynamics modeling with finite element analysis.

## 3.4 Finite Element Analysis Procedure

### 3.4.1 Macroscale Model

In this section, the FEA macroscale model was attained using the parameters acquired from the nanoscale model properties giving coordinates of the matrix and nanoreinforcement for macroscale model. The initial boundary conditions were extracted from the nanoscale as shown in Figure 3.14 below and were applied on FEA simulations to create the macroscale model.

The displacement and elements parameters extracted from the nanoscale model were therefore used to conduct a static FEA modeling of the nanocomposite. This parameters were defined in terms of dimensions, nodal points and geometry by the displacement vectors.

The formulation of these vectors in relation to the initial conditions obtained from the molecular dynamics analysis were used to formulate the coordinate system for the nodes and elements within the graphene epoxy macroscale model. To this purpose, FEA simulations were performed using MatLab script (refer to appendix D) to calculate the

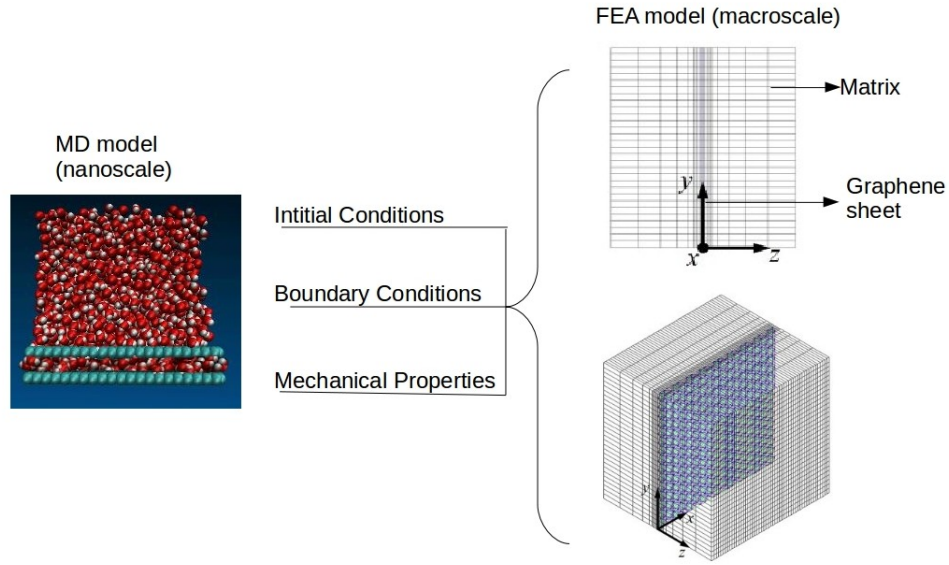


FIGURE 3.14: Extraction of initial conditions and boundary conditions from MD scale to macro scale (FEA)

nanocomposite mechanical properties using representative volume elements (RVEs) of the structure.

### 3.4.2 Analysis Procedure

Due to computational limitations and modeling complexities, in finite element modeling numbers of elements within the macroscale RVEs were limited to 100 as shown in the Matlab script (refer Appendix D). For a cubic geometry of the nanocomposite model, the size of the RVE was accordingly adjusted based on the averaged weight fraction of the nanoreinforcement from MD analysis. In order to accurately model the desired weight concentration of graphene nanoreinforcement to epoxy matrix inside RVE, models were constructed in a way to satisfy periodicity criterion (similar to periodic boundary conditions). This means that if a filling particle passes one boundary side of the RVE, the remaining part of that particle continues from the opposite side.

For each mesh element, properties were averaged according to the imported density map, and the effective properties of the entire macrostructure as calculated based on the nanoscale model of the nanocomposite. Properties obtained from the nanoscale averaged results were then assigned to the grid representing graphene in the overall nanocomposite RVE model using the properties listed in Table 3.6 below as further input.

From molecular dynamics simulations, the averaged values for the thickness of the nanoreinforcement used in the FEA model are shown in Table 3.7. Equilibrium thickness,

TABLE 3.6: The nanocomposite properties extracted from the nanoscale transferred to the macroscale.

Properties	Graphene epoxy nanocomposite
Young's modulus(E)	4.56
Weight fraction(%)	3.7
Poisson's ratio ( $\nu$ )	0.36

radius and mechanical properties attained from the Irving kirkwood averaging calculations of displacement properties were also illustrated. E is the Young's modulus,  $l$  is the equilibrium thickness and Y is the in-plane tensile rigidity.

TABLE 3.7: Averaged properties for FEA modelling

Radius (cm)	E (TPa)	$l$ (cm)	Y (TPa)
2.5	3.74	0.142	0.329
5.0	3.80	0.141	0.330
9.5	3.76	0.141	0.327

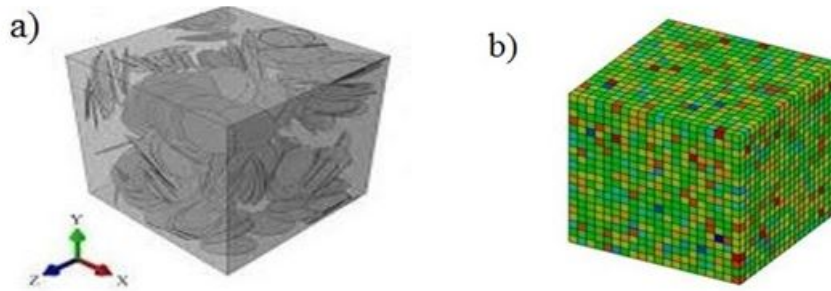


FIGURE 3.15: a) 3D cubic RVE filled with graphene nanoreinforcement with aspect ratio of 100. b) Flexible meshing of RVEs, each disc was partitioned into four symmetric parts

The predictions of representative macroscopic properties of graphene epoxy nanocomposites considered in this work were the final step of the multiscale modelling strategy. FEA calculations were performed in order to analyze the overall nanocomposites properties. The density profiles obtained from nanoscale simulations were mapped to a fixed cubic grid in macroscale model. The resulting effective properties were estimated using an energy minimization method (refer to Appendix D). In Figure 3.15 a) a 3D cubic RVE filled with graphene nanoreinforcement with aspect ratio of 100 is illustrated and in Figure 3.15 b), for a better and more flexible meshing of RVEs, each disc was partitioned into four symmetric parts.

## Chapter 4

# Results and Discussion

The numerical results and the corresponding discussions are presented in this chapter. At first, the MD modelling of the graphene sheet functionalized with OH and COOH functional groups (3%, 6%, and 9.8%) were completed. Then the functionalized graphene sheet with the better bonding properties was acquired. The better bonding properties were determined by the valency of the oxygen atoms attached to the functionalized graphene sheet. Subsequently, the MD modelling of the functionalized graphene sheet with epoxy matrix was developed to obtain the interfacial properties. The different weight fractions of graphene sheets were attached to the epoxy matrix, and the best weight fraction was obtained by checking the cross linking between the graphene sheet and the epoxy matrix. The modelled graphene-epoxy nanocomposites were then tested to obtain the interfacial properties by applying a displacement (normal and shear direction) to the graphene sheet. As the displacement was applied, the traction forces were obtained to characterize the interfacial properties of the developed nanocomposites. The MD modelled nanocomposite properties were transferred to the macroscale model by coupling the two scales. The coupled models were then analyzed to obtain the elastic properties of the graphene-epoxy nanocomposite. The results were then validated with the available literature. The graphene-epoxy composite with 3.7% weight fraction of functionalized graphene have shown improved properties and the results was in agreement with the literature data.

### 4.1 MD modelling of graphene functionalization

The graphene sheets were functionalized with COOH and OH functional groups. As explained in Chapter 3, the graphene sheets were grafted with 3.0%, 6.0% and 9.8% of the functional groups with increasing time and shown in Figure 4.1. As the time

increased, the bonds were formulated between the graphene sheet and the functional groups with oxygen and hydrogen atoms creating covalent bonds with carbon atoms upto 75 fs. As the functionalization process started, there was a gradual increase in grafting percentage at 45fs. This is because, after 5% grafting, the graphene sheet showed signs of saturation in functionalities due to the number of valence oxygen atoms attached during functionalization.

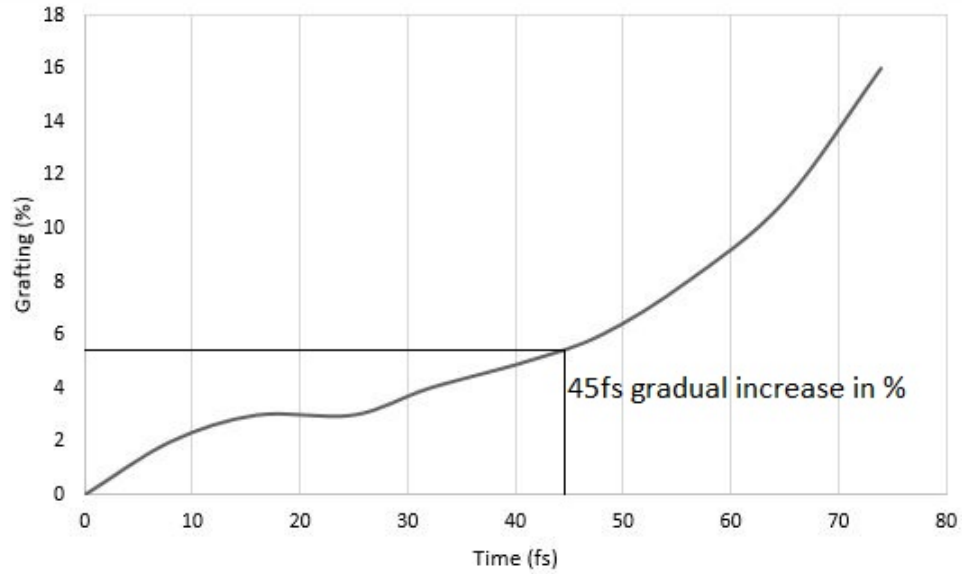


FIGURE 4.1: Graphene functionalization grafting percentage with time

The Young’s Modulus and strength of the functionalized graphene sheets were calculated within the LAMMPS script using the minimization commands by varying the LJ parameters. The results are given in Table 4.1 along with the comparative experimental results. The Young’s modulus and tensile strength of 3% grafted graphene sheet was very low compared with 9.8 % grafted graphene.

The required mechanical properties were of the 6.0 % grafted graphene sheet shown in the table and hence was selected best for improving the epoxy properties within the nanocomposite. This validated the the LAMMPS results for graphene functionalization with experimental data [172].

TABLE 4.1: Validation of MD results with experimental data.

Graphene Sheet Properties	Young’s Modulus E(TPa)	Strength (GPa)
3% grafted sheet	0.64	98.3
6% grafted sheet	0.89	121
9.8% grafted sheet	1.53	127
Experimental Graphene Sheet	1.00	123.5

## 4.2 Graphene and Epoxy cross-linking

The functionalized graphene sheet was cross linked with epoxy matrix. At first, the graphene epoxy unit cell was equilibrated at room temperature of 300 K to reach a balanced state, as the density of the unit cell fluctuates in a small range around the target temperature. The equilibration was done by controlling the NVT parameters within the LAMMPS code, which provided the temperature versus specific volume curves. These curves define the cross linking behaviour of epoxy-graphene nanocomposite and shown in Figure 4.2.

The cross linking was started with one graphene sheet, and the specific volume of the unit cell was constant at low temperatures as there was no change in thermal properties (expansion). At 350K (transition temperature), the specific volume started to increase rapidly due to the expansion of unit cell as the temperature increased further. The specific volume at this transition temperature for one graphene sheet was  $0.86 \text{ cm}^3/\text{g}$  showing incomplete cross linking in this unit cell. As the nanocomposite approached higher cross-linking temperatures, the specific volume increase was more gradual and the unit cell united atoms packed closely to each other.

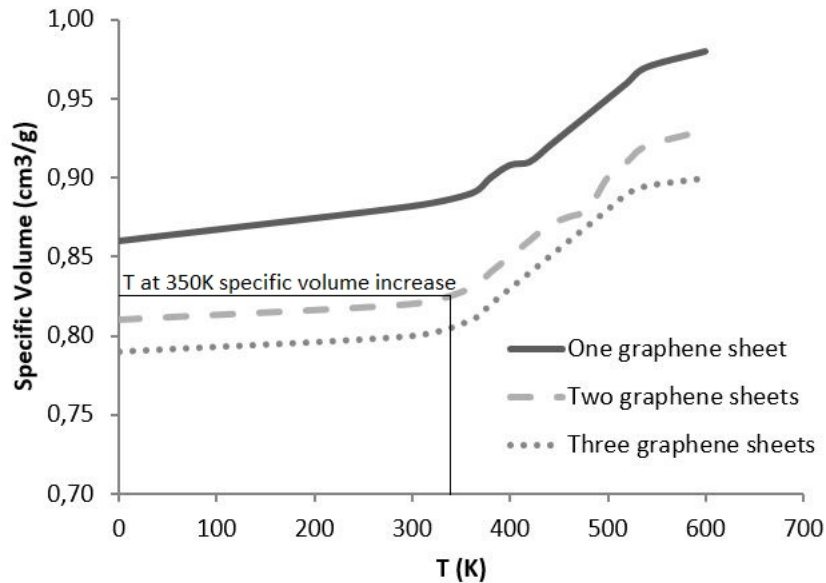


FIGURE 4.2: Specific volume vs temperature for epoxy nanocomposite

Further adding two graphene sheets showed closed and perfect bonds. This was first shown by the specific volume at transition temperature for two graphene sheets nanocomposite ( $0.82 \text{ cm}^3/\text{g}$ ). The cross-linking of two graphene sheets with the epoxy matrix showed improvement in the formation of covalent bonds between the united atoms therefore demonstrating a strong cross-linking. The addition of the third graphene sheet showed saturation in cross-linking of the united cell atoms at high specific volume of

0.89  $cm^3/g$ . The reason behind this phenomenon is that at this point the number of valence united atoms increased. This means that Van Der Waal forces were more between the united atoms due to the unbonded atoms within the unit cell. The transition temperature (at 350 K) was the corresponding temperature at the slight inflection point of the slopes of specific volume versus temperature linear curves. This therefore was a way to determine a perfect weight fraction for the graphene epoxy nanocomposite which proved to be of two graphene sheets (3.7% weight fraction).

Each layer of graphene sheet added to the epoxy matrix increased the mechanical properties of the nanocomposite. The elastic modulus increased with the addition of each graphene sheet and the two graphene sheets (weight fraction = 3.7%) achieved the highest modulus. Adding a third graphene sheet showed saturation in mechanical properties. This is shown in Figure 4.3.

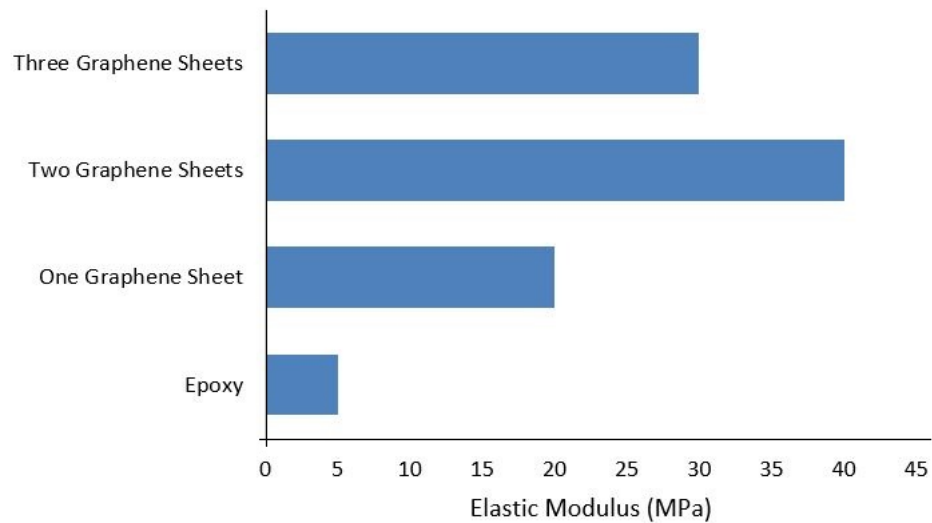


FIGURE 4.3: Mechanical properties change with addition of graphene sheets

### 4.3 Interfacial region properties

After the unit cell was equilibrated, the graphene sheet was then displaced to obtain the interfacial region properties along the normal and shear directions. The interface between graphene and epoxy plays a significant role in load transfer mechanism at the nanocomposite interfacial region.

The displacement applied along the normal direction of graphene helps to understand the pullout mechanism between graphene and epoxy as shown in Figure 4.4. As the graphene sheet was pulled under the displacement control, a reaction force was developed at the interface between graphene sheet and matrix. As it could be seen from figure that the

force-displacement curve is linear at the initial stage and reached a maximum force of 6.2 pN at the displacement of 0.13 nm. The normal force was enhanced with increased aspect ratio of the graphene sheet. In this study, the magnitude of the normal force is seen to be very small which mostly resulted from van der waal forces interaction between graphene and epoxy. Such normal force may be increased by minimizing the gap between graphene and epoxy or introducing more covalent bonds between graphene and epoxy.

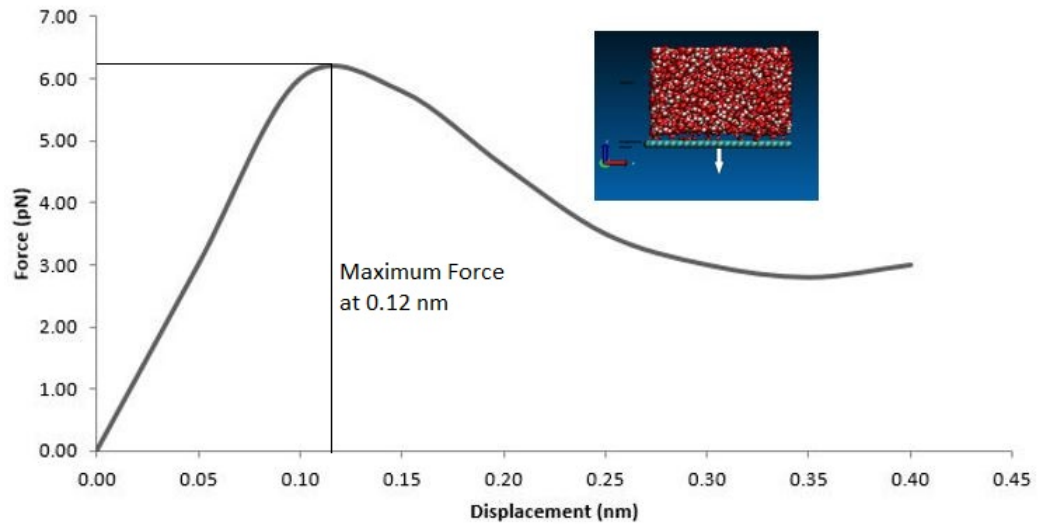


FIGURE 4.4: Normal force verses displacement plots at the interfacial region.

The shear displacement provided information about the shear mechanism of the graphene sheet from the epoxy matrix. Figure 4.5 shows shear force verses displacement curve at the interfacial region for the graphene epoxy nanocomposite. The maximum force and the displacement for shear force is seen to be 6 pN and 0.04 nm. It shows a non linear behaviour before reaching a peak point. The shear force then gradually drops with increased displacement.

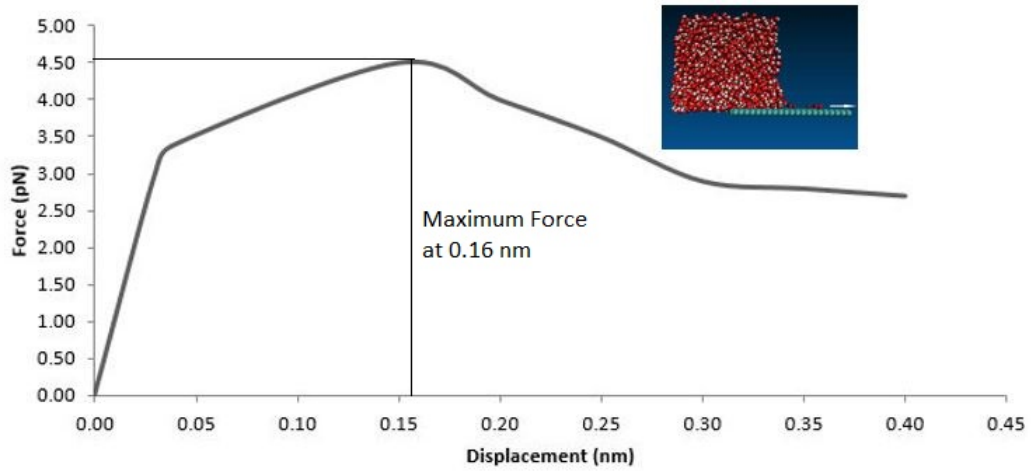


FIGURE 4.5: Shear force versus displacement plots at the interfacial region.

### 4.3.1 Traction separation of Graphene (normal displacement)

By measuring atom-by-atom separation as a function of traction, the traction-separation relationships for graphene and epoxy was obtained and plotted as given in the following subsections.

The MD analysis was performed efficiently to extract the equilibrium properties (meaning force and potentials of the mean force built in LAMMPS) from non-equilibrium processes (MD simulations). The traction versus displacement response for normal separation is shown in Figure 4.6. The traction stresses were calculated by dividing the traction force with the initial section area of the composite (equal to an effective graphene area). The traction strengths increases up to 1 nm displacement and then started to decrease. Then the values were approximately constant from 2 nm to 10 nm. From 2.5 nm the traction curves shows significant fluctuations, and this indicates that 2.5 nm is the point where the number of interfacial bonds results in a converged response for the separation of the graphene sheet from the epoxy matrix.

### 4.3.2 Traction separation of graphene (shear displacement)

As shown in Figure 4.7, traction increased as separation increased, reaching a peak value at 1.0 nm. This portion of separation - traction curve corresponds to the behaviour of atoms on the interfacial region during deformation. The peak value of traction was the critical fracture stress at which crack initiation occurred and it directly corresponds to the highest traction stress. Further increase in separation led to a traction decrease and eventually reached to minimum level from 8.3 nm. The area under this curve is equal to the energy needed for separation.

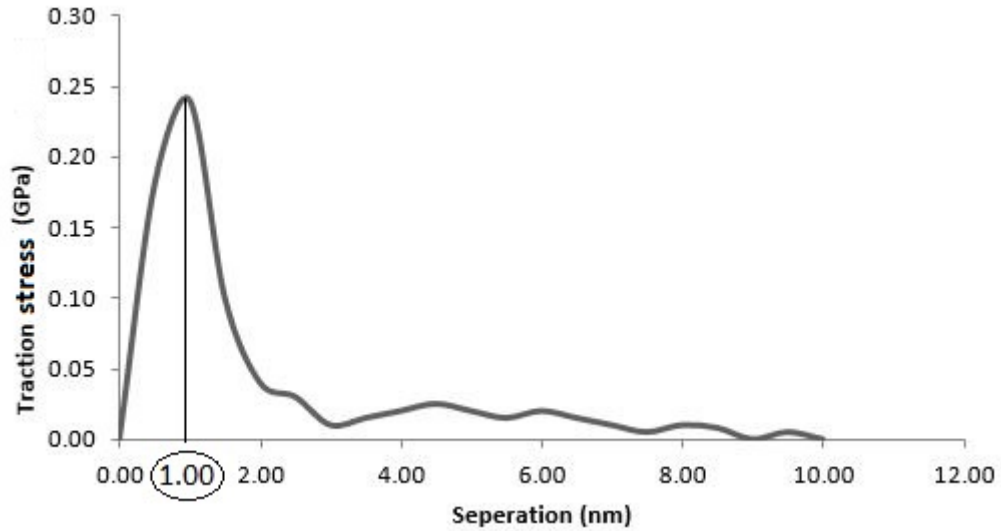


FIGURE 4.6: Traction separation of graphene under NVT ensemble (Normal)

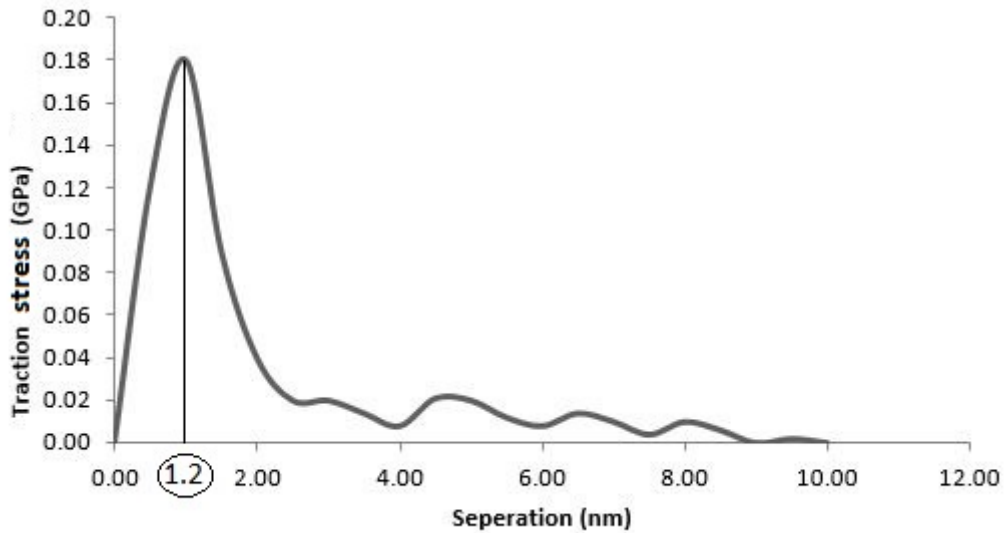


FIGURE 4.7: Traction on graphene under NVT ensemble (shear)

### 4.3.3 Radial distribution function

After the graphene sheet was displaced from the epoxy matrix, the position and distribution of atoms were analyzed to determine the radial distribution function. The position and distribution were analyzed by determining the change in density as a function of distance between united atoms. Radial Distribution Function ( $g(r)$ ) provided distribution pattern of graphene epoxy nanocomposite with one, two and three graphene sheets in a graphene epoxy nanocomposite system.

#### 4.3.4 Graphene Epoxy Nanocomposite RDF

The radial distribution function (RDF), was obtained directly from the MD simulations, which gave a measure of influence of nanoreinforcement on the nanocomposite structure. In Figure 4.8, the first peak at 3.0 nm representing the graphene epoxy nanocomposite of 1.8% weight fraction (one graphene sheet) was stronger due to the addition of functionalized graphene sheet on the epoxy matrix. This noticeable sharp peaks in the RDF ensured the amorphous nature of the graphene-epoxy system. The highest peak for one graphene nanocomposite was observed at 3.9 nm which indicated the maximum concentration of atoms in the entire system at this pairwise distance. The influence of graphene concentration was seen to be insignificant on RDF for 1.8 w% graphene epoxy nanocomposite.

The highest and lowest values of  $g(r)$  were seen in epoxy nanocomposite with two graphene sheet systems with 3.7% graphene concentrations. The lowest value of the radial distribution function was seen at  $1.2 \text{ \AA}$ , while the highest peak was noticed at  $3.9 \text{ \AA}$ . The subsequent intra-molecular peaks results from distance between atoms, including hydrogen and carbon atoms within the nanocomposite system. As the content of graphene increased, the overall molecular RDFs decreased for the direct chemical bonds between hydrogen and other atoms. However, the RDFs behaviour changed for other bonds.

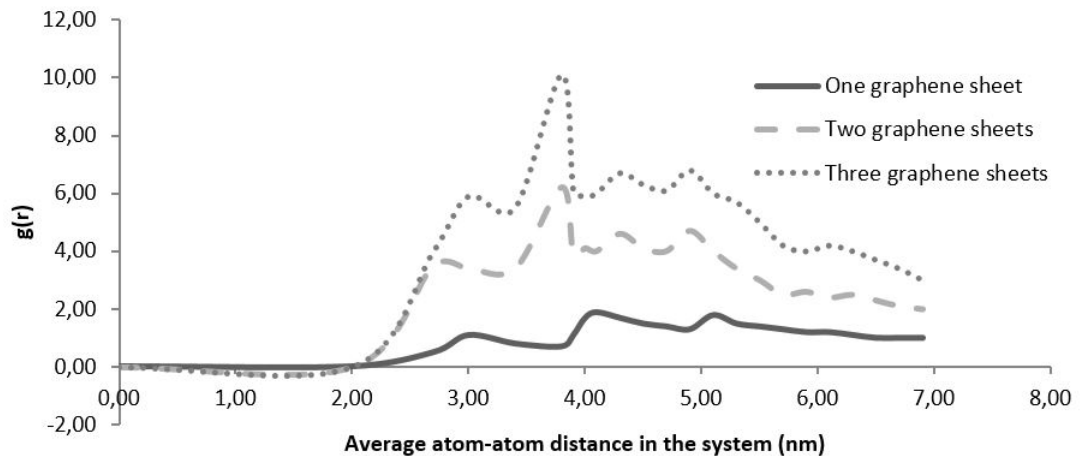


FIGURE 4.8: RDF pattern for graphene and epoxy particles in a epoxy nanocomposite.

The variations between individual plots of one and two graphene sheets nanocomposites are comparatively insignificant. This might explain the similarity in stress-strain response data for this systems in the next sections. Significant difference was not observed in the RDFs since the density remains almost the same in all the systems.

In graphene epoxy nanocomposite with three graphene sheets, the highest and lowest values of the radial distribution function are seen shown in Figure 4.8. The radial distribution function of three graphene sheets and two graphene sheets are very similar. Such observations are possibly due to insignificant variations in densities. In both cases, a distinguishable sharp peak was observed at  $3.9 \text{ \AA}$ . These sharp peaks correspond to carbon atoms that are connected by one or two bonds within system. The contribution of carbon-carbon bonds from both graphene structure are also attributed by this peak.

#### 4.4 Atom density

During molecular modeling in all the unit cells, the number of graphene sheets were changed to obtain necessary weight fraction. Thus, atom density in a unit cell varied with respect to different weight percentage. Figure 4.4 shows atom densities as a function of graphene concentrations in the unit cell for one, two and three graphene sheets nanocomposite.

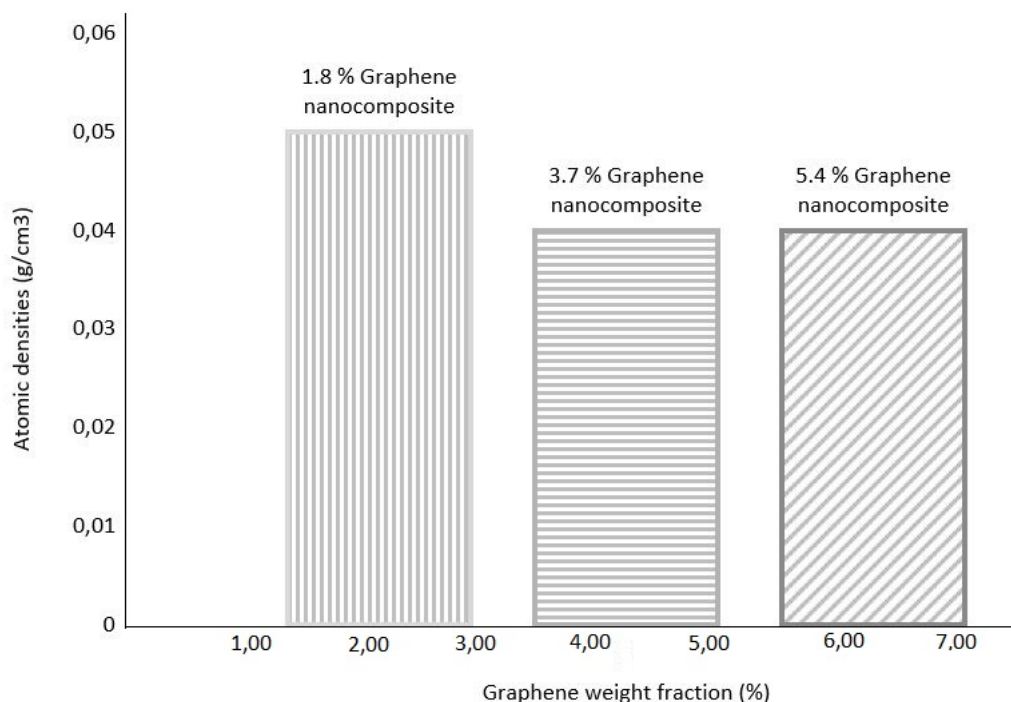


FIGURE 4.9: Atom densities as a function of graphene concentrations nanocomposite.

The atom density of graphene epoxy system with two and three graphene sheets was significantly low and the corresponding Young's modulus was also significantly low. Highest atom density was observed in unit cells with 1.8% graphene content including highest Young's and shear modulus. The atom densities for the nanocomposite with two graphene sheets system in Figure 4.4 showed comparatively weaker pairwise correlation than the

one with 5.4% graphene weight fraction. This was possibly due to lower RDF in this system.

## 4.5 Bond Stretching During Deformation

After separation of the graphene sheet from epoxy matrix, this analysis was also carried out in order to study the structural parameters such as pairwise bond stretch due to applied strain. The bond stretch play an important role in predicting the stiffness of the nanocomposite. As shown in Figure 4.10, the very first data at 0% strain is believed to be irrelevant in this analysis as the atoms undergo local relaxation between 0% strain and first deformation.

The epoxy nanocomposite with two graphene sheets and the epoxy nanocomposite with one graphene sheet have very similar slopes although the average pairwise bond deformed comparatively faster in epoxy nanocomposite with two graphene sheets than epoxy nanocomposite with one graphene sheet. The strain versus bond stretch plot for the graphene epoxy nanocomposite is shown in Figure 4.10

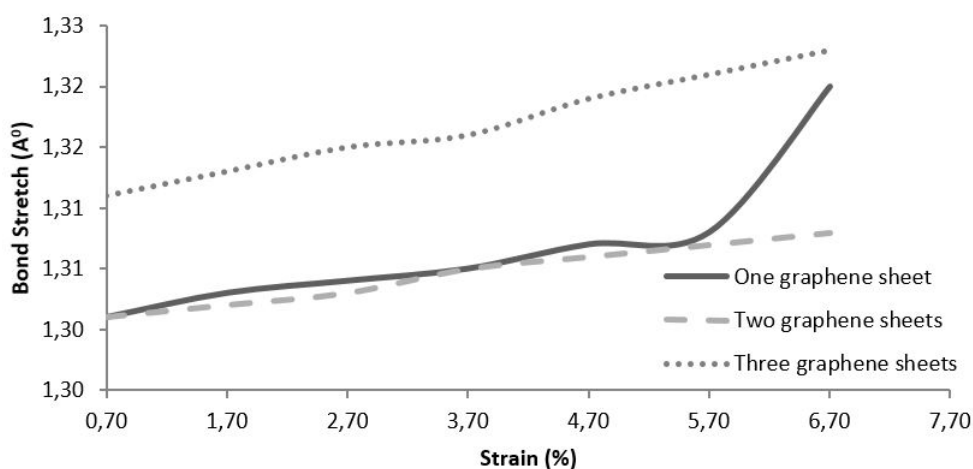


FIGURE 4.10: Bond stretch under applied strain for graphene epoxy nanocomposite.

The average bond stiffness for the three graphene epoxy nanocomposite (5.4% weight fraction) is slightly higher than the other two nanocomposite configurations. Stiffer pairwise bonds in epoxy nanocomposite with three graphene sheets resulted less stretch in the bond length.

## 4.6 Angle Bending for Epoxy Nanocomposite

This analysis was also carried out in order to study the inherent structural parameters such as pairwise bond angle bending due to applied strain. Similar to the bond stretch, bond angle also played a part in predicting the stiffness of the nanocomposite. The angle bending increased with increasing strain.

In graphene epoxy nanocomposite with two graphene sheets the average pairwise bond angle rates with respect to applied deformation were almost the same as those of graphene epoxy nanocomposite with one graphene sheet as shown in Figure 4.11. These curves are almost parallel spaced with different initial angle bending. Hence, this may also explain the highly correlated stress strain response and potential energy evolution for this unit cells.

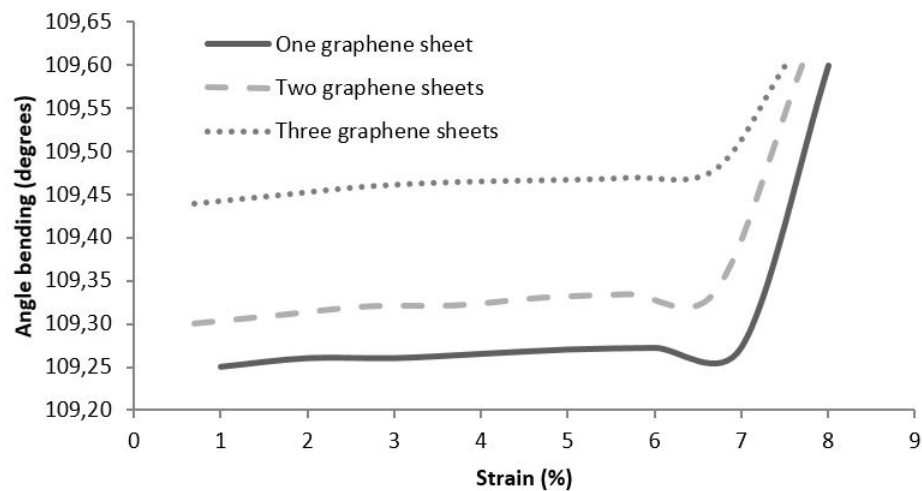


FIGURE 4.11: Angle bending under applied strain for epoxy nanocomposite

The strain versus bond angle curve for the three graphene epoxy nanocomposite (5.4% weight fraction) showed that the average bond stiffness was slightly higher than the other two nanocomposite configurations.

The average bond angle vs applied strain curves were similar for epoxy nanocomposite with two and three graphene sheets systems. Initial bond angles are observed to be less for epoxy nanocomposite with one graphene sheets compared to epoxy nanocomposite with three graphene sheets which correlate with the the number of graphene sheets.

## 4.7 Molecular Energy

The displacement of the graphene sheet in MD simulations caused change in atom positions, velocities and overall molecular structure resulting in an increase in overall potential energy. The potential energy had comparatively larger contribution in total molecular energy than van der Waals energy. The change in molecular energy followed by applied deformation indicated the sensitivity of the molecules against applied strain. Molecular energy verses strain plots for graphene epoxy nanocomposites with graphene concentration 1.8%, 3.7% and 5.4% is shown in the following sections.

The strain versus molecular energy for a unit cell with one graphene sheet showed gradual fluctuations in molecular energy. This is possibly due to a low modulus provided by 1.8% weight fraction of graphene. The increase in slope of molecular energy then clearly explained the deformation in the molecular topology with applied displacement. The plot for molecular energy variation with strain for graphene epoxy nanocomposite with one graphene sheet is therefore shown in Figure 4.12

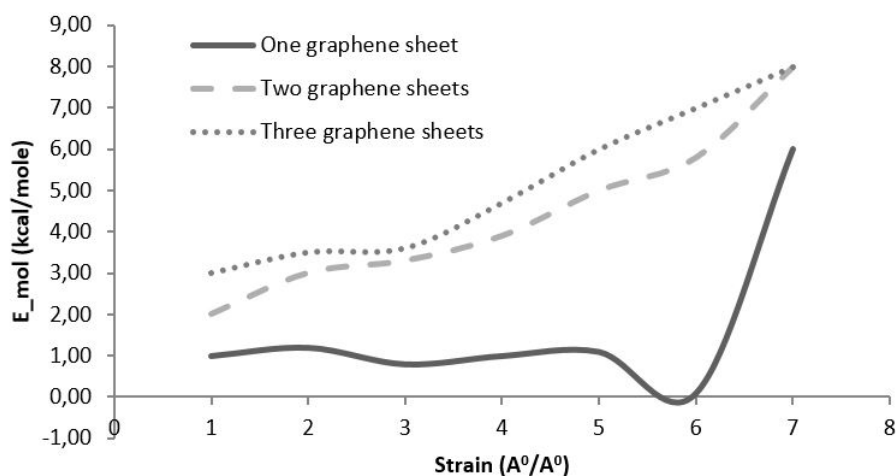


FIGURE 4.12: Molecular energy variation with strain for graphene epoxy nanocomposite.

The molecular energy curve of two graphene sheets unit cell is seen to be comparatively steeper and higher for unit cell with 3.7% graphene which provided higher modulus than than of one graphene sheet. This increase in slope implies higher modulus provided by the increase in number of graphene sheets.

The change in molecular energy is observed to be very small with 5.4% graphene, three graphene sheets though showing comparatively higher molecular energy depicted by Figure 4.12. It is to be noted that the amount of molecular energy was also seen to be higher with increased aspect ratio.

## 4.8 Stress/strain for graphene epoxy nanocomposite

The simulated stress-strain responses of graphene epoxy nanocomposites with graphene concentrations (1.8%, 3.7% and 5.4%) were plotted in the following sections. The values of Young's modulus (E) were determined from the slope of individual curves. The fluctuations in the stress-strain responses were minimized by applying moving average technique as shown in LAMMPS analysis. In Table 4.2, Young's modulus E and shear modulus G of graphene epoxy nanocomposites calculated by molecular dynamic (MD) methods are provided.

TABLE 4.2: Young's modulus E and shear modulus G of graphene epoxy nanocomposites

Material Configuration	Weight fraction (%)	Young's modulus E (GPa)	Shear modulus G (GPa)	Young's modulus from MD stress strain response (GPa)
One Graphene Sheet	1.8	4.56	1.73	5.00
Two Graphene Sheets	3.7	3.98	1.37	3.98
Three Graphene Sheets	5.4	2.98	1.07	3.56

It was seen that modulus of nanocomposites with lower graphene concentration (1.8% weight fraction) was comparatively higher than the same with higher concentration (5.4% weight fraction). This is possibly due to the variation in atom density. The results showed high E value with decreased aspect ratio in comparison to increased aspect ratio. The results of this study showed highest G (1.73 GPa) with lowest graphene concentration (1.8%) and lowest aspect ratio (150).

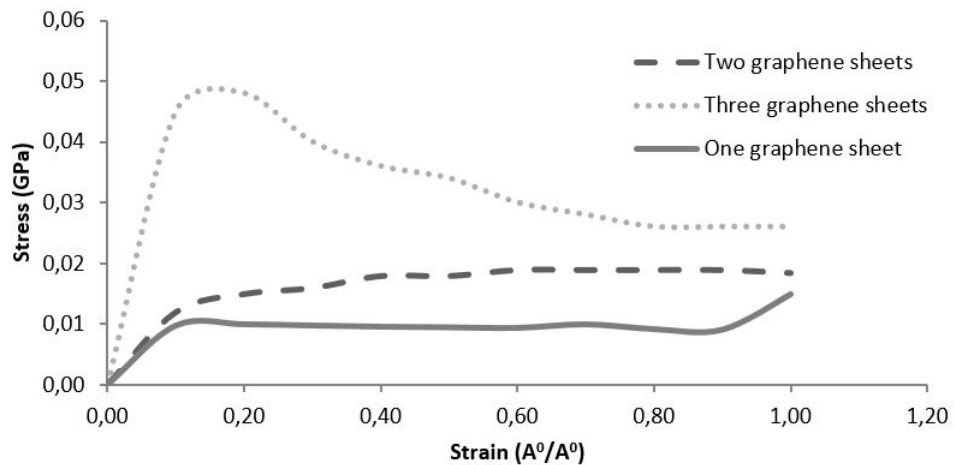


FIGURE 4.13: Stress-strain responses of graphene sheets nanocomposite

The Young's modulus showed low values in graphene epoxy nanocomposite system with 3.7% by weight concentration of graphene. In the atomistic models, distribution of

atoms, atom density and change in molecular energy in the unit cell play an important role in defining the properties. Hence, increasing Young's moduli with respect to weight fraction of graphene sheets may not be realistic in actual scenario. Figure 4.13 shows the stress-strain response for graphene sheets nanocomposite.

Adding three graphene sheets show reduced elastic modulus with increased graphene concentration (1.8% to 5.4% weight fractions) shown in Figure 4.13. It is to be noted that the Young's modulus calculated experimentally [173] shows higher values with increased graphene concentrations but in numerical simulations a similar trend is not observed. It is to be mentioned that increased concentration also enhances possibility of agglomeration in the system. Hence, the prediction shows increasing nature in Young's modulus with the increasing weight fraction of nanoreinforcement.

The Young's moduli for different graphene epoxy configurations were seen to be in the range 1.77 - 5.0 GPa by simulations due to the functionalized graphene sheet. The results of this study show highest shear modulus (1.73 GPa) with lowest graphene concentration (1.8%).

#### 4.8.1 Dispersion and agglomeration effects

Dispersion, agglomeration effects and elastic modulus calculated from stress-strain response for stacked graphene model are illustrated in Table 4.3. These parameters are calculated from the stress-strain responses in the x, y and z directions. The in-plane Young's modulus,  $E_x$  and  $E_y$  for the dispersed system (4.81 GPa, 8.76 GPa) is comparatively higher than the same in agglomerated system (3.99 GPa, 5.67 GPa). Dispersed graphene with high aspect ratio is seen to provide improved in-plane Young's modulus.

The in-plane modulus in three graphene system is comparatively larger than single graphene system. This indicates that in-plane modulus is significantly influenced by graphene volume fraction since graphenes in-plane property is significantly high (Young's modulus, 1 TPa). However, the out of plane Young's modulus,  $E_z$  of the graphene epoxy nanocomposites is mostly controlled by stiffness of epoxy and non-bonded interaction (van der Waals) between graphene-epoxy or graphene-graphene. The results show lowest  $E_z$  value (0.32 GPa) for three layer dispersed graphene system. The highest  $E_z$  value (2.36 GPa) was provided by three layer agglomerated system. The single layer graphene system shows  $E_z$  equals to 0.9 GPa.

TABLE 4.3: Dispersion and agglomeration effects

Material Configuration	Number of graphene sheets	$E_x$ (GPa)	$E_y$ (GPa)	$E_z$ (GPa)
One graphene sheet	1	1.89	1.94	0.9
Two graphene sheets	2 (dispersed)	4.81	8.76	4.32
Three graphene sheets	3 (agglomerated)	3.99	5.67	2.36

## 4.9 Effects of number of graphene sheets

The dispersion of graphene nanoreinforcement on the epoxy matrix improves the interfacial region properties therefore improving the macroscale properties of the nanocomposite. In the macroscale analysis the variation of different mechanical properties with different number of graphene sheets are as shown in Figure 4.14.

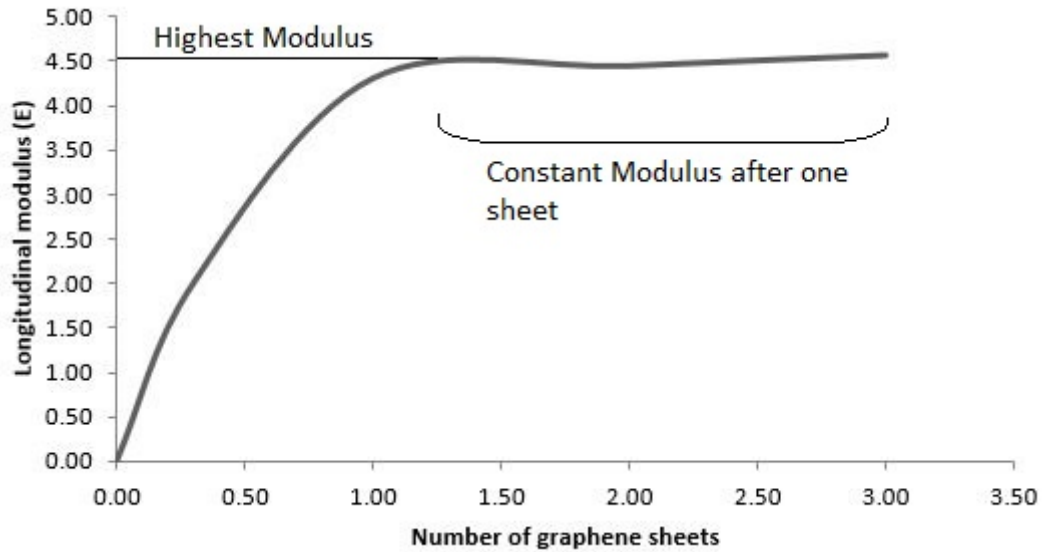


FIGURE 4.14: Longitudinal modulus of the RVEs versus number of graphene sheets.

The Longitudinal modulus increases constantly with increase in number of graphene sheets. At one graphene sheet we then see a peak value of the Longitudinal modulus at 4.5 GPa. This shows that addition for the graphene nanoreinforcement increased the mechanical properties until there was no change (constant modulus).

As the normal modulus versus the number of graphene sheets was close to constant, the stiffness of the RVEs in the normal direction was not affected much by the increase of graphene sheets. Transverse modulus showed a jump with the addition of the first graphene sheet and then consistency with the second and third sheet as shown in Figure 4.15.

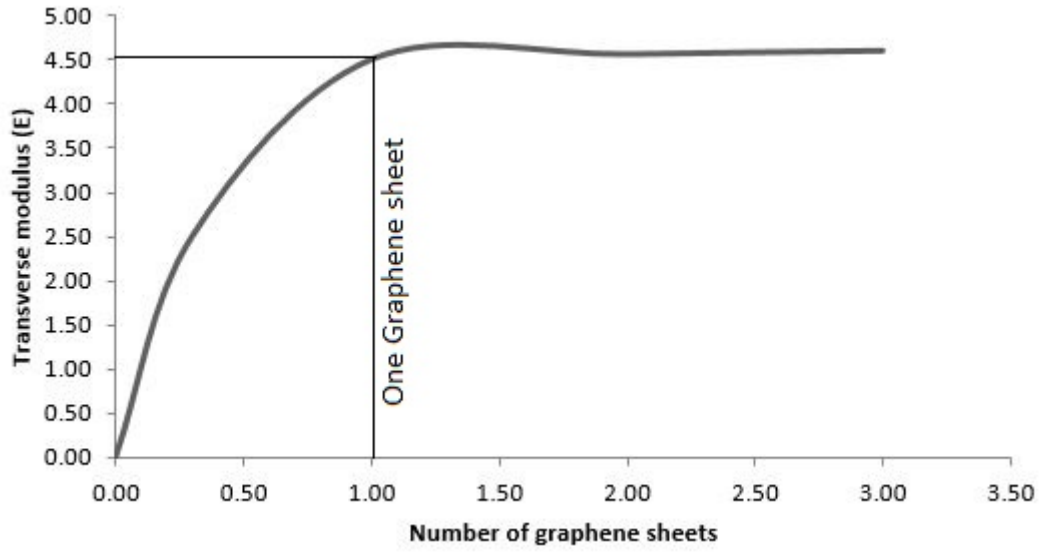


FIGURE 4.15: Transverse modulus of the RVEs versus number of graphene sheets.

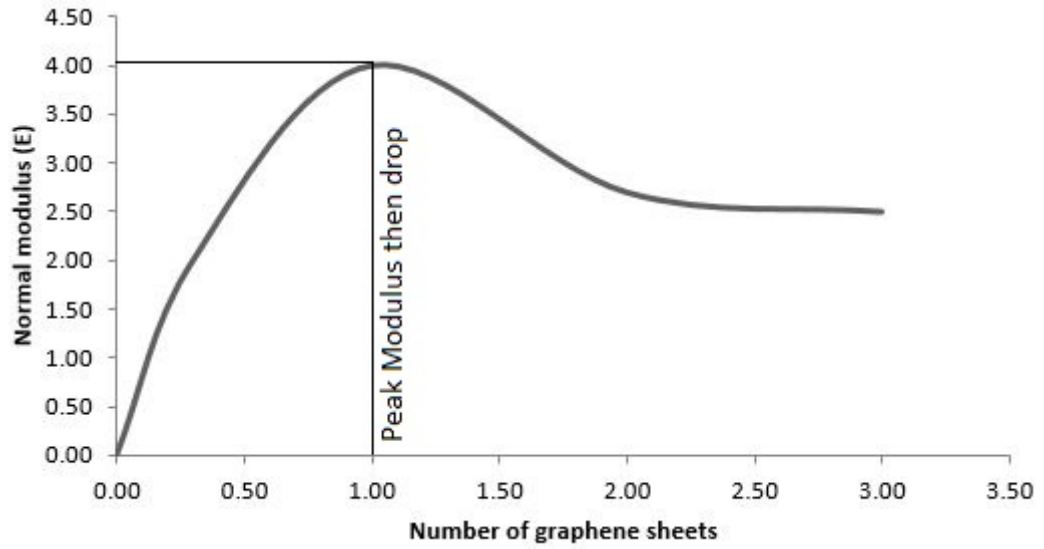


FIGURE 4.16: Normal modulus of the RVEs versus number of graphene sheets.

The normal modulus showed constant increase too with a highest value lower than that of longitudinal and transverse at 4 GPa as shown in Figure 4.16. This therefore showed that 3.7% weight fraction of graphene results in improved mechanical properties for the graphene epoxy nanocomposite. This results showed consistency with literature data [8].

## 4.10 Validation of numerical results with available literature data

### 4.10.1 Mechanical properties

The mean value of the stiffness of numerically tested samples of different weight fractions (1.8%, 3.7% and 5.4%) and the stiffness obtained from literature experimental results [3] were compared. The error of the experimental data is about 5% compared with the molecular dynamics data. This demonstrated that the model of 3.7% weight fraction with two graphene sheet epoxy nanocomposite gave the best improved nanocomposite properties and validated by literature data.

Experimental results for comparison were taken from Dr. King et al. [3] for test specimens constructed of graphene nanocomposite with the same properties as the graphene nanocomposite used in this research. Experimental results were shown in Table 4.4, and indicated a decrease in Elastic modulus modulus with increasing graphene nanoreinforcement weight fractions. Though the model data and the experimental data observed different trends, the model data falls within the standard deviation of the experimental results for all graphene sheet weight fractions, as shown in Figure 4.17.

TABLE 4.4: Experimental results for epoxy composites with varying GNP volume fractions.

Nanoreinforcement weight fraction (%)	Sample size	Tensile Modulus(MPa)	Standard Deviation
0	8	158.9	9.09
0	5	157.5	33.84
0	6	139.6	25.33
1.8	6	155.6	62.13
1.8	7	137.6	10.92
1.8	7	149	21.01
3.7	6	152.6	15.03
3.7	7	133.4	17.84
3.7	6	129.1	13.35
5.4	6	121	16
5.4	6	128	6.27
5.4	5	133	8.19

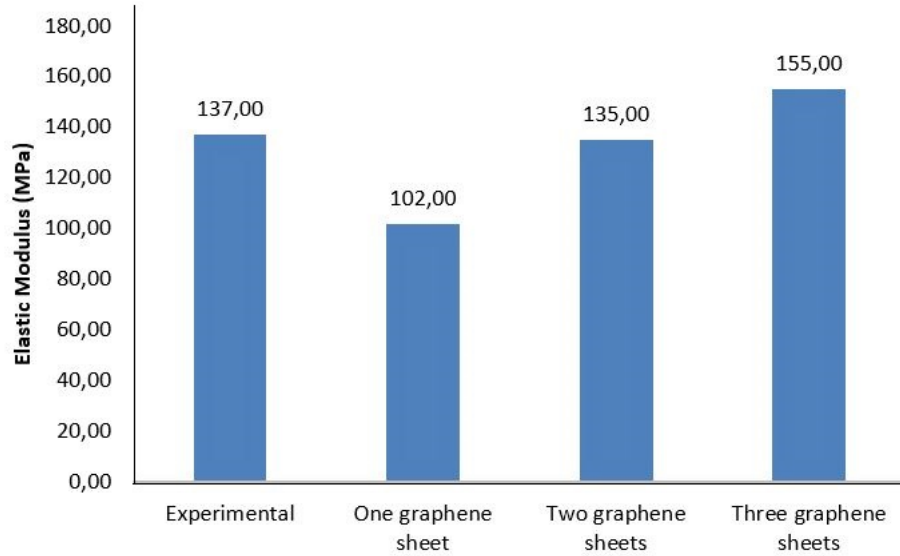


FIGURE 4.17: Comparing numerical results with experimental results of graphene epoxy nanocomposite.[8]

#### 4.10.2 Radial Distribution Function Validation

The radial distribution function for the graphene epoxy models of different weight fractions were analyzed to examine the structural changes after the functionalized graphene sheets incorporation in the system. Figure 4.18 shows molecular dynamics results compared with literature data for RDF of graphene epoxy nanocomposite.

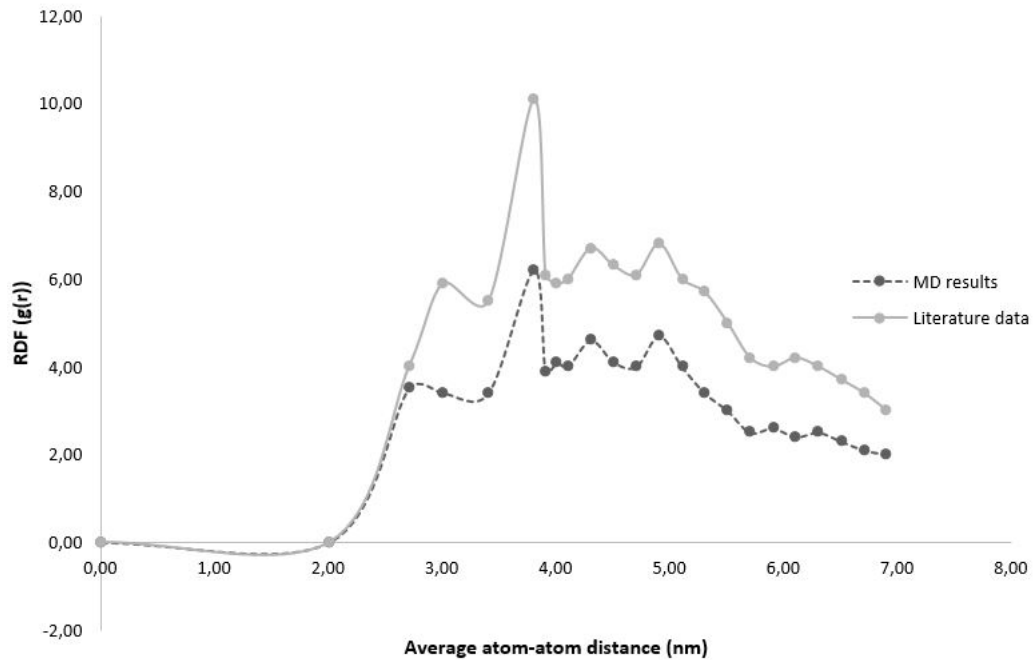


FIGURE 4.18: Molecular dynamics results validation with literature data for RDF of graphene epoxy nanocomposite.

Even though the literature data has the highest peak at  $4.1 \text{ \AA}^0$ , the molecular dynamics results correlates with this literature data with peak at  $3.9 \text{ \AA}^0$ . The difference in peaks may account for the difference in atoms in the systems and different functional groups for the nanoreinforcement. This indicated that both molecular dynamics and literature data models probably yield the same density.

### 4.10.3 Thermal Properties

During the molecular dynamics simulation at NVT, the thermal expansion coefficient for the graphene epoxy nanocomposite of 1.8%, 3.8% and 5.4% weight fraction was obtained. The change in unit cell length with varying temperature was compared with experimentally measured results in Figure 4.19.

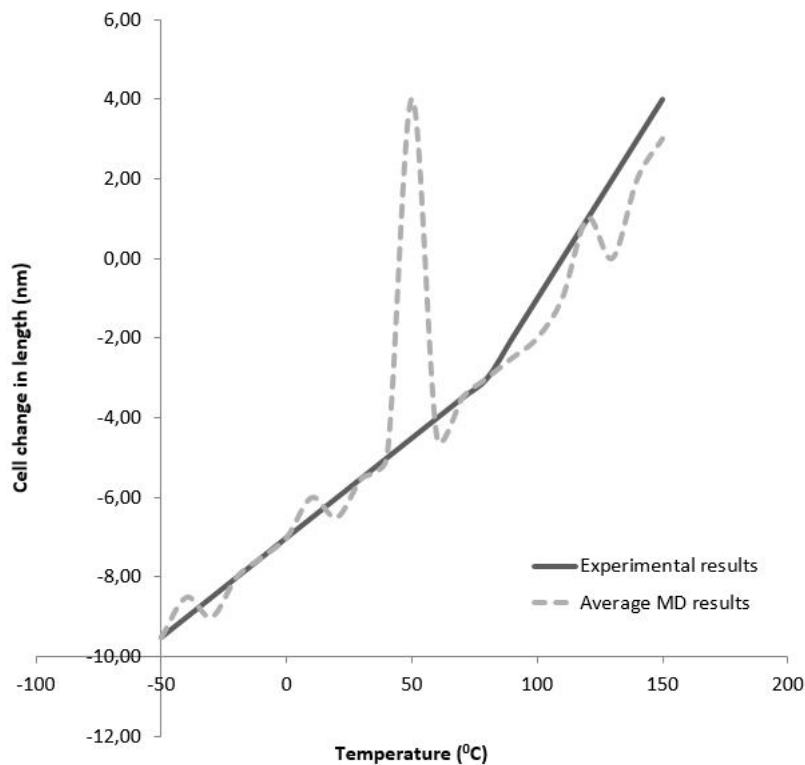


FIGURE 4.19: MD calculation of thermal expansion compared with an experimental data.

The MD calculated data (averaged results for the three weight fractions) is seen to be in very good agreement with the experimental curve. The thermal expansion at higher temperatures plotted show the glass transition temperature, which falls within the experimental range of  $50 - 75^{\circ}\text{C}$  for graphene epoxy nanocomposite.

In Figure 4.20, increasing behavior of the enhancement factor of graphene epoxy nanocomposite is shown as a function of graphene weight fraction. The molecular dynamics results show good agreement with experimental results [82]. This means that the thermal conductivity of graphene nanocomposite changes non linearly with the weight fraction.

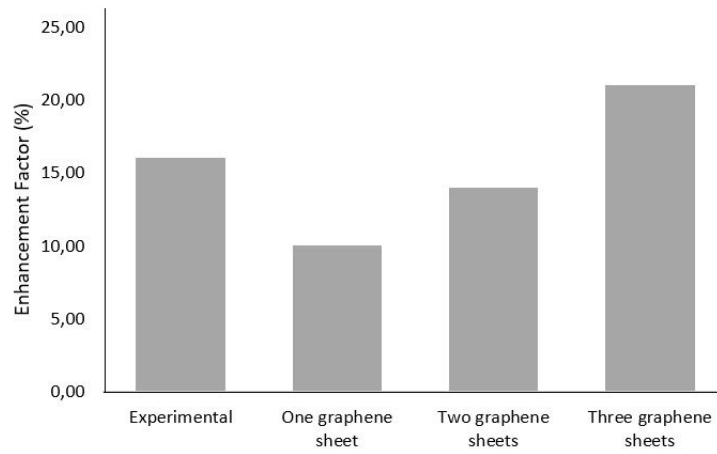


FIGURE 4.20: Comparing the multiscale modeling results with experimental results of graphene epoxy nanocomposite.

The thermal conductivity of the epoxy matrix material was increased by an impressive factor of 10 at the 5.4% weight fraction of graphene loading. This therefore shows that the epoxy-graphene composite preserved all the properties required for industrial thermal applications.

## Chapter 5

# Conclusion

In this study, the interfacial region of the graphene epoxy nanocomposite was characterized using multiscale modelling. Graphene as the nanoreinforcement and epoxy as the matrix. Molecular dynamics was used for the nanoscale analysis and coupled FEA for macroscale analysis to complete the multiscale process. LAMMPS was used in order to probe the effect of graphene on the polymer composite mechanical properties in MD simulations. Optimized LJ potential was used for introducing carbon atoms bonding interactions. The mechanical properties predicted by LAMMPS simulation showed considerable agreement with literature data. MD also determined the influence of crosslinking density and graphene atomic thickness on molecular level mechanical properties. The effect of graphene on the epoxy matrix showed improvement in mechanical properties with the best graphene weight fraction at 3.7%. The molecular dynamics results can be summarized as follows:

- Graphene epoxy nanocomposite with two graphene sheets crosslinking showed improved and expected mechanical properties which consisted of 3.7% weight fraction.
- The Young's modulus and Shear modulus were seen comparatively higher for graphene concentrations of 3.7% to 5.4%. The Young's modulus determined by molecular modelling showed good agreement with literature data.
- For the graphene sheet atoms, the radial distribution function maximum concentration was observed at an approximated pairwise separation of distance  $4 \text{ \AA}$ .
- The radial distribution function for the smaller 1.8% weight concentration was slightly distinguishable. The first peak at  $2.5 \text{ \AA}$  showed average bond distance between the carbon atoms.

- In the MD simulation, the slope of the molecular energy verses strain plots showed progressive deformation in graphene epoxy nanocomposite system. This therefore resulted in an increase in the elastic moduli of the graphene epoxy nanocomposite.
- The 5.4% and 3.7% graphene based systems pairwise bond length were slightly higher than the 1.8% graphene system.
- It was also noticed that during deformation, the maximum normal and shear force were seen to increase with increased graphene aspect ratio.

This gave an insight on load transfer mechanism between the graphene sheet and epoxy matrix. In this work molecular dynamics was coupled with finite element analysis using the Irving-Kirkwood formula. The extracted properties (boundary conditions, Initial conditions and mechanical properties) were used to model the finite element model and analyze the macroscale properties. For the graphene epoxy nanocomposite model, the solution was obtained by minimizing the energy function. Due to computational limitations and modelling complexities, in finite element modelling numbers of perfect particles inside the macroscale RVEs were limited to 100.

In the macroscale scale analysis, the variation of different mechanical properties with addition of different number of graphene sheets was studied. As the normal modulus versus the number of graphene sheets was close to constant, the stiffness of the RVEs in the normal direction was not affected much by the increase of graphene sheets. Transverse and longitudinal modulus showed a jump with the addition of the first graphene sheet and showed constancy with the second and third sheet. The macroscale mechanical properties of the graphene epoxy nanocomposite showed a significant match with literature data.

This multiscale modelling of the graphene epoxy nanocomposite in this work showed that the addition of one graphene sheet improved the interfacial region properties by strengthening the bond between the nanoreinforcement and the matrix. This therefore resulted in improved mechanical properties of the graphene epoxy nanocomposite as a whole. The molecular dynamics mechanical properties found from this research showed that 3.7% weight fraction of graphene showed the best properties for the overall nanocomposite. The addition of one more graphene sheet to the two showed saturation in mechanical properties. The mechanical properties acquired in this research from both molecular dynamics and finite element analysis showed considerable correlation with literature data.

# Appendix A

## An Appendix

### A.1 Appendix A

#### A.1.1 Epoxy LAMMPS input file

Initialization units real

boundary f f f

atom style molecular

log log.simname.txt

read data fname

Dreiding potential information

neighbor 0.4 bin

neighmodify every 10 one 10000

bond style harmonic

bond coeff 1 350 1.53

angle style harmonic

angle coeff 1 60 109.5

dihedral style multi/harmonic

dihedral coeff 1 1.73 -4.49 0.776 6.99 0.0

pair style lj/cut 10.5

pair coeff 1 1 0.112 4.01 10.5

compute csym all centro/atom fcc

compute peratom all pe/atom

Equilibration (Langevin dynamics at 5000 K)

```
velocity all create 5000.0 1231
fix 1 all nve/limit 0.05
fix 2 all langevin 5000.0 5000.0 10.0 904297
thermo style custom step temp
thermo 10000
timestep 1
run 1000000
unfix 1
unfix 2
write restart restart.simname.dreiding1
```

Define Settings

```
compute eng all pe/atom
compute eatoms all reduce sum c eng
```

Minimization

```
dump 1 all cfg 6 dump.comp *.cfg mass type xs ys zs c csym c peratom fx fy fz
```

```
reset timestep 0
fix 1 all nvt temp 500.0 500.0 100.0
thermo 20
thermo style custom step pe lx ly lz press pxx pyy pzz c eatoms
min style cg
minimize 1e-25 1e-25 500000 1000000
```

```
print "All done"
```

### A.1.2 Epoxy Coordinate Datafile

Model for EPOXY

100 atoms  
99 bonds  
98 angles  
97 dihedrals

1 atom types  
1 bond types  
1 angle types  
1 dihedral types

0.0000 158.5000 xlo xhi  
0.0000 158.5000 ylo yhi  
0.0000 100.0000 zlo zhi

Masses

1 14.02

Atoms

1 1 1 5.6240 5.3279 51.6059 2 1 1 7.4995 7.4810 50.2541 3 1 1 8.2322 8.0236 51.2149 4 1  
1 9.6108 9.9075 51.7682 5 1 1 11.5481 11.3690 50.4167 6 1 1 12.9409 13.4562 50.2481 7 1  
1 14.4708 14.8569 50.0868 8 1 1 16.1916 16.4790 50.5665 9 1 1 17.1338 17.6853 51.8189  
10 1 1 19.1109 19.4000 50.3869 11 1 1 20.7544 20.3463 50.8373 12 1 1 21.6557 22.3190  
51.2498 13 1 1 23.7386 23.8051 50.1344 14 1 1 25.4508 24.9976 51.5103 15 1 1 26.7424  
26.8311 50.3130 16 1 1 27.9573 28.1181 51.8644 17 1 1 29.8351 29.8954 51.1650 18 1 1  
31.0827 31.3549 50.0697 19 1 1 32.8854 32.4077 50.0728 20 1 1 34.2461 33.6548 50.2878  
21 1 1 35.6060 35.2545 50.6483 22 1 1 36.9018 36.9064 50.7724 23 1 1 38.6098 38.1669  
50.3762 24 1 1 39.5946 39.8232 51.5392 25 1 1 41.2341 41.7404 51.3856 26 1 1 43.3241  
43.3280 50.5867 27 1 1 44.3094 44.5230 50.6506 28 1 1 46.3318 46.3103 51.1140 29 1 1  
47.2630 47.6806 50.4673 30 1 1 48.9564 48.8846 51.0772 31 1 1 50.9917 50.7552 51.9609  
32 1 1 51.7348 52.0286 50.1029 33 1 1 53.7569 53.6020 51.7143 34 1 1 55.4883 55.4295  
50.8190 35 1 1 56.0003 56.5409 50.4155 36 1 1 57.7193 57.8258 50.1919 37 1 1 59.7475  
59.7485 51.0866 38 1 1 60.8381 61.3323 51.1051 39 1 1 62.9575 62.8928 50.7130 40 1 1  
64.0464 63.8467 51.2456 41 1 1 65.7966 65.7459 50.2511 42 1 1 67.3224 66.5252 50.8289  
43 1 1 68.7314 68.7814 50.7346 44 1 1 70.2449 70.3923 50.4852 45 1 1 71.1296 71.2251  
50.7000 46 1 1 72.7871 73.4275 50.1026 47 1 1 74.5927 74.1629 51.6768 48 1 1 75.6676

76.0022 51.9987 49 1 1 77.3554 77.0471 50.4273 50 1 1 78.8978 78.8337 50.4592 51 1 1  
80.9361 80.6832 51.9242 52 1 1 81.9380 82.4403 50.0117 53 1 1 83.6103 83.8011 50.4660  
54 1 1 85.4325 85.2633 51.6529 55 1 1 86.5735 86.7926 50.6581 56 1 1 87.7235 87.8124  
51.1690 57 1 1 89.8299 89.2905 50.8051 58 1 1 91.3621 91.1147 51.9824 59 1 1 92.2037  
92.8272 51.3517 60 1 1 93.7489 93.9758 50.7982 61 1 1 95.5994 95.8005 50.2101 62 1 1  
97.3214 97.3411 50.7090 63 1 1 98.4301 98.5722 51.4016 64 1 1 100.2425 100.2579 50.7783  
65 1 1 101.4293 101.9563 51.1459 66 1 1 103.3497 102.7763 51.2446 67 1 1 104.5884  
104.9635 50.1718 68 1 1 106.0005 106.0216 50.1803 69 1 1 107.9047 107.8844 50.8780  
70 1 1 109.2817 108.6485 51.2396 71 1 1 110.2606 110.4457 51.6880 72 1 1 111.6962  
111.8039 50.9666 73 1 1 113.3378 113.7985 51.9750 74 1 1 114.6590 114.7369 51.4045  
75 1 1 116.3755 116.9737 51.9446 76 1 1 118.1437 118.3601 50.8038 77 1 1 119.6319  
119.9852 51.1190 78 1 1 121.4336 121.2203 50.9681 79 1 1 122.6390 122.8876 50.3975  
80 1 1 123.8954 124.4922 50.8047 81 1 1 125.6589 125.9013 51.9908 82 1 1 127.1532  
126.6084 50.0722 83 1 1 128.6181 128.5671 51.9239 84 1 1 130.2461 130.1625 51.0466  
85 1 1 131.2599 131.9620 51.0804 86 1 1 132.5303 133.1963 51.0394 87 1 1 134.0590  
134.8900 50.6604 88 1 1 135.7297 135.6139 50.6218 89 1 1 137.2284 137.6520 50.1323  
90 1 1 138.7754 138.7818 51.7601 91 1 1 140.4443 140.7559 51.2066 92 1 1 142.2833  
141.6139 51.9571 93 1 1 143.8486 143.0506 50.9324 94 1 1 144.8257 145.1302 50.4606  
95 1 1 146.5799 146.6032 51.1998 96 1 1 147.9484 147.5354 51.0276 97 1 1 149.4077  
149.1080 50.9198 98 1 1 150.9509 151.0511 51.6108 99 1 1 152.7009 152.8722 50.1044 100  
1 1 153.7197 153.9596 51.9171

#### Bonds

1 1 1 2 2 1 2 3 3 1 3 4 4 1 4 5 5 1 5 6 6 1 6 7 7 1 7 8 8 1 8 9 9 1 9 10 10 1 10 11 11 1 11  
12 12 1 12 13 13 1 13 14 14 1 14 15 15 1 15 16 16 1 16 17 17 1 17 18 18 1 18 19 19 1 19  
20 20 1 20 21 21 1 21 22 22 1 22 23 23 1 23 24 24 1 24 25 25 1 25 26 26 1 26 27 27 1 27  
28 28 1 28 29 29 1 29 30 30 1 30 31 31 1 31 32 32 1 32 33 33 1 33 34 34 1 34 35 35 1 35  
36 36 1 36 37 37 1 37 38 38 1 38 39 39 1 39 40 40 1 40 41 41 1 41 42 42 1 42 43 43 1 43  
44 44 1 44 45 45 1 45 46 46 1 46 47 47 1 47 48 48 1 48 49 49 1 49 50 50 1 50 51 51 1 51  
52 52 1 52 53 53 1 53 54 54 1 54 55 55 1 55 56 56 1 56 57 57 1 57 58 58 1 58 59 59 1 59  
60 60 1 60 61 61 1 61 62 62 1 62 63 63 1 63 64 64 1 64 65 65 1 65 66 66 1 66 67 67 1 67  
68 68 1 68 69 69 1 69 70 70 1 70 71 71 1 71 72 72 1 72 73 73 1 73 74 74 1 74 75 75 1 75  
76 76 1 76 77 77 1 77 78 78 1 78 79 79 1 79 80 80 1 80 81 81 1 81 82 82 1 82 83 83 1 83  
84 84 1 84 85 85 1 85 86 86 1 86 87 87 1 87 88 88 1 88 89 89 1 89 90 90 1 90 91 91 1 91  
92 92 1 92 93 93 1 93 94 94 1 94 95 95 1 95 96 96 1 96 97 97 1 97 98 98 1 98 99 99 1 99  
100

#### Angles

1 1 1 2 3 2 1 2 3 4 3 1 3 4 5 4 1 4 5 6 5 1 5 6 7 6 1 6 7 8 7 1 7 8 9 8 1 8 9 10 9 1 9 10 11  
10 1 10 11 12 11 1 11 12 13 12 1 12 13 14 13 1 13 14 15 14 1 14 15 16 15 1 15 16 17 16  
1 16 17 18 17 1 17 18 19 18 1 18 19 20 19 1 19 20 21 20 1 20 21 22 21 1 21 22 23 22 1  
22 23 24 23 1 23 24 25 24 1 24 25 26 25 1 25 26 27 26 1 26 27 28 27 1 27 28 29 28 1 28  
29 30 29 1 29 30 31 30 1 30 31 32 31 1 31 32 33 32 1 32 33 34 33 1 33 34 35 34 1 34 35  
36 35 1 35 36 37 36 1 36 37 38 37 1 37 38 39 38 1 38 39 40 39 1 39 40 41 40 1 40 41 42  
41 1 41 42 43 42 1 42 43 44 43 1 43 44 45 44 1 44 45 46 45 1 45 46 47 46 1 46 47 48 47  
1 47 48 49 48 1 48 49 50 49 1 49 50 51 50 1 50 51 52 51 1 51 52 53 52 1 52 53 54 53 1  
53 54 55 54 1 54 55 56 55 1 55 56 57 56 1 56 57 58 57 1 57 58 59 58 1 58 59 60 59 1 59  
60 61 60 1 60 61 62 61 1 61 62 63 62 1 62 63 64 63 1 63 64 65 64 1 64 65 66 65 1 65 66  
67 66 1 66 67 68 67 1 67 68 69 68 1 68 69 70 69 1 69 70 71 70 1 70 71 72 71 1 71 72 73  
72 1 72 73 74 73 1 73 74 75 74 1 74 75 76 75 1 75 76 77 76 1 76 77 78 77 1 77 78 79 78  
1 78 79 80 79 1 79 80 81 80 1 80 81 82 81 1 81 82 83 82 1 82 83 84 83 1 83 84 85 84 1  
84 85 86 85 1 85 86 87 86 1 86 87 88 87 1 87 88 89 88 1 88 89 90 89 1 89 90 91 90 1 90  
91 92 91 1 91 92 93 92 1 92 93 94 93 1 93 94 95 94 1 94 95 96 95 1 95 96 97 96 1 96 97  
98 97 1 97 98 99 98 1 98 99 100

#### Dihedrals

1 1 1 2 3 4 2 1 2 3 4 5 3 1 3 4 5 6 4 1 4 5 6 7 5 1 5 6 7 8 6 1 6 7 8 9 7 1 7 8 9 10 8 1 8 9  
10 11 9 1 9 10 11 12 10 1 10 11 12 13 11 1 11 12 13 14 12 1 12 13 14 15 13 1 13 14 15  
16 14 1 14 15 16 17 15 1 15 16 17 18 16 1 16 17 18 19 17 1 17 18 19 20 18 1 18 19 20 21  
19 1 19 20 21 22 20 1 20 21 22 23 21 1 21 22 23 24 22 1 22 23 24 25 23 1 23 24 25 26 24  
1 24 25 26 27 25 1 25 26 27 28 26 1 26 27 28 29 27 1 27 28 29 30 28 1 28 29 30 31 29 1  
29 30 31 32 30 1 30 31 32 33 31 1 31 32 33 34 32 1 32 33 34 35 33 1 33 34 35 36 34 1 34  
35 36 37 35 1 35 36 37 38 36 1 36 37 38 39 37 1 37 38 39 40 38 1 38 39 40 41 39 1 39 40  
41 42 40 1 40 41 42 43 41 1 41 42 43 44 42 1 42 43 44 45 43 1 43 44 45 46 44 1 44 45 46  
47 45 1 45 46 47 48 46 1 46 47 48 49 47 1 47 48 49 50 48 1 48 49 50 51 49 1 49 50 51 52  
50 1 50 51 52 53 51 1 51 52 53 54 52 1 52 53 54 55 53 1 53 54 55 56 54 1 54 55 56 57 55  
1 55 56 57 58 56 1 56 57 58 59 57 1 57 58 59 60 58 1 58 59 60 61 59 1 59 60 61 62 60 1  
60 61 62 63 61 1 61 62 63 64 62 1 62 63 64 65 63 1 63 64 65 66 64 1 64 65 66 67 65 1 65  
66 67 68 66 1 66 67 68 69 67 1 67 68 69 70 68 1 68 69 70 71 69 1 69 70 71 72 70 1 70 71  
72 73 71 1 71 72 73 74 72 1 72 73 74 75 73 1 73 74 75 76 74 1 74 75 76 77 75 1 75 76 77  
78 76 1 76 77 78 79 77 1 77 78 79 80 78 1 78 79 80 81 79 1 79 80 81 82 80 1 80 81 82 83  
81 1 81 82 83 84 82 1 82 83 84 85 83 1 83 84 85 86 84 1 84 85 86 87 85 1 85 86 87 88 86  
1 86 87 88 89 87 1 87 88 89 90 88 1 88 89 90 91 89 1 89 90 91 92 90 1 90 91 92 93 91 1  
91 92 93 94 92 1 92 93 94 95 93 1 93 94 95 96 94 1 94 95 96 97 95 1 95 96 97 98 96 1 96  
97 98 99 97 1 97 98 99 100

## A.2 Appendix B

### A.2.1 Graphene sheet LAMMPS input file

```
dimension 3
boundary p p p
units metal

atom style charge
read data data.charge

region up block -9.838 -7.8704 INF INF INF INF units box
region down block 0 1.9676 INF INF INF INF units box

pair style airebo 3.0 1 1
pair coeff * * CH.airebo C

replicate 1 1 5

neighbor 4.0 bin
neigh modify delay 0 every 1 check yes

timestep 0.00005

velocity all create 300 1234567 mom yes rot yes dist gaussian units box

fix thermostat all nvt temp 300.0 300.0 0.1

compute alltemp all temp
thermo style custom step atoms temp press pe ke etotal xlo xhi ylo yhi zlo zhi vol en-
thalpy
thermo modify temp alltemp lost warn
```

```

compute ke all ke/atom
variable temp atom c ke/(1.5*1.0)/8.617343*100000.0
fix temp profile all ave/spatial 1 100000 100000 x -9.838 1.9676 v temp file
temp6.profile units box
fix temp atom all ave/atom 1 100000 100000 v temp
compute up temp all temp/region up
compute down temp all temp/region down
variable delta t equal c down temp-c up temp fix delta t all ave/time 1 100000 100000
v delta t file delta t6.dat

```

```

dump 1 all xyz 100000 dump6.coord.*
dump 2 all custom 100000 dump6.vel.* id type mass vx vy vz fx fy fz f temp atom
restart 400000 restart6.mwnt.*
thermo 1000
run 400000

```

```

unfix thermostat
fix ensemble all nve
fix heat swap all thermal/conductivity 40 x 10
fix e exchange all ave/time 40 2500 100000 f heat swap file e exchange6.dat

run 2000000

```

## A.2.2 Functionalized graphene sheet LAMMPS input file

Requirements: To run this system at constant pressure, it might help to compile LAMMPS with the optional RIGID package, and use "fix rigid" on the carbon. (Optional.) The use of fix rigid is controversial. This method is demonstrated below.

————— Initialization Section —————

```
include system.in.init
```

---

- Atom Definition Section -

```
read data system.data
```

---

- Settings Section -

```
include system.in.settings
```

---

- Run Section -

Only the graphene atoms are immobile.  
group mobile subtract all graphene

Unfortunately you can not use the LAMMPS "minimize" command on this system because there is no way to immobilize the carbon graphene atoms during minimization. Instead, we can use langevin dynamics with a large damping parameter and a small timestep.

```
print "----- beginning minimization (using fix langevin) -----"
```

```
timestep 0.1  
fix fxlan mobile langevin 1.0 1.0 100.0 48279  
fix fxnve mobile nve ;- needed by fix langevin (see lammmps documentation)  
thermo 100  
run 2500
```

```
unfix fxlan  
unfix fxnve
```

- simulation protocol -

```
print "----- beginning simulation (using fix nvt) -----"
```

timestep 0.5

dump 1 all custom 1000 traj npt.lammpstrj id mol type x y z ix iy iz

thermo style custom step temp pe etotal press vol epair ebond eangle edihed

thermo 1000 time interval for printing out "thermo" data

————— - NPT —————

Set temp=300K, pressure=100bar, and equilibrate volume only in the z direction

fix fxMoveStuff mobile npt temp 300 300 100 z 100 100 1000.0 dilate mobile

——— CONTROVERSIAL (see below): ——

fix Ffreezestuff Cgraphene rigid/npt single temp 300 300 100 z 100 100 1000.0 force \*

off off off torque \*

off off off dilate mobile

– Alternate npt rigid method –

I'm not sure which way is more correct, however

this also seems to behave in a reasonable-looking way:

fix Ffreezestuff Cgraphene rigid single force \* off off off torque \* off off off

The use of either "fix rigid" or "fix rigid/npt" to immobilize

an object is somewhat controversial. Feel free to omit it.

(Neither Trung or Steve Plimpton use rigid or rigid/npt for immobilizing molecules, but I noticed that at NPT, it does a better job of maintaining the correct volume. However "fix rigid" has changed since then (2011), so this may no longer be true. Please use this example with caution.)

—————

IMPORTANT for NPT: You must use "neigh modify" to turn off calculation of the forces between immobilized atoms.

neigh modify exclude group Cgraphene Cgraphene

The next two lines recalculate the temperature using only the mobile degrees of freedom:

```
compute tempMobile mobile temp
compute pressMobile all pressure tempMobile
```

```
thermo style custom step c tempMobile c pressMobile temp press vol
```

```
fix modify fxMoveStuff temp tempMobile
```

```
run 100000
```

### A.2.3 Functionalized graphene sheet coordinate LAMMPS file

This file contains a unit cell for building graphene

The 2AtomCellAlignX "molecule" defined below is a minimal unit cell for any hexagonal tessellation in 2-dimensions. (See "graphene unit cell.jpg")

The distance between nearest-neighbor carbon atoms (ie the length of a carbon-carbon bond) is equal to "d" which I set to 1.42 Angstroms.

$L = \text{length of each hexagon} = 2*d = 2.84 \text{ Angstroms}$

$W = \text{width of each hexagon} = 2*d*\sqrt{3}/2 = 2.4595121467478056 \text{ Angstroms}$

$w = \text{width of hexagon rows} = 1.5*l = 2.13 \text{ Angstroms}$

Consequently, the Lattice-cell vectors for single-layer graphene are:

(2.4595121467478, 0, 0) (aligned with X axis)

(1.2297560733739, 2.13, 0) ( $2.13 = 1.5*d$ )

So, to build a sheet of graphite, you could use:

```
sheet = new Graphene/2AtomCellAlignX [10].move(2.4595121467478,0,0)
```

```
[10].move(1.2297560733739,2.13,0)
```

Graphene

```
2AtomCellAlignX
```

```
atomID molID atomType charge x y z
```

```
write("Data Atoms") atom : C1mol:... @atom:../C 0.0 -0.61487803668695 -0.355 0.0
atom : C2mol:... @atom:../C 0.0 0.61487803668695 0.355 0.0
```

Now define properties of the Carbon graphene atom

```
write once("In Init")
pair style hybrid lj/charmm/coul/charmm 9.0 10.0
```

```
write once("Data Masses")
@atom:C 12.0
```

```
write once("In Settings")
i j epsilon sigma
pair coeff @atom:C @atom:C lj/charmm/coul/charmm 0.068443 3.407
```

These Lennard-Jones parameters come from  
R. Saito, R. Matsuo, T. Kimura, G. Dresselhaus, M.S. Dresselhaus,  
Chem Phys Lett, 348:187 (2001)

Define a group consisting of only carbon atoms in graphene molecules  
group Cgraphene type atom:C

Notice that the two atoms in the unit-cell above lie in the XY plane.  
(Their z-coordinate is zero). It's also useful to have a version of  
this object which lies in the XZ plan. So we define this below:

```
2AtomCellAlignXZ = 2AtomCellAlignX.rot(90,1,0,0)
```

Graphene

## A.3 Appendix C

### A.3.1 Graphene epoxy nanocomposite system LAMMPS input file

Initialization

```
units real
dimension 3
boundary p p p
atom style molecular
```

PCFF potential information (Class 2 Force-field)

```
neighbor 5.0 bin
neigh-modify every 1 delay 1
bond style class2 Define bond style
angle style class2 Define angle style
dihedral style class2 Define dihedral style
improper style class2 Define improper style
pair style lj/class2 10.0
```

```
read_data Model1Importgeometricaldata
```

Geometrical information

```
group polymer type 2 4 Define polymer group
group graphene type 1 Define graphene group
```

Output thermodynamics parameters

```
thermo style custom step temp etotal vol ke
thermo 1000
thermo modify lost warn
```

velocity polymer create 300 5812775 dist gaussian units box  
velocity graphene create 300 5812778 dist gaussian units box

#### Calculate Temperature Profile

compute ke all ke/atom

variable temp atom c ke/(1.5\*1.0\*0.0019872041)

fix temp polymer profile polymer ave/spatial 10 10000 100000 z lower 0.05

v temp file temp polymer 1.profile units reduced

fix temp graphene profile graphene ave/spatial 10 10000 100000 z lower 0.5

v temp file temp graphene 1.profile units reduced

#### NVT Equilibration

fix temp all temp/berendsen 300 300 5

fix nve all nve

timestep 0.25

run 500000

unfix temp

#### NEMD Calculation

fix heat swap all thermal/conductivity 200 z 20

fix e exchange all ave/time 200 500 100000 f heat<sub>s</sub>wapfileexchange1.dat

run 5000000

### A.3.2 Graphene epoxy nanocomposite interfacial region LAMMPS input file

————— Initialization Section —————

include system.in.init

————— Atom Definition Section —————

read data system.data

————— Settings Section —————

include system.in.settings

————— Run Section —————

Optional: Improve efficiency by omitting the calculation of interactions between immobile atoms. (Note: This is not optional under NPT conditions.)  
neigh modify exclude group graphene epoxy united atoms

Only the nanoreinforcement atoms are immobile.  
group mobile subtract all C

– minimization protocol –

print "———— beginning minimization (using fix langevin) ———"

timestep 0.1

fix fxlan mobile langevin 1.0 1.0 100.0 48279

```
fix fxnve mobile nve ;- needed by fix langevin (see lammmps documentation)
thermo 100
run 2500
```

```
unfix fxlan
unfix fxnve
```

– simulation protocol –

```
print "———— beginning simulation (using fix nvt) ————"
```

```
timestep 1.0
dump 1 all custom 500 traj nvt.lammpstrj id mol type x y z ix iy iz
```

```
thermo style custom step temp pe etotal press vol epair ebond eangle edihed
thermo 500 time interval for printing out "thermo" data
```

Integrate the equations of motion:

```
fix fxMoveStuff mobile nvt temp 300.0 300.0 100.0
```

The next two lines recalculate the temperature  
using only the mobile degrees of freedom:

```
compute tempMobile mobile temp
fix modify fxMoveStuff temp tempMobile
```

```
restart 5000000 restart nvt
run 10000000
```

## A.4 Appendix D

```
function cube_plot(origin,X,Y,Z,color)
% CUBE_PLOT plots a cube with dimension of X, Y, Z.
%
% INPUTS:
% origin = set origin point for the cube in the form of [x,y,z].
% X      = cube length along x direction.
% Y      = cube length along y direction.
% Z      = cube length along z direction.
% color  = STRING, the color patched for the cube.
%
% List of colors
%
% b blue
% g green
% r red
% c cyan
% m magenta
% y yellow
% k black
% w white
%
% OUPUTS:
% Plot a figure in the form of cubics.
%
% EXAMPLES
% cube_plot(2,3,4,'red')
%
% -----Code Starts
Here----- %
% Define the vertexes of the unit cubic
ver = [1 1 0;
       0 1 0;
       0 1 1;
       1 1 1;
       0 0 1;
       1 0 1;
       1 0 0;
       0 0 0];
% Define the faces of the unit cubic
fac = [1 2 3 4;
       4 3 5 6;
       6 7 8 5;
       1 2 8 7;
       6 7 1 4;
       2 3 5 8];
cube = [ver(:,1)*X+origin(1),ver(:,2)*Y+origin(2),ver(:,3)
        *Z+origin(3)];
patch('Faces',fac,'Vertices',cube,'FaceColor',color);
end
```

FIGURE A.1: Matlab script for the Macroscale RVE of the nanocomposite system

## A.5 Appendix E

```
clf;
figure(1);
% Use hold on and hold off to plot multiple cubes
hold on;
% Call the function to plot a cube with dimension of X, Y, Z,
at point [x,y,z].
cube_plot([1,1,1],1,1,1,'r');
% Figure configurations
% Define the range of x-axis, y-axis, and z-axis in form of
% [xmin,xmax,ymin,ymax,zmin,zmax].
% axis([0,1,0,1,0,1]);
% Set the axis with equal unit.
axis equal;
% Show grids on the plot
grid on;
% Set the lable and the font size
xlabel('X','FontSize',18);
ylabel('Y','FontSize',18);
zlabel('Z','FontSize',18);
% Control the ticks on the axes
h = gca; % Get the handle of the figure
% h.XTick = 0:0.5:1;
% h.YTick = 0:0.5:1;
% h.ZTick = 0:0.5:1;
% Set the color as transparent
material metal
alpha('color');
alphamap('rampup');
% Set the view point
view(30,30);
hold off;
% plot the figure in the form of eps with 600 ppi named
'filename'
% print(gcf,'-depsc2','-r600','filename.eps')
```

FIGURE A.2: Matlab script for the Macroscale RVE of the nanocomposite system

# Bibliography

- [1] Zénó Farkas. Multi-scale modelling of Li-ion batteries ECMI, 2015. URL <https://ecmiindmath.org/2015/03/16/multi-scale-modelling-of-li-ion-batteries/>.
- [2] Charles Chikwendu Okpala. Nanocomposites An Overview. *International Journal of Engineering Research and Development*, 8(11):2278–67, 2013. URL <http://www.ijerd.com/paper/vol8-issue11/C08111723.pdf>.
- [3] Dimitrios G Papageorgiou, Ian A Kinloch, and Robert J Young. Mechanical properties of graphene and graphene-based nanocomposites. *Progress in Materials Science*, 90:75–127, 2017.
- [4] N Saba, M Jawaid, MT Paridah, and Othman Alothman. Physical, structural and thermomechanical properties of nano oil palm empty fruit bunch filler based epoxy nanocomposites. *Industrial Crops and Products*, 108:840–843, 2017.
- [5] Ke Chu, Xiao-hu Wang, Yu-biao Li, Da-jian Huang, Zhong-rong Geng, Xi-long Zhao, Hong Liu, and Hu Zhang. Thermal properties of graphene/metal composites with aligned graphene. *Materials & Design*, 2017.
- [6] Dong Sun, Charles Divin, Claire Berger, Walt A. de Heer, Phillip N. First, and Theodore B. Norris. Spectroscopic Measurement of Interlayer Screening in Multilayer Epitaxial Graphene. *Physical Review Letters*, 104(13):136802, apr 2015. ISSN 0031-9007. doi: 10.1103/PhysRevLett.104.136802. URL <http://link.aps.org/doi/10.1103/PhysRevLett.104.136802>.
- [7] Olga Naboka, Chae-Ho Yim, and Yaser Abu-Lebdeh. Graphene/na carboxymethyl cellulose composite for li-ion batteries prepared by enhanced liquid exfoliation. *Materials Science and Engineering: B*, 213:41–50, 2016.
- [8] Yuka Takagi, Shiro Yamazaki, Kan Nakatsuji, and Hiroyuki Hirayama. Size, shape, and number density of deposits in the graphene solution liquid droplet method. *Materials Today Communications*, 13:65–71, 2017.

- [9] Ephraim M Kiarii, Krishna K Govender, Patrick G Ndung'u, and Penny P Goven-der. Computational condensed matter. 2017.
- [10] Chapter 8 Literature Review of Epoxy Toughening. URL <https://rjyhxfnvtheses.lib.vt.edu/theses/available/etd-32398-61326/unrestricted/8-9.pdf>.
- [11] Yun Chen, Donghai Zhang, Xiaofeng Wu, Haosheng Wang, Chong Zhang, Wei Yang, and Yunfa Chen. Epoxy/ $\alpha$ -alumina nanocomposite with high electrical insulation performance. *Progress in Natural Science: Materials International*, 27(5):574–581, 2017.
- [12] Paul Preuss. Atom by Atom, Bond by Bond, a Chemical Reaction Caught in the Act — Berkeley Lab, 2017. URL <http://newscenter.lbl.gov/2013/05/30/atom-by-atom/>.
- [13] Nikolas Provatas, Michael Greenwood, Badrinarayan Athreya, Nigel Goldenfeld, and Jonathan Dantzig. Multiscale modeling of solidification: phase-field methods to adaptive mesh refinement. *International Journal of Modern Physics B*, 19(31):4525–4565, 2015.
- [14] Yan-Jun Wan, Li-Xiu Gong, Long-Cheng Tang, Lian-Bin Wu, and Jian-Xiong Jiang. Mechanical properties of epoxy composites filled with silane-functionalized graphene oxide. *Composites Part A: Applied Science and Manufacturing*, 64:79–89, 2014.
- [15] Q Yuan and RDK Misra. Impact fracture behavior of clay-reinforced polypropylene nanocomposites. *Polymer*, 47(12):4421–4433, 2014.
- [16] 7 Advantages and Disadvantages of Experimental Research — Flow Psychology. URL <http://flowpsychology.com/7-advantages-and-disadvantages-of-experimental-research/>.
- [17] Graphene - What Is It? Graphenea. URL <https://www.graphenea.com/pages/graphene-#}.WMpMZ1WGOUk>.
- [18] Sung-Chiun Shiu and Jia-Lin Tsai. Characterizing thermal and mechanical properties of graphene/epoxy nanocomposites. *Composites Part B*, 56:691–697, 2014. doi: 10.1016/j.compositesb.2013.09.007. URL [http://ac.els-cdn.com/S1359836813005209/1-s2.0-S1359836813005209-main.pdf?\\_tid=6cdcdfdc-0a25-11e7-98a2-00000aab0f02&acdnat=1489654331{}\\_c117d53110239d49e435c3cdc03bc959](http://ac.els-cdn.com/S1359836813005209/1-s2.0-S1359836813005209-main.pdf?_tid=6cdcdfdc-0a25-11e7-98a2-00000aab0f02&acdnat=1489654331{}_c117d53110239d49e435c3cdc03bc959).

- [19] Byung Min Yoo, Hye Jin Shin, Hee Wook Yoon, and Ho Bum Park. Graphene and graphene oxide and their uses in barrier polymers. *Journal of Applied Polymer Science*, 131(1):n/a–n/a, jan 2014. ISSN 00218995. doi: 10.1002/app.39628. URL <http://doi.wiley.com/10.1002/app.39628>.
- [20] Dierk Raabe, Matthias Scheffler, Kurt Kremer, Walter Thiel, Jörg Neugebauer, and Martin Jansen. Multi-Scale Modeling in Materials Science and Engineering. 2014. URL <https://www.mpg.de/36458/cpt01{ }MultiscaleModeling-basetext.pdf>.
- [21] Olayinka Oluremi and Ogunro Ii. A Computational Study of the functionalization of Single-Walled Carbon Nanotubes with Macromolecules. 2013. URL <http://digitalcommons.auctr.edu/dissertations>.
- [22] Moorfield Nanotechnology Limited. Compact, turn-key and scalable CVD systems for high-throughput graphene and carbon nanotube synthesis. URL <http://moorfield.co.uk/nanocvd/>.
- [23] ) N. Hu M. C. Wang, Z. B. Lai, D. Galpaya, C. Yan. Atomistic simulation of surface functionalization on the interfacial properties of graphene-polymer nanocomposites. 12, 2014. URL <http://eprints.qut.edu.au/69118/8/69118p.pdf>.
- [24] Gina Peschel. Carbon-Carbon bonds: Hybridization. 2011. URL <http://www.physik.fu-berlin.de/einrichtungen/ag/ag-reich/lehre/Archiv/ss2011/docs/Gina{ }Peschel-Presentation.pdf>.
- [25] Leif Gustafsson and Mikael Sternad. Bringing consistency to simulation of population models Poisson Simulation as a bridge between micro and macro simulation. *Mathematical Biosciences*, 209(2):361–385, oct 2015. ISSN 00255564. doi: 10.1016/j.mbs.2007.02.004. URL <http://linkinghub.elsevier.com/retrieve/pii/S002555640700034X>.
- [26] Paul Sherwood, Bernard R Brooks, and Mark SP Sansom. Multiscale methods for macromolecular simulations. *Current opinion in structural biology*, 18(5):630–640, 2015.
- [27] Fu Chu-Chun, Jacques Dalla Torre, François Willaime, Jean-Louis Bocquet, and Alain Barbu. Multiscale modelling of defect kinetics in irradiated iron. *Nature materials*, 4(1):68, 2015.
- [28] E Weinan, Bjorn Engquist, and Zhongyi Huang. Heterogeneous multiscale method: a general methodology for multiscale modeling. *Physical Review B*, 67(9):092101, 2013.

- [29] D. Savastru, S. Miclos, R. Savastru, and I.I. Lancranjan. Study of thermo-mechanical characteristics of polymer composite materials with embedded optical fibre. *Composite Structures*, 2017. ISSN 0263-8223. doi: <https://doi.org/10.1016/j.compstruct.2017.09.042>. URL <http://www.sciencedirect.com/science/article/pii/S0263822316328100>.
- [30] Guangzhou Hu, Zhentao Bian, Ru Xue, Wenyan Huang, and Sridhar Komarineni. Polymer-coal composite as a novel plastic material. *Materials Letters*, 197 (Supplement C):31 – 34, 2017. ISSN 0167-577X. doi: <https://doi.org/10.1016/j.matlet.2017.03.148>. URL <http://www.sciencedirect.com/science/article/pii/S0167577X17304949>.
- [31] L.S. Schadler, L.C. Brinson and W.G. Sawyer. Polymer Nanocomposites: A Small Part of the Story. 13, 2015. URL <http://nersp.nerdc.ufl.edu/~wsawyer/nano2007.PDF>.
- [32] Pedro Henrique Cury Camargo, Kestur Gundappa Satyanarayana, and Fernando Wypych. Nanocomposites: synthesis, structure, properties and new application opportunities. *Materials Research*, 12(1):1–39, mar 2016. ISSN 1516-1439. doi: 10.1590/S1516-14392009000100002. URL [http://www.scielo.br/scielo.php?script=sci\\_arttext&pid=S1516-14392009000100002&lng=en&nrm=iso&tlng=en](http://www.scielo.br/scielo.php?script=sci_arttext&pid=S1516-14392009000100002&lng=en&nrm=iso&tlng=en).
- [33] Nastaran Nazeran and Jafarsadegh Moghaddas. Synthesis and characterization of silica aerogel reinforced rigid polyurethane foam for thermal insulation application. *Journal of Non-Crystalline Solids*, 461:1–11, 2017.
- [34] Charles Chikwendu Okpala. The benefits and applications of nanocomposites. *Int J Adv Engg Tech/Vol. V/Issue IV/Oct.-Dec*, 12:18, 2014.
- [35] Nadeesh Madusanka, Sai G Shivareddy, Mark D Eddleston, Pritesh Hiralal, Rachel A Oliver, and Gehan AJ Amaratunga. Dielectric behaviour of montmorillonite/cyanoethylated cellulose nanocomposites. *Carbohydrate Polymers*, 2017.
- [36] S Anandhan and Han Sup Lee. Influence of organically modified clay mineral on domain structure and properties of segmented thermoplastic polyurethane elastomer. *Journal of Elastomers & Plastics*, 46(3):217–232, 2014.
- [37] K Rahul, Madhukar H Shetty, Karthik Madhyastha, Kenneth Paul DSouza, Loyd DSouza, et al. Processing and characterisation of banana fiber reinforced polymer nano composite. *Nanoscience and Nanotechnology*, 7(2):34–37, 2016.

- [38] Poh Choon Ooi, Muhammad Aniq Shazni Mohammad Haniff, MF Mohd Razip Wee, Chang Fu Dee, Boon Tong Goh, Mohd Ambri Mohamed, and Burhanuddin Yeop Majlis. Reduced graphene oxide preparation and its applications in solution-processed write-once-read-many-times graphene-based memory device. *Carbon*, 124:547–554, 2017.
- [39] Long-Cheng Tang, Yan-Jun Wan, Dong Yan, Yong-Bing Pei, Li Zhao, Yi-Bao Li, Lian-Bin Wu, Jian-Xiong Jiang, and Guo-Qiao Lai. The effect of graphene dispersion on the mechanical properties of graphene/epoxy composites. *Carbon*, 60:16–27, 2013.
- [40] O Richard Alonge, Mahyuddin B Ramli, and T John Lawalson. Properties of hybrid cementitious composite with metakaolin, nanosilica and epoxy. *Construction and Building Materials*, 155:740–750, 2017.
- [41] Ahmed Akelah, Ahmed Rehab, Mohamed Abdelwahab, and Mohamed A Betiha. Synthesis and thermal properties of nanocomposites based on exfoliated organoclay polystyrene and poly (methylmethacrylate). *Nanocomposites*, pages 1–10, 2017.
- [42] S Anandhan and S Bandyopadhyay. Polymer Nanocomposites: From Synthesis to Applications. 2014. URL <http://cdn.intechweb.org/pdfs/17184.pdf>.
- [43] László Lendvai, Ákos Kmetty, and József Karger-Kocsis. Preparation and properties of thermoplastic starch/bentonite nanocomposites. In *Materials Science Forum*, volume 885, pages 129–134. Trans Tech Publications, 2017.
- [44] Farzana Hussain, Mehdi Hojjati, and Russell E Gorga. Polymer-matrix Nanocomposites, Processing, Manufacturing, and Application: An Overview. *Journal of COMPOSITE MATERIALS*, 40(17), 2013. doi: 10.1177/0021998306067321. URL <http://jcm.sagepub.com>.
- [45] Kesong Hu, Dhaval D Kulkarni, Ikjun Choi, and Vladimir V Tsukruk. Graphene-polymer nanocomposites for structural and functional applications. *Progress in Polymer Science*, 39(11):1934–1972, 2014.
- [46] Jeffrey R Potts, Daniel R Dreyer, Christopher W Bielawski, and Rodney S Ruoff. Graphene-based polymer nanocomposites. *Polymer*, 52(1):5–25, 2011.
- [47] Jaemin Cha, Gwang Hoon Jun, Jong Kyoo Park, Jung Cheol Kim, Ho Jin Ryu, and Soon H Hong. Improvement of modulus, strength and fracture toughness of cnt/epoxy nanocomposites through the functionalization of carbon nanotubes. *Composites Part B: Engineering*, 129:169–179, 2017.

## Bibliography

- [48] Refik Arat and Nurseli Uyanık. Study of the morphological and thermal properties of polystyrene nanocomposites based on modified halloysite nanotubes with styrene-maleic anhydride copolymers. *Materials Today Communications*, 13:255–262, 2017.
- [49] Hyuk-Gi Lee, Gue-Hyun Kim, and Chang-Sik Ha. Polyimide/amine-functionalized cellulose nanocrystal nanocomposite films. *Materials Today Communications*, 13: 275–281, 2017.
- [50] Linda Schadler. Nanocomposites: model interfaces. *Nature materials*, 6(4):257–258, 2015.
- [51] Evangelos Manias. Nanocomposites: Stiffer by design. *Nature Materials*, 6(1): 9–11, 2013.
- [52] Sung-Chiun Shiu and Jia-Lin Tsai. Characterizing thermal and mechanical properties of graphene/epoxy nanocomposites. *Composites Part B: Engineering*, 56: 691–697, 2014.
- [53] Mauricio Terrones, Olga Martín, María González, Javier Pozuelo, Berna Serrano, Juan C Cabanelas, Sofía M Vega-Díaz, and Juan Baselga. Interphases in graphene polymer-based nanocomposites: Achievements and challenges. *Advanced Materials*, 23(44):5302–5310, 2011.
- [54] Xiaoqing Zhang, Xinyu Fan, Chun Yan, Hongzhou Li, Yingdan Zhu, Xiaotuo Li, and Liping Yu. Interfacial microstructure and properties of carbon fiber composites modified with graphene oxide. 2012.
- [55] Hiroaki Miyagawa, Kit H Foo, Isaac M Daniel, and Lawrence T Drzal. Mechanical properties and failure surface morphology of amine-cured epoxy/clay nanocomposites. *Journal of applied polymer science*, 96(2):281–287, 2015.
- [56] SC Tjong and SP Bao. Fracture toughness of high density polyethylene/sebs-gamma/montmorillonite nanocomposites. *Composites science and technology*, 67(2): 314–323, 2014.
- [57] Long-Cheng Tang, Yan-Jun Wan, Dong Yan, Yong-Bing Pei, Li Zhao, Yi-Bao Li, Lian-Bin Wu, Jian-Xiong Jiang, and Guo-Qiao Lai. The effect of graphene dispersion on the mechanical properties of graphene/epoxy composites. *Carbon*, 60:16–27, 2013.
- [58] Tie Lan and Thomas J Pinnavaia. Clay-reinforced epoxy nanocomposites. *Chemistry of materials*, 6(12):2216–2219, 2013.

- [59] Xianhang Sui, Jie Shi, Hongwei Yao, Zhiwei Xu, Lei Chen, Xiaojie Li, Meijun Ma, Liyun Kuang, Hongjun Fu, and Hui Deng. Interfacial and fatigue-resistant synergetic enhancement of carbon fiber/epoxy hierarchical composites via an electrophoresis deposited carbon nanotube-toughened transition layer. *Composites Part A: Applied Science and Manufacturing*, 92:134–144, 2017.
- [60] Kyriaki Kalaitzidou, Hiroyuki Fukushima, and Lawrence T Drzal. A new compounding method for exfoliated graphite–polypropylene nanocomposites with enhanced flexural properties and lower percolation threshold. *Composites Science and Technology*, 67(10):2045–2051, 2016.
- [61] Wenge Zheng and Shing-Chung Wong. Electrical conductivity and dielectric properties of pmma/expanded graphite composites. *Composites Science and Technology*, 63(2):225–235, 2013.
- [62] Yang Hua, Fei Li, Yu Liu, Gui-Wen Huang, Hong-Mei Xiao, Yuan-Qing Li, Ning Hu, and Shao-Yun Fu. Positive synergistic effect of graphene oxide/carbon nanotube hybrid coating on glass fiber/epoxy interfacial normal bond strength. *Composites Science and Technology*, 149:294–304, 2017.
- [63] H.T.; Viculis L.; Kaner R. Kim, H.C.; Hahn. Proceedings of the caneus conference. *AIAA*, 67(5), 2014.
- [64] Haroon Mahmood, Manoj Tripathi, Nicola Pugno, and Alessandro Pegoretti. Enhancement of interfacial adhesion in glass fiber/epoxy composites by electrophoretic deposition of graphene oxide on glass fibers. *Composites Science and Technology*, 126:149–157, 2016.
- [65] Yinhui She, Guohua Chen, and Dajun Wu. Fabrication of polyethylene/graphite nanocomposite from modified expanded graphite. *Polymer International*, 56(5): 679–685, 2015.
- [66] Donghwan Cho, Sangyeob Lee, Gyeongmo Yang, Hiroyuki Fukushima, and Lawrence T Drzal. Dynamic mechanical and thermal properties of phenylethynyl-terminated polyimide composites reinforced with expanded graphite nanoplatelets. *Macromolecular Materials and Engineering*, 290(3):179–187, 2015.
- [67] Aea Yasmin, JJ Luo, JL Abot, and IM Daniel. Mechanical and thermal behavior of clay/epoxy nanocomposites. *Composites Science and technology*, 66(14):2415–2422, 2016.
- [68] Xuming Yao, Xinyu Gao, Jianjun Jiang, Chumeng Xu, Chao Deng, and Junbiao Wang. Comparison of carbon nanotubes and graphene oxide coated carbon fiber for

- improving the interfacial properties of carbon fiber/epoxy composites. *Composites Part B: Engineering*, 132:170–177, 2018.
- [69] Pedro Henrique Cury Camargo, Kestur Gundappa Satyanarayana, and Fernando Wypych. Nanocomposites: synthesis, structure, properties and new application opportunities. *Materials Research*, 12(1):1–39, mar 2014. ISSN 1516-1439. doi: 10.1590/S1516-14392009000100002. URL [http://www.scielo.br/scielo.php?script=sci\\_arttext&pid=S1516-14392009000100002&lng=en&nrm=iso&tlng=en](http://www.scielo.br/scielo.php?script=sci_arttext&pid=S1516-14392009000100002&lng=en&nrm=iso&tlng=en).
- [70] Luis EF Foa Torres, Stephan Roche, and Jean-Christophe Charlier. *Introduction to graphene-based nanomaterials: from electronic structure to quantum transport*. Cambridge University Press, 2014.
- [71] Péter Nemes-Incze, Gergő Kukucska, János Koltai, Jenő Kürti, Chanyong Hwang, Levente Tapasztó, and László P Biró. Preparing local strain patterns in graphene by atomic force microscope based indentation. *Scientific Reports*, 7, 2017.
- [72] Joseph Scott Bunch. MECHANICAL AND ELECTRICAL PROPERTIES OF GRAPHENE SHEETS. 10, 2013. URL [https://www.mceugroup.lassp.cornell.edu/sites/mceuen/files/publications/Thesis{}\\_Bunch.pdf](https://www.mceugroup.lassp.cornell.edu/sites/mceuen/files/publications/Thesis{}_Bunch.pdf).
- [73] Fei Hui, Pujashree Vajha, Yanfeng Ji, Chengbin Pan, Enric Grustan-Gutierrez, Huiling Duan, Peng He, Guqiao Ding, Yuanyuan Shi, and Mario Lanza. Variability of graphene devices fabricated using graphene inks: Atomic force microscope tips. *Surface and Coatings Technology*, 320:391–395, 2017.
- [74] Matthew R Rosenberger, Michael Cai Wang, Xu Xie, John A Rogers, SungWoo Nam, and William P King. Measuring individual carbon nanotubes and single graphene sheets using atomic force microscope infrared spectroscopy. *Nanotechnology*, 28(35):355707, 2017.
- [75] Xiaogan Liang, Zengli Fu, and Stephen Y Chou. Graphene Transistors Fabricated via Transfer-Printing In Device Active-Areas on Large Wafer. doi: 10.1021/nl072566s. URL [http://www.bioee.ee.columbia.edu/courses/upload/Bibliography/liang{}\\_nanoletters{}\\_2014.pdf](http://www.bioee.ee.columbia.edu/courses/upload/Bibliography/liang{}_nanoletters{}_2014.pdf).
- [76] Adriano Ambrosi and Martin Pumera. Electrochemically exfoliated graphene and graphene oxide for energy storage and electrochemistry applications. *Chemistry-A European Journal*, 22(1):153–159, 2016.
- [77] Syed Sajid Ali Shah and Habib Nasir. Exfoliation of graphene and its application as filler in reinforced polymer nanocomposites. *Nano Hybrids*, 11, 2016.

- [78] Nina I Kovtyukhova, Nestor Perea-López, Mauricio Terrones, and Thomas E Malouk. Atomically thin layers of graphene and hexagonal boron nitride made by solvent exfoliation of their phosphoric acid intercalation compounds. *ACS nano*, 11(7):6746–6754, 2017.
- [79] A K Geim and K S Novoselov. the Rise of Graphene. pages 1–14. ISSN 15213765. doi: 10.1103/PhysRevLett.77.3865.
- [80] Xiaodan Xu, Lu Cai, Xiaoli Zheng, and Qun Xu. Molecular dynamics simulation of solvent-exfoliation and stabilization of graphene with the assistance of compressed carbon dioxide and pyrene-polyethylene glycol. *Physical Chemistry Chemical Physics*, 2017.
- [81] Yan-Jun Wan, Long-Cheng Tang, Dong Yan, Li Zhao, Yi-Bao Li, Lian-Bin Wu, Jian-Xiong Jiang, and Guo-Qiao Lai. Improved dispersion and interface in the graphene/epoxy composites via a facile surfactant-assisted process. *Composites science and technology*, 82:60–68, 2013.
- [82] Yan-Jun Wan, Long-Cheng Tang, Li-Xiu Gong, Dong Yan, Yi-Bao Li, Lian-Bin Wu, Jian-Xiong Jiang, and Guo-Qiao Lai. Grafting of epoxy chains onto graphene oxide for epoxy composites with improved mechanical and thermal properties. *Carbon*, 69:467–480, 2014.
- [83] Nabil A Abdel Ghany, Safaa A Elsherif, and Hala T Handal. Revolution of graphene for different applications: State-of-the-art. *Surfaces and Interfaces*, 9: 93–106, 2017.
- [84] Ting Wang, Cai-hong Yang, Chun-Li Man, Li-guang Wu, Wan-Lei Xue, Jiang-nan Shen, Bart Van der Bruggen, and Zhuan Yi. Enhanced separation performance for co2 gas of mixed-matrix membranes incorporated with tio2/graphene oxide: Synergistic effect of graphene oxide and small tio2 particles on gas permeability of membranes. *Industrial & Engineering Chemistry Research*, 56(31):8981–8990, 2017.
- [85] Junwei Gu, Xutong Yang, Zhaoyuan Lv, Nan Li, Chaobo Liang, and Qiuyu Zhang. Functionalized graphite nanoplatelets/epoxy resin nanocomposites with high thermal conductivity. *International Journal of Heat and Mass Transfer*, 92:15–22, 2016.
- [86] Yan-Jun Wan, Long-Cheng Tang, Dong Yan, Li Zhao, Yi-Bao Li, Lian-Bin Wu, Jian-Xiong Jiang, and Guo-Qiao Lai. Improved dispersion and interface in the graphene/epoxy composites via a facile surfactant-assisted process. *Composites science and technology*, 82:60–68, 2013.

- [87] Junsu Lee, Minjung Kim, James R Chelikowsky, and Gunn Kim. Computational simulation of subatomic-resolution afm and stm images for graphene/hexagonal boron nitride heterostructures with intercalated defects. *Physical Review B*, 94(3):035447, 2016.
- [88] H Li, YJ Zeng, XJ Hu, HH Zhang, SC Ruan, MJ Van Bael, and C Van Haendonck. Thickness-dependent magnetotransport: from multilayer graphene to few-layer graphene. *Carbon*, 124:193–200, 2017.
- [89] Arun Kumar, Kaushal Kumar, PK Ghosh, and KL Yadav. Mwcnt/tio2 hybrid nano filler toward high-performance epoxy composite. *Ultrasonics sonochemistry*, 41:37–46, 2018.
- [90] Mu Ee Foo and Subash CB Gopinath. Feasibility of graphene in biomedical applications. *Biomedicine & Pharmacotherapy*, 94:354–361, 2017.
- [91] Andrey I Dmitriev, Ines Häusler, Werner Österle, Bernd Wetzels, and Ga Zhang. Modeling of the stress–strain behavior of an epoxy-based nanocomposite filled with silica nanoparticles. *Materials & Design*, 89:950–956, 2016.
- [92] Manoj Singla and Vikas Chawla. Mechanical Properties of Epoxy Resin Fly Ash Composite. *Journal of Minerals and Materials Characterization and Engineering*, 09(03):199–210, 2014. ISSN 2327-4077. doi: 10.4236/jmmce.2010.93017. URL <http://www.scirp.org/journal/PaperDownload.aspx?DOI=10.4236/jmmce.2010.93017>.
- [93] Danielle R Klimek-McDonald, Julia A King, Ibrahim Miskioglu, Evan J Pineda, and Greg M Odegard. Determination and modeling of mechanical properties for graphene nanoplatelet/epoxy composites. *Polymer Composites*, 2016.
- [94] Sagheer Gul, Ayesha Kausar, Mazhar Mehmood, Bakhtiar Muhammad, and Saira Jabeen. Progress on epoxy/polyamide and inorganic nanofiller-based hybrids: Introduction, application, and future potential. *Polymer-Plastics Technology and Engineering*, 55(17):1842–1862, 2016.
- [95] Jinyan Wang, Rui Liu, and Xigao Jian. Introduction to epoxy/thermoplastic blends. *Handbook of Epoxy Blends*, pages 1–29, 2016.
- [96] Atsushi Kaiho, Daniele Mazzarella, Masamitsu Satake, Makiko Kogo, Ryo Sakai, and Takashi Watanabe. Construction of the di (trimethylolpropane) cross linkage and the phenylnaphthalene structure coupled with selective  $\beta$ -o-4 bond cleavage for synthesizing lignin-based epoxy resins with a controlled glass transition temperature. *Green Chemistry*, 18(24):6526–6535, 2016.

## Bibliography

- [97] C Liu, T Chen, CH Yuan, CF Song, Y Chang, GR Chen, YT Xu, and LZ Dai. Modification of epoxy resin through the self-assembly of a surfactant-like multi-element flame retardant. *Journal of Materials Chemistry A*, 4(9):3462–3470, 2016.
- [98] Shuiping Li, Huajun Zhu, Tingting Lv, Qin Lin, Haijun Hou, Yanbo Li, Qisheng Wu, and Chong Cui. The effect of amino-terminated hyperbranched polymers on the impact resistance of epoxy resins. *Colloid and Polymer Science*, 294(3): 607–615, 2016.
- [99] Fatemeh Ferdosian, Zhongshun Yuan, Mark Anderson, and Chunbao Charles Xu. Thermal performance and thermal decomposition kinetics of lignin-based epoxy resins. *Journal of Analytical and Applied Pyrolysis*, 119:124–132, 2016.
- [100] Hongbo Gu, Chao Ma, Junwei Gu, Jiang Guo, Xingru Yan, Jiangnan Huang, Qiuyu Zhang, and Zhanhu Guo. An overview of multifunctional epoxy nanocomposites. *Journal of Materials Chemistry C*, 4(25):5890–5906, 2016.
- [101] Tomonaga Okabe, Yutaka Oya, Koichi Tanabe, Gota Kikugawa, and Kenichi Yoshioka. Molecular dynamics simulation of crosslinked epoxy resins: Curing and mechanical properties. *European Polymer Journal*, 80:78–88, 2016.
- [102] X Peng and SA Meguid. Molecular dynamics simulations of the buckling behavior of defective carbon nanotubes embedded in epoxy nanocomposites. *European Polymer Journal*, 93:246–258, 2017.
- [103] Bonsung Koo, Nithya Subramanian, and Aditi Chattopadhyay. Molecular dynamics study of brittle fracture in epoxy-based thermoset polymer. *Composites Part B: Engineering*, 95:433–439, 2016.
- [104] Amin Aramoon, Timothy D Breitzman, Christopher Woodward, and Jaafar A El-Awady. Coarse-grained molecular dynamics study of the curing and properties of highly cross-linked epoxy polymers. *The Journal of Physical Chemistry B*, 120(35):9495–9505, 2016.
- [105] Fariba Safaei, Saied Nouri Khorasani, Hadi Rahnama, Rasoul Esmaeely Neisiany, and Mohammad Sadegh Koochaki. Single microcapsules containing epoxy healing agent used for development in the fabrication of cost efficient self-healing epoxy coating. *Progress in Organic Coatings*, 114:40–46, 2018.
- [106] Peerapan Dittanet, Raymond A Pearson, and Paisan Kongkachuichay. Thermo-mechanical behaviors and moisture absorption of silica nanoparticle reinforcement in epoxy resins. *International Journal of Adhesion and Adhesives*, 78:74–82, 2017.

## Bibliography

- [107] Camille François, Sylvie Pourchet, Gilles Boni, Sari Rautiainen, Joseph Samec, Lucie Fournier, Carine Robert, Christophe M Thomas, Stéphane Fontaine, Yves Gaillard, et al. Design and synthesis of biobased epoxy thermosets from biorenewable resources. *Comptes Rendus Chimie*, 2017.
- [108] Ke Zhong, Xu Yang, and Xiaohao Wei. Investigation on surface characteristics of epoxy asphalt concrete pavement. *International Journal of Pavement Research and Technology*, 10(6):545–552, 2017.
- [109] Linna Su, Xiaoliang Zeng, Hongping He, Qi Tao, and Sridhar Komarneni. Preparation of functionalized kaolinite/epoxy resin nanocomposites with enhanced thermal properties. *Applied Clay Science*, 148:103–108, 2017.
- [110] Wei-Qi Xie, Yi-Xian Gong, and Kong-Xian Yu. Quantification of the amine value in aliphatic amine epoxy hardeners by using a reaction-based headspace gas chromatographic technique. *Analytical Methods*, 9(16):2440–2444, 2017.
- [111] Brian Johnson, Keshab Paudel, Mark J Kendrick, and Oksana Ostroverkhova. Numerical Modeling of Time-Resolved Photocurrent in Organic Semiconductor Films. URL [http://www.science.oregonstate.edu/~jostroveo/publications/conference{}\\_proceedings/Johnson{}\\_SPIE2013.pdf](http://www.science.oregonstate.edu/~jostroveo/publications/conference{}_proceedings/Johnson{}_SPIE2013.pdf).
- [112] Alfredo J Diaz, Hanaul Noh, Tobias Meier, and Santiago D Solares. High-stress study of bioinspired multifunctional pedot: Pss/nanoclay nanocomposites using afm, sem and numerical simulation. *Beilstein journal of nanotechnology*, 8:2069, 2017.
- [113] Zengrong Hu, Mojib Saei, Guoquan Tong, Dong Lin, Qiong Nian, Yaowu Hu, Shengyu Jin, Jiale Xu, and Gary J Cheng. Numerical simulation of temperature field distribution for laser sintering graphene reinforced nickel matrix nanocomposites. *Journal of Alloys and Compounds*, 688:438–448, 2016.
- [114] AK Manta and KI Tserpes. Parametric numerical simulation of impact response of carbon nanotube/polymer nanocomposites. *Plastics, Rubber and Composites*, 45(4):157–165, 2016.
- [115] Ya-Fei Zhang, Yun-Hong Zhao, Shu-Lin Bai, and Xiaowen Yuan. Numerical simulation of thermal conductivity of graphene filled polymer composites. *Composites Part B: Engineering*, 106:324–331, 2016.
- [116] Bo Mi Lee and Kenneth J Loh. Carbon nanotube thin film strain sensors: comparison between experimental tests and numerical simulations. *Nanotechnology*, 28(15):155502, 2017.

- [117] Yi Huang, Zhaohui Liu, Chuguang Zheng, and Shizhi Qian. Direct numerical simulation of particle segregation and dynamics in inertial microfluidics by discrete external boundary force-lattice boltzmann method. In *Meeting Abstracts*, number 36, pages 2295–2295. The Electrochemical Society, 2016.
- [118] SJ Vijay, Alexandre Tugirumubano, Sun Ho Go, Lee Ku Kwac, and Hong Gun Kim. Numerical simulation and experimental validation of electromagnetic properties for al-mwcnt-fe<sub>2</sub>o<sub>3</sub> hybrid nano-composites. *Journal of Alloys and Compounds*, 731:465–470, 2018.
- [119] Adrian V Catalina, Andreas Buhrig-Polaczek, Charles Monroe, and Adrian S Sabau. Numerical modeling of the dispersion of ceramic nanoparticles during ultrasonic processing of a356-based nanocomposites. In *Advances in the Science and Engineering of Casting Solidification: An MPMD Symposium Honoring Doru Michael Stefanescu*, page 37. Springer, 2016.
- [120] L Snoussi, N Ouerfelli, KV Sharma, N Vrinceanu, AJ Chamkha, and A Guizani. Numerical simulation of nanofluids for improved cooling efficiency in a 3d copper microchannel heat sink (mchs). *Physics and Chemistry of Liquids*, pages 1–21, 2017.
- [121] Daojie Zhang. *Numerical modeling of fluid flow and solidification phenomena during ultrasonic processing of metal-matrix-nanocomposites*. The University of Alabama, 2016.
- [122] Jaros Meller. Molecular Dynamics. URL [http://fizyka.umk.pl/ftp/pub/publications/kmk/Jarek/04Jarek\\_{\\_}Mo1Dyn.pdf](http://fizyka.umk.pl/ftp/pub/publications/kmk/Jarek/04Jarek_{_}Mo1Dyn.pdf).
- [123] Antonio De Nicola, Toshihiro Kawakatsu, Florian Müller-Plathe, and Giuseppe Milano. Fast relaxation of coarse-grained models of polymer interphases by hybrid particle-field molecular dynamics: Polystyrene-silica nanocomposites as an example. *The European Physical Journal Special Topics*, 225(8-9):1817–1841, 2016.
- [124] Manoj Singla and Vikas Chawla. Mechanical Properties of Epoxy Resin Fly Ash Composite. *Journal of Minerals & Materials Characterization & Engineering*, 9(3):199–210, 2015. URL [http://file.scirp.org/pdf/JMMCE20100300003\\_{\\_}77044062.pdf](http://file.scirp.org/pdf/JMMCE20100300003_{_}77044062.pdf).
- [125] Yan Wang, Malin Bergenstråhle-Wohlert, Yaoquan Tu, Hans Ågren, Lars A Berglund, and Jakob Wohlert. Swelling and dimensional stability of xyloglucan/montmorillonite nanocomposites in moist conditions from molecular dynamics simulations. *Computational Materials Science*, 128:191–197, 2017.

## Bibliography

- [126] AR Alian, MAN Dewapriya, and SA Meguid. Molecular dynamics study of the reinforcement effect of graphene in multilayered polymer nanocomposites. *Materials & Design*, 124:47–57, 2017.
- [127] M Zahabul Islam, Monon Mahboob, and Robert L Lowe. Mechanical properties of defective carbon nanotube/polyethylene nanocomposites: A molecular dynamics simulation study. *Polymer Composites*, 37(1):305–314, 2016.
- [128] Feng Lin, Y Xiang, and Hui-Shen Shen. Temperature dependent mechanical properties of graphene reinforced polymer nanocomposites—a molecular dynamics simulation. *Composites Part B: Engineering*, 111:261–269, 2017.
- [129] Shūichi Nosé. A molecular dynamics method for simulations in the canonical ensemble. *Molecular physics*, 52(2):255–268, 1984.
- [130] Mark E Tuckerman, Bruce J Berne, and Glenn J Martyna. Molecular dynamics algorithm for multiple time scales: Systems with long range forces. *The Journal of chemical physics*, 94(10):6811–6815, 1991.
- [131] M. S. Shell. Molecular dynamics ChE210D Today’s lecture: how to evolve a system of classical atoms in time using numerical approximations to Newton’s equations of motion. 2014. URL [https://engineering.ucsb.edu/~shell/che210d/Molecular\\_dynamics.pdf](https://engineering.ucsb.edu/~shell/che210d/Molecular_dynamics.pdf).
- [132] Katsumi Hagita, Hiroshi Morita, Masao Doi, and Hiroshi Takano. Coarse-grained molecular dynamics simulation of filled polymer nanocomposites under uniaxial elongation. *Macromolecules*, 49(5):1972–1983, 2016.
- [133] Hyunseong Shin, Seongmin Chang, Seunghwa Yang, Byeng Dong Youn, and Maenghyo Cho. Statistical multiscale homogenization approach for analyzing polymer nanocomposites that include model inherent uncertainties of molecular dynamics simulations. *Composites Part B: Engineering*, 87:120–131, 2016.
- [134] Mohammad Reza Saeb, Hadi Rastin, Meisam Shabaniyan, Mehdi Ghaffari, and Ghasem Bahlakeh. Cure kinetics of epoxy/ $\beta$ -cyclodextrin-functionalized Fe<sub>3</sub>O<sub>4</sub> nanocomposites: Experimental analysis, mathematical modeling, and molecular dynamics simulation. *Progress in Organic Coatings*, 110:172–181, 2017.
- [135] I Mathioudakis, GG Vogiatzis, Christos Tzoumanekas, and DN Theodorou. Molecular modeling and simulation of atactic polystyrene/amorphous silica nanocomposites. In *Journal of Physics: Conference Series*, volume 738, page 012021. IOP Publishing, 2016.

## Bibliography

- [136] Weinan E. Principles of Multiscale Modeling. 2014. URL [https://web.math.princeton.edu/~weinan/papers/weinan\\_book.pdf](https://web.math.princeton.edu/~weinan/papers/weinan_book.pdf).
- [137] Ioannis G Mathioudakis, Georgios G Vogiatzis, Christos Tzoumanekas, and Doros N Theodorou. Molecular modeling and simulation of polymer nanocomposites at multiple length scales. *IEEE Transactions on Nanotechnology*, 15(3):416–422, 2016.
- [138] Jianxiang Shen, Xue Li, Xiaojun Shen, and Jun Liu. Insight into the dispersion mechanism of polymer-grafted nanorods in polymer nanocomposites: A molecular dynamics simulation study. *Macromolecules*, 50(2):687–699, 2017.
- [139] Hongyu Tang, Huaiyu Ye, Xianping Chen, Xuejun Fan, and Guoqi Zhang. Thermal conductivity of functionalized graphene-polymer nanocomposite: A non-equilibrium molecular dynamics study. In *Thermal, Mechanical and Multi-Physics Simulation and Experiments in Microelectronics and Microsystems (EuroSimE), 2017 18th International Conference on*, pages 1–5. IEEE, 2017.
- [140] Farshid Aghadavoudi, Hossein Golestanian, and Yaghoub Tadi Beni. Investigation of cnt defects on mechanical behavior of cross linked epoxy based nanocomposites by molecular dynamics. *Int J Adv Design Manuf Technol*, 9(1):137–146, 2016.
- [141] M. Parrinello and A Rahman. Crystal structure and pair potentials: A molecular-dynamics study. *Physical Review Letters*, 45(14):1196, 1980.
- [142] Katsumi Hagita, Hiroshi Morita, and Hiroshi Takano. Molecular dynamics simulation study of a fracture of filler-filled polymer nanocomposites. *Polymer*, 99:368–375, 2016.
- [143] Yu-hua Wang, Wei-hua Wang, Zhiqiang Zhang, Liancai Xu, and Ping Li. Study of the glass transition temperature and the mechanical properties of pet/modified silica nanocomposite by molecular dynamics simulation. *European Polymer Journal*, 75:36–45, 2016.
- [144] Rupali Sahu and S Anup. Molecular dynamics study of toughening mechanisms in nano-composites as a function of structural arrangement of reinforcements. *Materials & Design*, 100:132–140, 2016.
- [145] Roza-Eleftheria Roussou and Kostas Karatasos. Graphene/poly (ethylene glycol) nanocomposites as studied by molecular dynamics simulations. *Materials & Design*, 97:163–174, 2016.
- [146] S Mathiazhagan and S Anup. Influence of platelet aspect ratio on the mechanical behaviour of bio-inspired nanocomposites using molecular dynamics. *Journal of the mechanical behavior of biomedical materials*, 59:21–40, 2016.

## Bibliography

- [147] Zijian Zheng, Guanyi Hou, Xiuyang Xia, Jun Liu, Mesfin Tsige, Youping Wu, and Liqun Zhang. Molecular dynamics simulation study of polymer nanocomposites with controllable dispersion of spherical nanoparticles. *The Journal of Physical Chemistry B*, 2017.
- [148] Dinesh R Katti, Keshab B Thapa, and Kalpana S Katti. Modeling molecular interactions of sodium montmorillonite clay with 3d kerogen models. *Fuel*, 199: 641–652, 2017.
- [149] Argyrios Karatrantos, Nigel Clarke, and Martin Kröger. Modeling of polymer structure and conformations in polymer nanocomposites from atomistic to mesoscale: A review. *Polymer Reviews*, 56(3):385–428, 2016.
- [150] Argyrios Karatrantos, Nigel Clarke, and Martin Kröger. Modeling of polymer structure and conformations in polymer nanocomposites from atomistic to mesoscale: A review. *Polymer Reviews*, 56(3):385–428, 2016.
- [151] Matthieu Chavent, Anna L Duncan, and Mark SP Sansom. Molecular dynamics simulations of membrane proteins and their interactions: from nanoscale to mesoscale. *Current opinion in structural biology*, 40:8–16, 2016.
- [152] Matthew M Dedmon, Kresten Lindorff-Larsen, John Christodoulou, Michele Vendruscolo, and Christopher M Dobson. Mapping long-range interactions in  $\alpha$ -synuclein using spin-label nmr and ensemble molecular dynamics simulations. *Journal of the American Chemical Society*, 127(2):476–477, 2005.
- [153] Hongshu Zhang, Shiling Yuan, Jichao Sun, Jianqiang Liu, Haiping Li, Na Du, and Wanguo Hou. Molecular dynamics simulation of sodium dodecylsulfate (sds) bilayers. *Journal of colloid and interface science*, 506:227–235, 2017.
- [154] David Roylance. Finite Element Analysis. 2016. URL [https://ocw.mit.edu/courses/materials-science-and-engineering/3-11-mechanics-of-materials-fall-1999/modules/MIT3\\_{\\_}11F99\\_{\\_}fea.pdf](https://ocw.mit.edu/courses/materials-science-and-engineering/3-11-mechanics-of-materials-fall-1999/modules/MIT3_{_}11F99_{_}fea.pdf).
- [155] Ping Zhu, ZX Lei, and Kim Meow Liew. Static and free vibration analyses of carbon nanotube-reinforced composite plates using finite element method with first order shear deformation plate theory. *Composite Structures*, 94(4):1450–1460, 2014.
- [156] Andrei A Gusev and Hans Rudolf Lusti. Rational design of nanocomposites for barrier applications. *Advanced Materials*, 13(21):1641–1643, 2013.

- [157] Young Seok Song and Jae Ryoum Youn. Evaluation of effective thermal conductivity for carbon nanotube/polymer composites using control volume finite element method. *Carbon*, 44(4):710–717, 2016.
- [158] DR Katti, KS Katti, JM Sopp, and M Sarikaya. 3d finite element modeling of mechanical response in nacre-based hybrid nanocomposites. *Computational and Theoretical Polymer Science*, 11(5):397–404, 2015.
- [159] Haibo Yang, Fanzhu Li, Tung W Chan, Li Liu, and Liqun Zhang. Effect of nanofiller shape on viscoelasticity of rubber nanocomposite investigated by fea. *Composites Part B: Engineering*, 92:160–166, 2016.
- [160] Dimitrios Tzetzis, Konstantinos Tsongas, and Gabriel Mansour. Determination of the mechanical properties of epoxy silica nanocomposites through fea-supported evaluation of ball indentation test results. *Materials Research*, 20(6):1571–1578, 2017.
- [161] G P Nikishkov. INTRODUCTION TO THE FINITE ELEMENT METHOD. 2014. URL <http://homepages.cae.wisc.edu/~suresh/ME964Website/M964Notes/Notes/introfem.pdf>.
- [162] Multiscale modelling and design for engineering application. 2014. ISSN 2242-1211. URL <http://www.vtt.fi/publications/index.jsp>.
- [163] Giulio Scocchi, Paola Posocco, Jan-Willem Handgraaf, Johannes GEM Fraaije, Maurizio Fermeglia, and Sabrina Pricl. A complete multiscale modelling approach for polymer–clay nanocomposites. *Chemistry-A European Journal*, 15(31):7586–7592, 2015.
- [164] Dimitri D Vvedensky. Multiscale modelling of nanostructures. *Journal of Physics: Condensed Matter*, 16(50):R1537, 2014.
- [165] PD Spanos and A Kontsos. A multiscale monte carlo finite element method for determining mechanical properties of polymer nanocomposites. *Probabilistic Engineering Mechanics*, 23(4):456–470, 2014.
- [166] A Montazeri and H Rafii-Tabar. Multiscale modeling of graphene-and nanotube-based reinforced polymer nanocomposites. *Physics Letters A*, 375(45):4034–4040, 2013.
- [167] Y Chandra, F Scarpa, R Chowdhury, S Adhikari, and J Sienz. Multiscale hybrid atomistic-fe approach for the nonlinear tensile behaviour of graphene nanocomposites. *Composites Part A: Applied Science and Manufacturing*, 46:147–153, 2013.

## Bibliography

- [168] J Cho, JJ Luo, and IM Daniel. Mechanical characterization of graphite/epoxy nanocomposites by multi-scale analysis. *Composites science and technology*, 67(11):2399–2407, 2016.
- [169] Dean M Philipp and Richard A Friesner. Mixed ab initio qm/mm modeling using frozen orbitals and tests with alanine dipeptide and tetrapeptide. *Journal of computational chemistry*, 20(14):1468–1494, 2014.
- [170] Patrick Jenny, Seong H Lee, and Hamdi A Tchelepi. Adaptive multiscale finite-volume method for multiphase flow and transport in porous media. *Multiscale Modeling & Simulation*, 3(1):50–64, 2015.
- [171] Mikhail I Katsnelson. Graphene: carbon in two dimensions A two-dimensional form of carbon Graphene: carbon in two dimensions REVIEW. 10:1–2, 2014. URL [http://www.condmat.physics.manchester.ac.uk/pdf/mesoscopic/news/graphene/MaterialsToday{}\\_2014.pdf](http://www.condmat.physics.manchester.ac.uk/pdf/mesoscopic/news/graphene/MaterialsToday{}_2014.pdf).
- [172] Changgu Lee, Xiaoding Wei, Jeffrey W Kysar, and James Hone. Measurement of the elastic properties and intrinsic strength of monolayer graphene. *science*, 321(5887):385–388, 2008.
- [173] Tanya Kairn, Peter J Daivis, Ivan Ivanov, and Sati N Bhattacharya. Molecular-dynamics simulation of model polymer nanocomposite rheology and comparison with experiment. *The Journal of chemical physics*, 123(19):194905, 2005.